Characterization of Peptidoglycan, and the Enzymes That Synthesize it, in *Borrelia burgdorferi* and Insights into the Peptidoglycan of Other Pathogenic *Borrelia*

Tanner Gage DeHart

Thesis submitted to the faculty of the Virginia Polytechnic Institute and State University
in partial fulfillment of the requirements for the degree of

Master of Science
In
Biochemistry

Brandon L. Jutras (chair)
Richard F. Helm
Pablo Sobrado

May 12th, 2021
Blacksburg, Virginia

Keywords: Lyme disease, *Borrelia burgdorferi*, peptidoglycan

Characterization of Peptidoglycan, and the Enzymes That Synthesize it, in *Borrelia burgdorferi* and Insights into the Peptidoglycan of Other Pathogenic *Borrelia*

Tanner Gage DeHart

Scientific Abstract

Peptidoglycan (PG) is an essential cell-wall biopolymer in virtually all bacteria. It is composed of glycan strands of *N*-acetylglucosamine (Glc*N*Ac) and *N*-acetylmuramic acid (Mur*N*Ac) crosslinked by peptide chains of alternating D- and L- amino acids and diamines. PG plays an important role in 1) cell elongation and division, 2) cell strength and morphology, 3) antibiotic susceptibility, and 4) host immune detection and modulation. While differences in peptide chains are common, deviations in glycan strand composition were not previously known to occur. Here, we provide characterization of the first known deviation to bacterial glycan strand composition — Glc*N*Ac-Glc*N*Ac-anhMur*N*Ac (G-G-anhM) in *Borrelia burgdorferi*, the causative agent of Lyme disease. *B. burgdorferi* with less G-G-anhM were found to be significantly less motile, flexible, and stress-tolerant while possessing gross morphological defects and less overall PG. Our studies also characterized the muropeptide profile of *Borrelia afzelii, Borrelia garinii, and Borrelia hermsii* — species of *Borrelia* associated with causing different disease manifestations of Lyme disease, and relapsing fever, respectively. These species were found to incorporate appreciable amounts of G-G-anhM into their PG, suggesting an evolutionary adaptation to life inside a tick that predates the differentiation of Lyme disease and relapsing fever *Borrelia*. Finally, we provide partial characterization of a putative penicillin-binding protein in *B. burgdorferi* — a class of highly conserved PG synthesis enzymes present in the vast majority of bacteria. Collectively, the work in this thesis furthers our understanding of the structure, function, and synthesis of PG in *Borrelia*.

Characterization of Peptidoglycan, and the Enzymes That Synthesize it, in *Borrelia burgdorferi* and Insights into the Peptidoglycan of Other Pathogenic *Borrelia*

Tanner Gage DeHart

General Audience Abstract

Peptidoglycan (PG) is the main cell-wall component in the vast majority of bacteria. PG is composed of strong, rigid sugars linked together by short, flexible amino acid chains, and resembles a mesh-like bag that surrounds the cell. In nearly all bacteria that have PG, it plays an important role in how 1) the cell grows and divides, 2) the cell dictates its shape, 3) antibiotics treat bacterial infections, and 4) the human body detects and responds to a bacterial infection. While the amino acids that make up PG are known to differ between bacterial species, deviations in sugar organization are not known to occur. Here, we characterize the first known deviation to sugar organization in bacterial PG in *Borrelia burgdorferi* — the bacteria that causes Lyme disease. *B. burgdorferi* with less of this deviation possess defects absent in their normal counterparts. In addition, we show that other *Borrelia* species that cause a variety of different diseases around the world mimic this sugar deviation, suggesting the majority, if not all, of *Borrelia* may do so. Finally, we provide partial characterization of the function of an enzyme thought to synthesize PG in *B. burgdorferi*. Collectively, the work in this thesis furthers our understanding of the structure, function, and synthesis of PG in *Borrelia*.

Table of Contents

Acknowledgements

To my family, Sonya, Booie, Bryce, Skyler, Narlene, Dee, and Melvin, thank you for your continuous support of the endeavors in my life. I would not have been able to succeed without such a wonderful support system.

To Dr. Jutras, thank you for being a phenomenal mentor. The past three years of your guidance have been the most incredible experience in my academic and professional career thus far. You've molded me into the scientist I am and shaped the image for the scientist I aspire to be.

To Dr. Helm, thank you for your guidance both in the classroom and in the lab. Your teachings kindled my passion for biochemistry and your mentorship was instrumental in many aspects of my work.

To members of the Jutras Lab, past and present, thank you for making this lab feel like home.

List of Figures & Tables

List of Abbreviations

PG	Peptidoglycan
Glc*N*Ac	*N*-acetylglucosamine
Mur*N*Ac	*N*-acetylmuramic acid
Hex*N*Ac	*N*-acetylhexosamine
Man*N*Ac	*N*-acetylmannosamine
Gal*N*Ac	*N*-acetylgalactosamine
mDAP	meso-2,6-diaminopilmelic acid
Orn	Ornithine
Gly	Glycine
Ala	Alanine
Glu	Glutamate
PBP	Penicillin-Binding Protein

Chapter I

Literature Review

Lyme Disease in the United States

Lyme disease is the most common vector-borne illness in the United States with an estimated >450,000 new cases every year[1]. The prevalence of this disease is rapidly increasing — in contrast to just over 16,000 cases recorded in 1996 — with the majority of cases localized in the Northeast; namely, Maine, Vermont, Pennsylvania, New Hampshire, and Rhode Island[2]. However, the occurrence of Lyme disease continues to spread as a result of environmental and societal factors. The most important factors include: increased geographic range of the tick vector, climate change, deforestation, land-use changes, public awareness, and improvements in disease reporting standards and surveillance techniques[3,4]. As a result of its expanding range and rapidly increasing prevalence, Lyme disease will likely be a recurring and ever-important issue within the United States for years to come.

A Vector-borne Illness

When people hear "Lyme disease", they typically think of the "deer tick" or "black-legged tick". Both names refer to the species *Ixodes scapularis* — the vector responsible for spreading Lyme disease in the United States[5]. First observed in 1977, Lyme disease was hypothesized to be transmitted via arthropod vector, more specifically, *I. scapularis*[6,7]. In the following years, it was discovered that Lyme disease in the United States was caused by *Borrelia burgdorferi* sensu stricto (hereafter referred to as *B. burgdorferi*), a spirochetal bacterium living within the midgut of the *I. scapularis* tick[8]. Transmission of *B. burgdorferi* occurs when *I. scapularis* feeds on a host and the resulting infection can manifest into Lyme disease[9]. Interestingly, *I. scapularis* is not the native

reservoir for *B. burgdorferi;* meaning, the tick acquires *B. burgdorferi* upon feeding on an infected host[10]. Transovarial transmission of *B. burgdorferi* from adult ticks to eggs is not known to occur[11].

The life cycle of *I. scapularis* is relatively complex, with the range of hosts varying as the tick progresses from larva, to nymph, to adult. Larva and nymph-stage ticks feed on rodents, birds, insectivores, and other small mammals[12,13]. Ticks of this age commonly acquire *B. burgdorferi* by feeding on the white-footed mouse (*Peromysus leucopus*) — one of the most important native reservoirs of *B. burgdorferi* in the United States[14]. *B. burgdorferi* can first be acquired at the larval stage, meaning nymph and adult-stage ticks who previously acquired *B. burgdorferi* are capable of transmitting the Lyme disease spirochete to subsequent hosts. Nymph-stage ticks are the primary vector for human infection with *B. burgdorferi* — their small size makes them difficult to detect and more likely to feed long enough to transmit the Lyme disease spirochete to their host[9,15]. Adult ticks feed mostly on larger mammals; primarily, white-tailed deer (*Odocoileus virginianus*). White-tailed deer appear to be capable of clearing *B. burgdorferi* infection in a tick[16], resulting in adult ticks playing a smaller role in human infection[15,17].

While there are multiple hosts for *I. scapularis*, and subsequently *B. burgdorferi*, in nature, many show no symptoms of Lyme disease. The best example of this phenomena is the white-footed mouse, possessing no adverse health effects upon long-term infection with the bacteria[18]. In contrast to native reservoirs, humans are an incidental host for both the tick and *B. burgdorferi* meaning they are not required for survival of either population in nature[5]. Unfortunately, human infection with the Lyme disease spirochete can result in chronic, debilitating, disease manifestations.

The Manifestation of Lyme Disease

Borrelia burgdorferi sensu stricto is the causative agent of Lyme disease in the United States. Human Lyme disease is a biphasic illness characterized by acute and late-stage disease states. The acute-stage, ranging from 3 to 30 days post-infection, is accompanied by flu-like symptoms of fatigue, fever and muscle aches with 70-80% of patients displaying an erythema migrans rash[19,20]. Appearance of an erythema migrans is typically indicative of infection; however, not all patients will develop one. Out of those who do less than 20% will have the typical bull's-eye-like appearance[20]. If left untreated, late-stage symptoms can develop and are associated with dissemination of *B. burgdorferi* to different tissues throughout the body. These symptoms can manifest as Lyme arthritis[21], partial facial palsy[22], and potentially fatal Lyme carditis[22]. Infection with *B. burgdorferi* should be treated promptly, and the most common treatment options are doxycycline, amoxicillin, and cefuroxime — all broad-spectrum antibiotics[23]. Despite the increasing prevalence of Lyme disease in the United States and around the world, antibiotics and treatments specifically targeting *B. burgdorferi* are yet to be developed. One of the main reasons for this complete lack of specialized treatment options is the inability to effectively screen for, detect, and culture *B. burgdorferi* from patient samples[24]. A promising candidate for addressing these shortcomings is peptidoglycan from *B. burgdorferi* itself.

Peptidoglycan in all bacteria

Peptidoglycan (PG) is the main component of the bacteria cell wall, acting as a sacculus mesh that envelopes the cell. PG is composed of strong, rigid, glycan strands crosslinked by short, flexible, peptide chains. The glycan strands consist of alternating *N*-acetylglucosamine (Glc*N*Ac) and *N*-acetylmuramic acid (Mur*N*Ac) linked by β-1,4 glycosidic bonds[25]. Glycan strand chain

length differs between bacterial species but are usually on the magnitude of 20-40 disaccharide (Glc*N*Ac-Mur*N*Ac) units[26]. These chains terminate with an anhydroMur*N*Ac residue[27] — a residue incapable of polymerizing further β-1,4 glycosidic bonds. Peptide chains stem from the D-lactoyl group on Mur*N*Ac, with the most common composition being L-Ala-D-Glu-diamine-D-Ala-D-Ala, where the diamine is typically meso-2,6-diaminopilmelic acid (mDAP), D-lysine, or ornithine, in gram-negative bacteria, gram-positive bacteria, and spirochetes, respectively[28]. During crosslinking, the terminal D-Ala is often cleaved to make the reaction thermodynamically favorable, and the resulting peptide stem is crosslinked to an adjacent peptide stem bound to another Mur*N*Ac[29]. Amino acids in the peptide chain are labeled 1-5, with the most proximal amino acid to the Mur*N*Ac designated as 1. Crosslinking between peptide stems most often occurs between the amino group of the diamine in the 3 position and a carboxyl group of D-Ala in an adjacent stem's 4 position[28]. This can be accomplished through direct crosslinking[30], or by use of a short peptide bridge between stems[31]. While variations in the amino acids and crosslinked positions in peptide chains are common between bacterial species, deviations in glycan strand composition are not known to occur.

In all bacteria that incorporate PG, it is important for 1) cell strength and morphology[32], 2) cell elongation and division[33], 3) it serves as a major antibiotic target[34], and 4) it plays a role in host immune detection and modulation[35]. As a result, the ability of a cell to synthesize and manipulate their PG is directly related to their viability — an inability to create PG and maintain its integrity has major adverse effects for the cell.

Borrelia burgdorferi: An Atypical Gram-Negative Bacteria

Borrelia burgdorferi is a gram-negative, obligate parasite, spirochetal bacterium possessing a variety of genetic, enzymatic, and cellular abnormalities that make it unique relative to the majority of bacteria. To begin, *B. burgdorferi's* genome is composed of a linear chromosome — uncommon in bacteria — alongside over 20 circular and linear plasmids[36]. Despite this odd organization, *B. burgdorferi* encodes many known, and differentially expressed, lipoproteins and regulatory agents beneficial for cycling between arthropod and vertebrate hosts[37,38]. However, *B. burgdorferi* lacks classical virulence factors, such as lipopolysaccharide, commonly associated with gram-negative bacteria[39]. Even more striking, *B. burgdorferi* lacks many biosynthetic pathways necessary to create amino acids, fatty acids, nucleotides, and enzyme cofactors[36]; instead, relying on exploiting their host for nutrients. As a result of their substantial reliance on scavenging, *B. burgdorferi* can utilize a vast array of lipoproteins and host-derived lipids[40,41].

As a diderm, the cell envelope of *B. burgdorferi* is composed of an inner and outer cell membrane. The space residing between these membranes — the periplasm — is home to *B. burgdorferi's* PG layer. Like many bacteria, *B. burgdorferi* rely on flagella to be motile. However, unlike most bacteria whose flagella protrude from the exterior of their cell membrane, *B. burgdorferi* house their flagella within their periplasm — a trait common in spirochetes[42]. In the periplasm, *B. burgdorferi's* flagella run the length of the cell, wrapping around the cell cylinder, and are anchored to an enzymatic motor in the PG at each pole, dictating the morphology of the cell[43]. These motors "crank" *B. burgdorferi's* anchored flagella, wringing the bacteria along its longitudinal axis and propelling it forward at incredible speeds[44]. However, this speed comes at the cost of immense torsional stress on the PG sacculi[45], suggesting *B. burgdorferi* may have evolved structurally to withstand this force.

Compared to most bacteria, the PG of *B. burgdorferi* has a variety of unique features. Like many other spirochetes, *B. burgdorferi* incorporates the diamine ornithine (Orn) into its PG, which is relatively uncommon for bacteria in general[28]. Unlike most other spirochetes, *B. burgdorferi*'s Orn always has glycine (Gly) linked to its ε-group. The amino group of the ε-linked Gly also participates in crosslinking, forming a small peptide bridge between stems, where most other bacteria use the amino group from their diamine for this purpose[46]. In addition to the incorporation of Orn-Gly residues, D-Ala-D-Ala moieties are rarely found in the peptide chains of *B. burgdorferi* PG[46]. Outside of deviations to the peptide stem, previous studies have shown *B. burgdorferi's* PG alone is capable of causing a robust immune response in a host and induces arthritis just one day post-injection in a murine model[46]. This is compounded by *B. burgdorferi* lacking a muropeptide recycling pathway, resulting in nearly 50% of PG being shed into the host per generation[46]. Accompanying the shed PG is PG-associated protein NapA — capable of exacerbating the immune response in a host by acting as a molecular beacon[47]. The culmination of all of these unusual characteristics makes *B. burgdorferi* PG highly unique and pathogenic in comparison to that of most other bacteria.

Perhaps the most peculiar aspect of *B. burgdorferi's* biology is its method of cellular elongation and division. These processes are intimately linked to PG expansion and remodeling in many bacteria, and must be tightly regulated, both spatially and temporally, for the cell to correctly organize itself prior to, and after, division. For many bacteria, this involves synthesizing PG from their poles or throughout their cell cylinder to elongate — polar[48] and lateral growth[49], respectively — followed by septal PG synthesis to divide. Differing from this norm, *B. burgdorferi* exhibits three separate zones of PG synthesis: mid-cell, ¼, and ¾ cell-length, with the latter two zones initializing synthesis as the cell begins to separate cytoplasmic components for its daughter cells[50].

Interestingly, these three zones are conserved regardless of cell length, and the ¼ and ¾ cell-length PG synthesis sites establish mid-cell for the resulting daughter cells post-division[50]. This unique form of division and maternally dictated organization alludes to the existence of potentially novel PG synthesis machinery capable of performing these specialized tasks.

The Enzymes Responsible for Peptidoglycan Synthesis

Penicillin-binding proteins (PBPs) are essential PG synthesis enzymes in the vast majority of bacteria[51]. PBPs are characterized into two groups, high and low molecular weight, based on their size, and further subdivided into class A and B, depending on their role in PG synthesis. Type A PBPs catalyze transglycosylation and transpeptidase reactions — linking Glc*N*Ac and Mur*N*Ac while also being capable of crosslinking peptide chains in nascent PG[52]. Type B PBPs exclusively perform transpeptidase reactions, having a higher affinity for D-Ala-D-Ala moieties[53]. Due to their importance in PG synthesis PBPs are lucrative drug targets; mainly, as their name suggests, for β-lactam drugs such as penicillin, methicillin, and cefuroxime[54]. These drugs inhibit PG synthesis by resembling D-Ala, the substrate used by PBPs to perform transpeptidase reactions[53]. Upon entering the PBP's active site, the β-lactam covalently binds, permanently disabling the enzyme, resulting in a lack of cell-wall maintenance and eventual cell death. However, in recent years, some bacteria have demonstrated a resistance to β-lactam antibiotics. The most widely known example of this is Methicillin-Resistant *Staphylococcus aureus* (MRSA) — a cocci bacteria that is resistant to methicillin, a commonly used β-lactam[55]. MRSA possesses a unique PBP2a, capable of resisting β-lactam antibiotics while compensating for the inhibition of the cell's other PBPs in the presence of β-lactams. This is accomplished through allosteric regulation, where the transpeptidase active site of PBP2a is shielded from the environment unless nascent PG precursor is bound[56]. Thus exists

an evolutionary arms race between scientists, to develop more efficacious antibiotics, and bacteria, to evolve ways to tolerate our treatments.

Lyme Disease Abroad: Species of Borrelia Around the World

Outside of the United States, Lyme disease is caused by a variety of *Borrelia* species, each localized to a specific geographical region. As members of the same genus, these *Borrelia* retain a relatively conserved set of genomic data[57]; however, their late-stage disease manifestations differ greatly. In Eurasia, *Borrelia afzelii* and *Borrelia garinii* are the main causative agents of Lyme disease. European countries report a combined >65,000 cases reported per year — the most of any arthropod-borne illness[58]. Similarly, these *Borrelia* strains are responsible for Lyme disease in Russia[59], Japan[60], and China, with the latter seeing upwards of 30,000 cases per year[61]. Although acute-stage symptoms are similar between species, untreated *B. afzelii* infection can lead to the development of acrodermatitis — a skin rash characterized by inflammation and lesions[62]. In comparison, late-stage *B. garinii* infection often appears as neuroborreliosis — a nervous system manifestation accompanied by meningitis-like symptoms, pain radiating from the spine, and on occasion, partial paralysis[63]. Interestingly, while each *Borrelia* species is associated with a late-stage disease manifestation, these manifestations are not exclusive to any single species.

While *B. burgdorferi, B. garinii*, and *B. afzelii* are the main causative agents of Lyme disease around the world, there are at least 6 additional species of *Borrelia* capable of causing Lyme disease in humans[64]. Despite their global impact, little is known about the cellular and molecular differences between these *Borrelia* species responsible for such strikingly different Lyme disease manifestations.

What Lies Ahead

In this thesis I provide an in-depth characterization of the muropeptides, or subunits, that make up peptidoglycan in *B. burgdorferi*. Analysis into *B. burgdorferi's* muropeptide profile verified the existence of, and characterized, the first documented deviation to glycan strand composition in all studied bacterial peptidoglycan — the incorporation of Glc*N*Ac-Glc*N*Ac. Further studies demonstrated the implications of incorporating Glc*N*Ac-Glc*N*Ac, and the consequences of failure to do so. In addition, I present a comparison of the muropeptide profiles between multiple species of *Borrelia* — different pathogenic bacteria that cause various forms of disease throughout the world. Finally, I provide evidence for, and partial characterization of, a putative penicillin-binding protein in *B. burgdorferi* — a class of peptidoglycan synthesis enzymes hypothesized to perform essential functions in *B. burgdorferi*.

Chapter II

Methods

Borrelia strains, growth conditions, and genome analysis

All *Borrelia burgdorferi* strains used in these studies are transformable derivatives of the type strain[36]. *B. burgdorferi* B31-5A11, B31-5A3, and a non-infectious (n.i.) clone of B31-5A3[65] were provided by Frank Gheradini (NIH), Jenifer Coburn (Medical College of Wisconsin), and Utpal Pal (University of Maryland), respectively. B31-5A3/*chbC1* strain was provided by Patricia Rosa (Rocky Mountain Labs, NIH) and has been characterized elsewhere[66].

All *B. burgdorferi* strains were grown in Barbour-Stoenner-Kelly II (BSK-II) media supplemented with 6% heat inactivated rabbit serum (Gibco Laboratories), hereafter referred to as BSK-II complete culture media. Metabolic labeling studies simply replaced unlabeled Glc*N*Ac (Sigma-Aldrich, 0.33 g/L) with 1-C^{13} Glc*N*Ac or 1-C^{13} Man*N*Ac (Omicron Biochemicals). Glc*N*Ac-free BSK-II was supplemented with varying amounts of Gal*NA*c or Man*N*Ac (Sigma Aldrich), as described in the text.

Borrelia afzelii, *Borrelia garinii*, and *Borrelia hermsii* strains used in these studies were American Type Culture Collection (ATCC) banked type strains. All three *Borrelia* species were cultured in Barbour-Stoenner-Kelly-H (BSK-H) complete media (Sigma-Aldrich). To normalize for differences in media composition, B31-5A3 *B. burgdorferi* was also grown in BSK-H complete media for experiments making interspecies comparisons.

Regardless of media used or media manipulations, all cultures were incubated at 37°C with 5% CO_2. In all cases, bacteria were enumerated using Incyto C-Chip disposable hemocytometers (SKC Inc.). All measurements were performed in triplicate and the average was reported or used to normalize material for downstream analysis.

The entire genome of each *B. burgdorferi* strain was sequenced to confirm 1) plasmid content; 2) clean deletion of A3/*chbC* ; 3) A3/*chbC* is free of polar mutations*;* and 4) clonality (see Table S4). After harvesting and washing cells from 40 mL cultures (~2 x 10^9 cells) with PBS, genomic DNA was purified using quick-DNA miniprep plus kit (Zymo Research) following manufacturers recommended procedures. Purified DNA was sequenced and assemble by Microbial Genome Sequencing Center (Pittsburgh, PA). Reads were analyzed using *breseq*[67], freely available online at http://barricklab.org/breseq) to align Illumina reads with reference genome. We ran *breseq* separately for each of three strains to identify base pair substitutions and plasmid profiles relative to the reference genome *B. burgdorferi* B31 clonal isolate 5A3 (RefSeq GCF_000008685.2). Outputs were analyzed manually and summarized in Supplemental Tables S1-4. Raw data are available upon request.

For peptidoglycan (PG) purification with all samples, cells were harvested when cultures reached a density of ~ 5x10^7 cells/mL by centrifugation at 3,500 x g for 15 mins at 4°C. The resulting pellet was gently washed three times with PBS before being centrifuged at 3,000 x g for 15 mins at 4°C. Whole cell lysate pellets were stored at -20°C for later use. For direct comparative purposes (A3 vs A3/*chbC*), cells were enumerated, and PG was extracted (see below) from equivalent cell counts (5 x 10^7 cells/mL).

Peptidoglycan isolation: intact peptidoglycan sacculi

PG was isolated and purified from 0.5 - 2 L of mid-log phase cultures; volumes depended on application. Regardless of culture volume or bacterial species, all PG was prepared as follows. Whole cell pellets were acquired by centrifugation, and washed, as described above. Cell pellets were resuspended in 10 mL PBS and added dropwise to 10 mL of boiling (150°C) 10% SDS (v/v),

which was vigorously mixed throughout the solubilization step. The final concentration of SDS after sample addition was 5% (v/v). After all material, with the exception of PG, was solubilized, the solution was boiled for 1 h at 150°C. The solution was cooled to slightly above room temperature, brought up to 23 mL final volume with ultrapure water (50°C), and insoluble material pelleted at 275,000 x g for 45 mins at 30°C. Solubilized supernatant was removed, 23 mL of ultrapure water (50°C) was added, and centrifugation step repeated. This washing step, to remove SDS, was repeated four additional times. The final pellet was subsequently resuspended in 500 µL of PBS containing 240 µg/mL Chymotrypsin, 1 mM HCl, 2 mM $CaCl_2$ and incubated while shaking (540 rpm) overnight at 37°C. Chymotrypsin digested material was solubilized by the heating the mixture at 80°C for 30 mins in 0.5% SDS (final concentration). Purified PG was harvested by centrifugation, as described above, and washed three times with 23 mL of ultrapure water (50°C). The final pellet, containing intact PG sacculi, was resuspended in 495 µL ultrapure water. Intact PG sacculi were stored at 4°C for AFM analysis or used to generate digested muropeptides as described in the following sections.

Peptidoglycan processing for muropeptide analysis

Intact PG sacculi, resuspended in $NaHPO_4/NaH_2PO_4$ buffer (5mM, pH 5.5) containing mutanolysin (7.8 µL, 4000 U/mL; Sigma-Aldrich), and digested overnight at 37°C with shaking (540 rpm). The following morning, an additional 7.8 µL mutanolysin was spiked in and allowed to incubate, shaking, for 5 h at 37°C and 540 rpm. The mutanolysin digest was then heat inactivated at 100°C for 10 mins. Following heat inactivation, the digest was cooled to room temperature and centrifuged at 22,000 x g for 30 mins. The supernatant (containing digested PG muropeptides) was

carefully moved to a pre-weighed microfuge tube without disturbing the pellet (undigested PG). The supernatant, containing digested muropeptides, was dried and final weight determined.

Purified, dried muropeptides were fully dissolved in 150 µL of saturated sodium borate buffer pH 9.25. Sodium borohydride or borodeuteride (50 mg) was dissolved in 500 µL of LCMS-grade H_2O, and an aliquot (50 µL) was added slowly to the muropeptide solution with mixing after the addition was complete. The reduction was quenched after 1 h by the addition of LCMS-grade formic acid (~10 uL) to a pH of ~ 3 as evaluated by pH paper. Samples were then immediately snap frozen and dried using a high vacuum line equipped with a liquid nitrogen solvent trap. Dried samples were stored desiccated until analysis, which involved reconstitution in H_2O:MeCN (200 µL, 9:1 v/v) containing 0.1% formic acid. Reconstituted samples were sonicated in a water bath for 10 mins and centrifuged at 4°C (13,000 x g, 10 min). From the centrifuged sample, 180 µL was placed in a labeled LC-MS vial for analysis.

LCMS Analysis

Analyses were performed on a Shimadzu LCMS9030 QToF instrument interfaced with a LC-40B X3 UPLC, a SIL-40C X3 autosampler (10 °C), and a CTO-40C column oven (40 °C). Gradient separations utilized a BEH C_{18} column (2.1 x 50 mm, 1.7 µm particle size, Waters) with Solvent A (0.1% formic acid in water) and Solvent B (0.1% formic acid in MeOH) at a constant flow rate of 0.4 mL/min. Initial solvent conditions were 99:1 (A:B) which was held constant for 3 min, followed by a shallow linear gradient to 8% B at 12 min, then to 20% B at 24 min, and finally to 95% B at 25 min, which was held for 4 min. The gradient was converted to starting conditions with a one-minute gradient to 1% B (29 min), followed by a 5 min hold. Sample

injection volumes ranged from 0.5 to 20 μL. The first 1.25 min of the separation was diverted to waste to avoid reduction reaction product contamination of the mass spectrometer interface.

The mass spectrometer was operated in positive ion mode using electrospray ionization and external calibration (NaI). Interface voltage was 4.0 kV at 300 °C, with a desolvation temperature of 526 °C, and a DL transfer line temperature of 250 °C. Gas flows (L/min) were 2, 10, 10 for nebulizing, heating and drying gases, respectively. Muropeptide data were collected between 1.25-24 min using several different MS and MS/MS programs. For statistical comparisons of strains, data was collected in MS mode only, from 400-2,000 *m/z* at 0.1 Hz. Fragmentation data was collected in data dependent mode (top three) at low Q1 resolution with 3 MS/MS spectra before placement on the exclusion list (15 s exclusion time). The precursor window as set to 400-2,000 *m/z* with fragmentation data collected between 50-2,000 *m/z*, using a ramped collision energy (25V +/- 10V). Total duty cycle was 0.4 s (0.1 s/event)

LCMS Data Analytics

Shimadzu .LCD files were converted to the .mzML file format using Shimadzu LabSolutions (v 5.99 SP2). The discovery of features and associated peak areas was performed using the xcms package (v 3.13) in the R programming environment (v 4.0.3)[68,69]. The R package RamClustR (v 1.1)[70] was used to reduce spectral redundancy through the binning of the features into groups and this reduced dataset was used for further statistical analysis. Statistical analysis was performed using Metaboanalyst 4.0[71]. Principal components analysis was performed on log-transformed and pareto-scaled peak area values.

To determine the relative amount of Glc*N*Ac-Glc*N*Ac-anhydroMur*N*Ac (G-G-anhM) present in wild-type *B. burgdorferi* A3 and A3/*chbC* strains, we prepared six independent, 450 mL

culture volumes of BSK-II complete media. Each strain was propagated in three independent cultures and PG was purified from the same number of cells, in all six samples. Relative abundances of muropeptides were quantified from all three independent PG samples of A3 and A3/*chbC*. RamClustR was once again used as above; however, from the resulting binned dataset, data was manually curated to ensure all adducts and redundancies were successfully filtered out. For each muropeptide, from each replicate, relative abundance was calculated as the amount of muropeptide compared to the sum of all muropeptides present. These values were averaged between all three replicates of A3/*chbC* and compared to the averaged replicates of A3 for each muropeptide. This analysis was repeated on samples of *B. burgdorferi*, *B. afzelii*, *B. garinii*, and *B. hermsii* to assess G-G-anhM content, and relative muropeptide abundancies, between species.

Monosaccharide analysis

PG glycosyl composition analysis was performed by the Complex Carbohydrate Research Center (Athens, GA). PG was purified, as described above, from two independent of *E. coli* K-12 and *B. burgdorferi* 5A11 cultures. Each sample were spiked with 20 µg of *myo*-inositol (internal standard) and hydrolyzed (200 µL 6 N HCl, 100 °C, 16 h). After solvent removal under a stream of nitrogen, glycosyl composition analysis was performed by combined gas chromatography/mass spectrometry (GC-MS) of the alditol acetates (AAs) as described by previously[72]. The samples were hydrolyzed again in 2 M trifluoroacetic acid (TFA) for 2 h in a sealed tube at 120 °C, reduced with $NaBD_4$, and acetylated using acetic anhydride/pyridine. The resulting alditol acetates were analyzed by GC-MS analysis on an Agilent 7890A GC interfaced to a 5975C MSD, electron impact ionization mode. Separation was performed on a 30-m Equity 1 capillary column. Alongside the samples, standards of Glc*N*Ac, Gal*N*Ac, Man*N*Ac, and Mur*N*Ac were also analyzed.

NMR Spectroscopy

Muropeptide samples and a chitotriose standard were reduced with $NaBH_4$ as described above, followed by removal of reaction by-products using gravity-fed size exclusion chromatography (1 x 20 cm column, 15 mL Bio-Gel P-2 media, fine-grade) using a 9:1 v/v mixture of water:95% ethanol (food grade/glass distilled) as mobile phase. Muropeptide fractions (~0.5 mL) were collected manually and combined after assessment by UV absorption (DeNovix DS-11 FX+) and LC-MS. Combined fractions were snap frozen, dried, and freeze dried once with 100% D_2O prior to NMR. Samples (unlabeled muropeptides, ^{13}C-labeled, and chitotriitol) were dissolved in 100% D_2O, placed in a standard NMR tube (unlabeled and chitotriitol) or a Shigemi tube (^{13}C-labeled) and analyzed on a Bruker Biospin600 MHz instrument. Standard pulse sequences were used for ^{1}H, ^{13}C, COSY, gH2BC, gHMBC, and gHSOC. Data was processed using MestReNova (v14.2, Mestrelab Research).

Stress tests & plate recovery assay in B. burgdorferi

Wild type *B. burgdorferi* 5A3 and 5A3/*chbC* strains were cultured to a final density of $5x10^7$ cells/mL and back-diluted to a concentration of 10^6 cells/mL in 5 mL in BSK-II complete culture media. NaCl (Affymetrix) and Lysozyme (Sigma-Aldrich) were added to a final concentration of 0.25 M and 1 mg/mL, respectively — one treatment per tube, per strain — and incubated for 24 h at 37°C and 5% CO_2.

Four batches of 100 mL BSK plating media was prepared as previously described[73] and added to four 100 mL volumes of pre-equilibrated, 5% low-melt agarose solution (1:1 ratio). The resulting solution was then allowed to re-equilibrate to 48°C in the water bath and will be referred to as the plating media hereafter. The plating media was poured — 25 mL per plate, 4 plates per

batch of plating media, for 16 plates — and allowed to solidify at room temperature for 2 h. The media poured constitutes the bottom layer. The top layer consisted of an equal amount of culture media, which was inoculated in a serial dilution of each strain, for each treatment. After 9 days, the colony forming units (CFUs) were determined using a magnified petri dish light box, fit with a grid.

The serial dilution replicates for each strain and treatment were normalized by cell inoculum concentration, to the highest concentration, and reported as total CFUs observed. Differences in total CFUs were compared using a two-tailed, unpaired t-test and graphed in GraphPad Prism 9.0.

Swarm/motility assay

To evaluate the motility of *B. burgdorferi* 5A3 and 5A3/*chbC* strains, we prepared solid media as described above, but with the following modifications: 1) the final concentration of low melt agarose was adjusted to 0.5% (w/v) and 2) the entire volume plating media was added at once (i.e., no layering) and allowed to solidify for 4 h at room temperature. After the plates solidified, we sub-surface inoculated one side of each plate with 7.5 µL of the 10^9 cells/mL of 5A3, and the other with equal amounts of 5A3/*chbC*. This was repeated for a total of 5 plates.

After 5 days we measured the radius, in millimeters, of the disseminated colony in 4 different directions. These values were averaged to obtain a single, average radius value, which was recorded for both strains on each plate. Differences in the 5 average radius values for 5A3 and 5A3/*chbC* were compared using a two-tailed, unpaired t-test and graphed in GraphPad Prism 9.0.

Sample preparation, brightfield microscopy, and image analysis

The morphological differences between *B. burgdorferi* 5A3 and 5A3/*chbC* strains were evaluated using phase-contrast microscopy on fixed cells. Briefly, both strains were cultured to final density of 10^7 cells/mL in BSK-II complete culture media. Cells were fixed by adding 16% paraformaldehyde, from a fresh ampule, to a final concentration of 1.8% (vol:vol). The mixture was incubated with gentle agitation for 10 mins at room temperature, followed by 20 minutes on ice. Fixed cells were harvested by centrifugation at 3500 x g for 15 mins at 4°C, washed 3 times with, and resuspended in, PBS.

Fixed cells were spotted on 2% agarose (in PBS) pads, as previously described[50]. Phase-contrast micrographs were acquired on Zeiss Axio Observer equipped with an oil-immersion phase-contrast objective Plan Apochromat 100x/1.45 N.A. (Nikon) using a Hamamatsu Orca-Flash 4.0 V3 Digital CMOS camera. Image acquisition occurred on the same day, using the same agarose pad, which was split in half. Cell preparation, image acquisition, and analysis was repeated to ensure reproducibility. Results from independent experiments were near identical, and thus, results from one experiment were reported.

We attempted to use the automated cell detection software Oufti[74] as has been done in the past for *B. burgdorferi* phase-contrast micrographs[50]. However, the gross morphological changes (Fig. 5) in 5A3/*chbC* made cell detection challenging. We opted for an alternative approach whereby a threshold was applied to each phase-contrast micrograph, using Fiji. This resulted in clear cell outlines, with clean cell boundaries, for virtually all cells in a field of view (see Fig. S34 for example). After semi-automated cell detection, we used the macro function *Roundness* to calculate differences in cell shape. Here, the cell area is fit to an ellipse, normalized by the aspect ratio of the object— an established method to evaluate the differences in the area a cell occupies[75].

Values were attained from ≥ 300 cells for each experiment, binned, and reported as frequency. ANOVA was used to calculate differences between strains and graphed; both of which were performed using GraphPad Prism 9.0.

Atomic Force Microscopy (AFM)

A suspension of purified PG (see above), isolated from *B. burgdorferi* 5A3 and 5A3/*chbC,* was created with ultrapure water, diluted 1:5, and 50 μL was deposited onto a freshly cleaved mica sheet (10 mm diameter) attached to a metal AFM sample puck with epoxy. Samples were incubated for 5 min before being dried with Nitrogen Gas. All images were acquired using a Jupiter-XR AFM (Oxford Instruments Asylum Research, Goleta CA) operating in Amplitude Modulate Frequency Modulated (AMFM) Mode with an AC160TS-R3 (Olympus) cantilever. Cantilever oscillation was produced using photothermal excitation. The cantilevers first Eigen Mode and second Eigen Modes were tuned to free amplitudes of 2 and 0.025V respectively. The setpoints were established to achieve a phase angle <90 degrees (repulsive regime) to permit Stiffness Image acquisition; typically, 1.5 and 0.018V respectively. Stiffness Values were calculated using the Hertz Contact Model assuming the radius of contact being 8 nm. Prior to image acquisition, the cantilever spring constant was calibrated using Asylum Research's GetReal Calibration Software API. Raw data files were processed and analyzed using Gwyddion. Height and stiffness measurements were compiled in Gwyddion and results graphed using GraphPad Prism 9.0.

Escherichia coli strains and growth conditions

The *B. burgdorferi* native gene *bb0718* was isolated and cloned into a pET200 plasmid — a lac operon inducible plasmid containing both kanamycin resistance and an N-terminal His tag

sequence. This plasmid was subsequently transformed into LOBSTR *E. coli* — a protein expression strain conferring chloramphenicol resistance — and the resulting lobster/*bb0718 E. coli* strain was used in all experiments regarding BB0718. In addition, an empty pET200 plasmid was transformed into LOBSTR *E. coli*. The resulting strain, hereafter referred to as LOBSTR/empty *E. coli*, served as a control for the experiments regarding BB0718. Successful transformation of both the LOBSTR/pET200::$bb0718^{Bb}$ and LOBSTR/pET200::empty *E. coli* was gauged through selection with 50 µg/mL kanamycin and 30 µg/mL chloramphenicol on LB agar plates. Resulting colonies were analyzed via PCR to verify the insertion of *bb0718* and the empty vector.

Gibson cloning was utilized to create a fluorescent mCherry-BB0718 fusion as previously described[76]. DH5α *E. coli* were transformed with pBSV2::mCherry-*bb0718* yielding DH5α/pBSV2::mCherry-*bb0718 E. coli* — an *E. coli* strain capable of expressing *bb0718* with an N-terminal translational fusion to mCherry. Successful transformation was assessed via selection with 50 µg/mL kanamycin on LB agar plating media followed by colony PCR analysis.

Regardless of strain, *E. coli* were grown in Terrific Broth (TB, Genesee Scientific Corp.) + 10% (TB+K) in an orbital shaking incubator at 30°C and 200 rpm. *E. coli* strains were grown, with appropriate antibiotic selection, to an OD (600 nm) of ~0.35 before induction with Isopropyl β- d-1-thiogalactopyranoside (IPTG) as explained below.

Colony PCR

To verify the retention of plasmid inserts, recently transformed *E. coli* were plated on LB agar plates with appropriate antibiotic selection and allowed to incubate for 24 h at 37°C. The resulting colonies were selected at random for analysis. A single swab of colony was added to a reaction mixture containing: 1x Standard Taq Mg-Free reaction buffer, 1.5 mM $MgCl_2$, 0.8 mM

dNTPs, 0.5 µM forward & reverse T7 primers, and 1% (v/v) Taq polymerase (all products New England Biolabs). The reaction was then marked up to 25 µL with ultrapure water. This process was repeated for each colony of interest. The negative and positive control contained ultrapure water and digested plasmid instead of DNA from a colony, respectively. Each reaction mixture received a 5 min denaturation at 95°C, followed by 30 cycles of: 30 s at 94°C, 30 s at 48°C, and 135 s at 70°C. Following PCR, samples were mixed with purple loading dye (New England Biolabs). Samples were loaded into a 1% agarose gel containing 0.1% ethidium bromide and were ran at 125 V, constant amplitude, for 1 hour, submerged in TAE, before imaging in a G:Box imaging system (Syngene).

Induction optimization and expression conditions in E. coli

Starter cultures of LOBSTR/pET200::*bb0718 E. coli* were grown overnight. The following day, cultures were back-diluted 1:500 and grown to an OD (600 nm) of 0.35. From this culture, 200 µL was aliquoted into each well of a 96-well plate, containing a serial dilution of 0.0078 to 4 mM IPTG. Each concentration of IPTG was tested in duplicate for three separate isolates of LOBSTR/pET200::*bb0718 E. coli* isolated from the original, successful, transformation experiment above. The plate was allowed to incubate, shaking for 18 h at room temperature in a Synergy H1 plate reader (Biotek) and OD (600 nm) was recorded every 6 min. The optimal IPTG induction concentration was found to be 1 mM and was used thereafter. For all following experiments, *E. coli* were grown to an OD (600 nm) of 0.35 before induction at 1 mM IPTG at 30°C for 3 h.

Protein isolation & purification

Protein isolation was performed using nickel-bead affinity chromatography to bind the His-tagged proteins of interest. LOBSTR/pET200::*bb0718 E. coli* (1.8 L) were harvested after induction with 1 mM IPTG for 3 h. Cells were centrifuged at 4000 rpm at 4°C and gently washed with PBS, constituting one cycle. This cycle was repeated three times in total. The resulting pellet was resuspended in 40 mL of 4°C binding/washing buffer (100 mM HEPEs, 25 mM imidazole, pH 7.5) and sonicated on ice at 35% amplitude, 20 s on, 40 s off, for 15 on/off cycles. Cellular debris was pelleted at 4000 rpm at 4°C and the supernatant was transferred to a fresh 50 mL conical tube containing 500 µL of MagneHis beads. The supernatant/bead solution was allowed to incubate, rocking, for 60 min at 4°C before pulldown via magnet. The supernatant was then removed and replaced with 40 mL of fresh 4°C binding/washing buffer and allowed to incubate, rocking, for 10 min at 4°C before a 5 min magnetic pulldown, constituting one cycle. This cycle was repeated 4 times. On the final cycle, beads were resuspended in 1 mL of 4°C binding/washing buffer and transferred to a 1.5 mL conical tube before magnetic pulldown and removal of the binding/washing buffer. "Strong" binding/washing buffer (750 µL of 100 mM HEPEs, 75 mM imidazole, 100 mM NaCl, pH 7.5) was then added and allowed to incubate, rocking, at 4°C for 10 min before magnetic pulldown, constituting one cycle. This cycle was repeated twice more. After removing the final "strong" binding/washing wash, 250 µL of elution buffer (100 mM HEPEs, 500 mM imidazole, pH 7.5) was added and allowed to incubate at 4°C for 10 min. Magnetic pulldown was used to isolate the beads, while the supernatant, now containing isolated BB0718, was prepared for dialysis.

Isolated BB0718, resuspended in elution buffer, was loaded via syringe inoculation into a 20k Dalton semipermeable dialysis cassette. The cassette was then gently placed in 1 L of dialysis

buffer (20 mM Tris, 150 mM NaCl, 10% glycerol, 10 mM KCl, 1 mM $MgCl_2$, pH 6.0) and allowed to incubate, stirring slowly, at 4°C for 24 h. Following dialysis, purified BB0718 was removed from the dialysis cassette via syringe and stored at -20°C until needed.

SDS-PAGE gel and Coomassie staining

To verify the production of BB0718 in LOBSTR/pET200::*bb0718 E. coli* samples were taken from various points of the induction and isolation pathway for analysis. Samples include pre-IPTG induction, post-IPTG induction, post-affinity chromatography isolation, and post-dialysis. For each sample, volume collected was normalized to account for differences in cell density or protein concentration at that time point. Samples, along with 10% (v/v) β-mercaptoethanol and 25% (v/v) loading dye, were incubated at 100°C for 10 min before being loaded into a 10% SDS polyacrylamide gel. Separation was performed at 125 V, constant amplitude, for 1 h in a TGS running buffer (Tris base 2.5 mM, glycine 57.5 mM, SDS 2.0 mM). The resulting gel was removed from its cassette and incubated for 30 min at RT in fixing solution (10% (v/v) acetic acid, 40% (v/v) methanol, 50% (v/v) H_2O). After fixing, the gel was incubated in Coomassie blue (7% (v/v) acetic acid, 46.5% (v/v) methanol, 46.5% H_2O, 0.2% (w/v) brilliant blue) for 3 hours. The gel was then destained (10% (v/v) acetic acid, 50% (v/v) methanol, 40% (v/v) H_2O) until protein bands were apparent. Imaging was performed in a G:Box imaging system (Syngene).

Enzymatic and osmotic stress analysis in E. coli

A starter culture of LOBSTR/pET200::*bb0718 E. coli* in TB + 10% (TB+K) was grown overnight. The following day, it was back-diluted 1:500 in fresh TB + 10% (TB+K) and grown to

an OD (600 nm) of 0.25. Here, it was split into two identical cultures. One was induced with 1 mM IPTG and the other was not; both incubated, shaking, at 30°C and 200 rpm for 3 h. After this incubation, 200 µL of induced and non-induced culture was added to 7 separate wells on a 96-well plate containing a serial dilution of lysozyme, ranging from 0.038 to 2.5 mg/mL. In a separate plate, the induced and non-induced cultures had their cell concentration diluted in water, across 8 wells, ranging from a 1:1 to 1:128 dilution. These cultures incubated in their respectively conditions for 1 h. After incubation, 20 µL of induced and non-induced culture in each condition was spotted on LB agar and allowed to incubate at 37°C for 24 hours. The following day each LB plate was imaged in a G:Box imaging system (Syngene).

Microscopy & cell-length distribution analysis

LOBSTR/pET200::*bb0718* and LOBSTR/pET200::empty *E. coli* were cultured overnight in TB + 10% (TB + K) and back-diluted 1:500 in fresh TB + 10% (TB+K) the following day. At an OD (600 nm) of 0.35, both cultures were induced with 1 mM IPTG for 3 h. Post-induction, cells were gently harvested via centrifugation at 3000 rpm, and washed with PBS. 2% agarose pads were prepared, and the cells were imaged as described above. The length of 1000 *E. coli* from each sample were analyzed by Oufti as previously described[74]. Data was curated by Oufti and graphed in MatLab.

DH5α/pBSV2::mCherry-*bb0718 E. coli* were prepared and imaged as described above. Micrographs were obtained for both phase contrast and epifluorescent signal of the mCherry-BB0718 fusion product and were merged in the Zeiss Zen program.

Attribution

Multiple colleagues were involved in work described in this chapter, which is currently under review at Nature Microbiology. The authors and their contributions are as follows:

Chapter III: A tick-derived sugar shapes the unusual peptidoglycan cell-wall of *Borrelia burgdorferi*, the Lyme disease spirochete

Authors: Tanner G. DeHart, Mara R. Kushelman, Sherry B. Hildreth, Richard F. Helm, and Brandon L. Jutras

Author Contributions.

Conceptualization: TGD, RFH, BLJ

Methodology: TGD, MRK, SBH, RFH, BLJ

Investigation: TGD, MRK, SBH, RFH, BLJ

Funding acquisition: BLJ

Project administration: RFH, BLJ

Writing: TGD, RFH, BLJ

Chapter III

A tick-derived sugar shapes the unusual peptidoglycan cell-wall of *Borrelia burgdorferi*, the Lyme disease spirochete

Introduction

The peptidoglycan (PG) sacculus is an essential biopolymer that protects the cytoplasmic contents of virtually all bacterial cells. PG architecture is universal across bacterial taxa—rigid glycan strands, cross-linked by flexible peptides. PG glycan strands consist of a disaccharide repeat of *N*-acetylglucosamine (Glc*N*Ac) and *N*-acetylmuramic acid (Mur*N*Ac), where the latter provides the C3 lactyl moiety for stem peptide assembly. Glycan chain lengths are on the order of six to hundreds of disaccharide repeats, with the reducing end anomeric position terminated with a 1,6-anhydro-*N*-acetylmuramic acid residue to prevent further assembly[28]. While alterations in PG peptide chemistry are common across the bacterial domain, deviations from the repetitive β-(1-4)-linked 'Glc*N*Ac-Mur*N*Ac' disaccharide organization of glycans are not known to occur.

The spirochetal bacterium *Borrelia burgdorferi* is thought to cause more than 450,000 cases of Lyme disease each year, in the United States alone[1]. Upon transmission from an infected *Ixodes scapularis* tick, *B. burgdorferi* causes a bi-phasic infection: a relatively innocuous acute stage, followed by a severe late-stage that involves multiple organ systems[77-79]. Despite the public health burden posed by this unusual bacterium, very little is known about some of its most salient biochemical features, many of which are well described for most pathogens. For instance, the components and molecular organization of the *B. burgdorferi* PG cell-wall have not been fully elucidated. Earlier analyses found evidence for the presence of ornithine (Orn) in the PG stem peptide[46,79], as well as several unidentifiable components, including an unknown *N*-acetylated

hexose (Hex*N*Ac) linked to the Glc*N*Ac-Mur*N*Ac disaccharide in glycan strands[46]. The culprit responsible for this atypical alteration has remained unknown.

Results

B. burgdorferi PG glycan strand architecture.

B. burgdorferi lacks many biosynthetic pathways and resorts to scavenging environmental biomolecules, including the PG cell wall precursor Glc*N*Ac and, by extension, Mur*N*Ac[36]. Optimal growth thus requires that *B. burgdorferi* culture media be supplemented with Glc*N*Ac[80]. We reasoned that, by taking advantage of this auxotrophy, we may be able to substitute less common *N*-acetylated sugars to identify the unknown PG-glycan component. While *N*-acetylmannosamine (Man*N*Ac) and *N*-acetylgalactosamine (Gal*N*Ac) are capable of supporting *B. burgdorferi* growth in the absence of Glc*N*Ac (Supplementary Fig. S1 and references[81-84]), neither Man*N*Ac nor Gal*N*Ac were present in our monosaccharide analysis of purified PG (Fig. 1A). In fact, with the exception of Glc*N*Ac and Mur*N*Ac, no other Hex*N*Acs were detected in *B. burgdorferi* PG (Fig. 1A). To further understand these results, we propagated bacteria in culture media containing 1-^{13}C Man*N*Ac and analyzed the resulting muropeptide pool, obtained from purified and digested PG, by LC-MS (Fig. 1B). Compared to muropeptide samples prepared from bacteria cultured with unlabeled Glc*N*Ac (Fig. 1B), 1-^{13}C Man*N*Ac labeled muropeptides were identical and contained the expected mass shift, equally distributed across both Glc*N*Ac and Mur*N*Ac (Fig. 1B). This strongly suggested that not only are there pathway(s) capable of converting Man*N*Ac, and likely Gal*N*Ac, to Glc*N*Ac in *B. burgdorferi*, but more importantly, the unknown Hex*N*Ac may actually be Glc*N*Ac.

Previous analysis of the *B. burgdorferi* PG cell-wall used a long chromatography step to separate muropeptides followed by targeted MS. This method captured the identity of ~45% of the *B. burgdorferi* muropeptides. We aimed to develop a method that improved the speed, accuracy, and coverage with the logic that it may help elucidate the enigmatic organization of *B. burgdorferi* PG. Our new high-resolution, tandem LC-MS method determined the identity of ~80% of the entire muropeptide pool in $1/7^{th}$ the time (Fig. 1C). The liquid chromatography step separated 25 discrete peaks, which contained 17 unique muropeptides (Fig. 1C and Supplementary Fig. S2), five of which contained the Hex*N*Ac-Glc*N*Ac-Mur*N*Ac moiety (Supplementary Tables S1-3; Supplementary Figs. S8, S11, S20, S26, S29). We coupled LC-MS from $NaBH_4$ reduced muropeptides with data obtained from isotopically ($NaBD_4$) labeled reduction products to provide mass markers and increased resolution for MS^2 spectra (Supplementary Fig. S33). The latter confirmed that the unknown Hex*N*Ac was always adjacent to a Glc*N*Ac-anhydroMur*N*Ac residue, indicating that the novel structure was at the terminus of PG glycan chains (Supplementary Fig. S33). Regardless of whether *B. burgdorferi* was cultured in media containing labeled (1-C^{13} Glc*N*Ac) or unlabeled Glc*N*Ac, the resulting LC-MS traces of each sample were identical, with mass shifts confirming that the label was disposed equally between the Glc*N*Ac and Mur*N*Ac residues (Fig. 2A and B). These data further implicated Glc*N*Ac as the unknown Hex*N*Ac.

To confirm the presence of Glc*N*Ac-Glc*N*Ac in *B. burgdorferi* PG glycans, and assess the stereochemistry of the glycosidic bond, we performed a series of H-NMR experiments using the alditol of *N*,*N*',*N*''-triacetylchitotriose as a reference. *N*,*N*',*N*''-triacetylchitotriose is essentially Glc*N*Ac-Glc*N*Ac-anhydroMur*N*Ac. Due to limitations associated with both purifying *B. burgdorferi* PG and the detection limits for H-NMR, comparisons to the standard were in relation to the total muropeptide pool obtained from the 1-C^{13} Glc*N*Ac experiment and not an individual

muropeptide. Anomeric ^{1}H chemical shifts (> 5 ppm) and coupling constants (~8 Hz) combined with ^{13}C-chemical shifts at ~100 ppm firmly established all linkages as β-glycopyranosidic bonds between Glc*N*Ac residues (Fig. 2C). The only available hydroxyls for glycosidic bond formation are at positions 3, 4 and 6; with all known muropeptide linkages being (1-4)[28]. While at present we cannot exclude the non-canonical (1-3) and (1-6) glycosidic bonds, the data obtained (Fig. 2C) matches closest to that of a β-(1-4) linkage. Most importantly, our findings establish an unprecedented modification of the glycan component of a bacterial cell-wall; *B. burgdorferi* PG glycan chains terminate with Glc*N*Ac-Glc*N*Ac-anhydroMur*N*Ac (G-G-anhM).

Laboratory strains of *B. burgdorferi* are known to lose extra-chromosomal DNA during prolonged *in vitro* propagation[85]. The result is a departure from clonality, loss of some biosynthetic capacity, and avirulence[85-88]. To that end, we questioned whether PG glycan strands containing G-G-anhM was an unusual feature of our laboratory strain and/or an artifact of prolonged *in vitro* cultivation. First, we performed whole genome sequencing on three different clones: a fully infectious clone of the B31 type strain[36] with all genetic elements and has been the source of our PG thus far (strain 5A11); a fully infectious clonal derivative[85,87] of 5A11 that is often used in the Lyme disease research field (5A3); and a high passage variant of B31 that lacks many of the native plasmids and is therefore not infectious (Supplementary Table S4). Together, these three strains represent the most commonly studied of the B31 type strain. Comparative analysis of muropeptide profiles attained from all three *B. burgdorferi* clones were near identical: each containing appreciable levels of G-G-anhM (Fig. 2D). Collectively, our studies demonstrate the first modification to the disaccharide repeat arrangement in bacterial glycans— a core biological feature of *B. burgdorferi* PG that is conserved, regardless of genome content.

Alterations to G-G-anhM impacts *B. burgdorferi* physiology and cell-wall flexibility.

Where might Glc*N*Ac-Glc*N*Ac come from and what advantage(s) does it provide for the Lyme disease spirochete? *B. burgdorferi* has evolved to survive the sometimes-desperate tick midgut for months on end for the past ~40 million years[89]. Since the tick vector feeds once each life cycle, nutrient rich blood is rarely available and, once it is, the bacterium needs to be primed to make the journey from the tick midgut to the salivary glands. One of the plausible carbon source available virtually at all times in *I. scapularis* would be a usable form of chitin, since this glycomaterial is the primary component of tick peritrophic membrane[90]. *N*,*N*'-diacetylchitobiose (hereon referred to as chitobiose) is the repeat unit of chitin, a disaccharide of Glc*N*Ac with a β-(1-4) glycosidic linkage. The G-G-anhM sequence is essentially chitotriose with a 3-*O*-lactyl moiety. To assess the possibility that chitobiose is involved in *B. burgdorferi* PG biosynthesis, we studied a mutant bacterium (A3/*chbC*), which is incapable of importing Glc*N*Ac-Glc*N*Ac into the cytoplasm[66]. First, we confirmed that our parental A3 strain studied above and A3/*chbC* mutant strain were clonal, and with the exception of the hypervariable *vlsE* locus and the targeted deletion of *chbC* gene, the strains were genetically identical by whole genome DNA sequencing (Supplementary Table S5). Principal component analysis of the muropeptide profiles attained from three biological replicates — six different batches of culture media — of both the wild-type A3 and A3/*chbC* bacteria indicated homogeneity between replicates, but distinct features common to each strain, suggesting that chitobiose transport impacts PG composition (Fig. 3A). Comparative analysis of muropeptide identity and absolute abundance clearly indicated that the parental strain had significantly more PG, despite the fact that each PG preparation came from the same number of bacteria (Fig. 3B). These findings support the claim that chitobiose may be used to build the *B. burgdorferi* PG cell-wall[66,82,84] and the lack of chitobiose reduces PG levels when normalized to

the number of bacteria. Importantly, even after we normalize for the overall decrease in PG (see methods), we found that bacteria that were unable to import chitobiose from their environment had ~37% less G-G-anhM (Supplementary Table S6). These data provide evidence that one source of G-G-anhM is actually the tick-derived sugar chitobiose.

Bacteria rely on PG as an osmoprotectant and load-bearing structure. We reasoned that the collective consequences of less PG and/or G-G-anhM, at the ultra-structure and cellular level, would be severe. Atomic Force Microscopy (AFM) of purified PG sacculi showed that, relative to wild type, A3/*chbC* PG was jagged and frayed (Fig. 4A). This was apparent in all PG sacculi analyzed and dramatic at high-resolution (Fig. 4A). Gross structural defects in purified PG translated to phenotypic effects in live cells. After both strains were exposed to a finite amount of osmotic (NaCl, Fig. 4B) or PG-specific (Lysozyme, Fig. 4C) stress, the parental A3 control strain was significantly more able to withstand both (Fig. 4B and C). Together, these data highlight the importance of both chitobiose utilization, and/or incorporation, in both *B. burgdorferi* PG synthesis and homeostasis.

One of many distinguishing characteristics of the *Borrelia* genus is periplasmic flagella — a ribbon of individual flagellum that wrap around the cell cylinder and PG layer — imparting the classical flat wave morphology[42]. Each flagellum is inserted into 7-11 motors[91], which reside adjacent to each cell pole. Motor rotation produces immense torsional stress by the flagella on the PG layer, akin to wringing a wet towel, but also propels the organism up to velocities nearly 100 times faster than a human neutrophil cell; the fastest cell in the human body[92,93]. Contorting the cell cylinder with torque of this magnitude would necessitate, in theory[43], strong yet flexible PG to counteract deforming forces produced by the flagella[94]. We speculated that defects in PG continuity and/or reduced levels of G-G-anhM may alter the physical balance between PG and the

flagellar ribbon, resulting in altered morphology. Phase-contrast micrographs of individual cells show a clear discrepancy in the pitch (or trough) of the wave between wild-type A3 and A3/*chbC* strains (Fig. 5A). Morphometric, single-cell analysis, to evaluate differences in helical abnormalities between each population were determined by measuring the *Roundness*[95] or the collective area required to enclose an object in an ellipse, corrected by aspect ratio[75,96]. Population-level analysis confirmed that there was a significant amount of variability in the helical pitch of the chitobiose mutant strain (Fig. 5B). Morphological changes in helicity suggest an imbalance in PG-motility machinery homeostasis. We performed a swarm assay in which two equidistant sites on a single semi-soft agar plate were inoculated with each strain. After 5 days the radial distance was measured. While A3/*chbC* retains motility, we found a significant difference in distance confirming that cell-wall/motility homeostasis was disrupted (Fig. 5C). Our data support the theoretical model whereby *B. burgdorferi* PG hemostasis is tuned to the torsional stress created by periplasmic flagellum[97]. We extend this theory and provide a biological and chemical means by which *B. burgdorferi* has tailored its cell-wall to combat the unique forces produced by periplasmic, endo-flagella.

Thus far, we have not determined whether the phenotypic differences (Figs. 3-5) in bacteria unable to import chitobiose are solely the result of reduced levels of cellular PG (Fig. 3B) or if less G-G-anhM may alter the biophysical properties of the *B. burgdorferi* PG sacculus. In other words, has *B. burgdorferi* evolved to utilize tick-derived Glc*N*Ac-Glc*N*Ac in order to increase the distance between muropeptides, adjacent to glycan termini (Fig. 2 and Supplementary Fig. S33), thus making their PG more flexible? To address these possibilities, we performed elasticity-based mechanical measurements using AFM on purified sacculi. Comparative analysis of PG elasticity between individual sacculi appeared similar (Fig. 6A) but, in order to capture the full range of

measurements, the A3/*chbC* sample required a colormap that extended more than three times the max force of wild type sacculi (Fig. 6A). Tandem height and force map measurements, collected from 8 samples per strain (>3000 data points), corroborated that PG isolated samples with reduced G-G-anhM was, on average, 3.3 times stiffer (Fig. 6B). We note, however, that topological height mapping also showed differences in PG thickness between samples (Fig. 6C), potentially due to less total PG in A3/*chbC* (Fig. 3B). To exclude the possibility that differences in thickness were contributing substantially to elastic modulus differences, we normalized by PG thickness, and performed a relative comparison on the same eight independent sacculi per strain. Even after accounting for thickness differences, G-G-anhM content was found to directly correlate with elasticity (Fig. 2D). Together, our data support an evolutionary adaptation whereby *B. burgdorferi* has evolved to incorporate a chitin-derived disaccharide into its cell wall; effectively increasing the distance between muropeptide to provide the flexibility necessary to counteract the torsional stress it inflicts on itself.

Discussion

PG is a structural component of the bacterial cell envelope and an intense area of evolving research over the past century. This is undoubtedly because of its importance in bacterial 1) physiology; 2) morphology; 3) cell biology; 4) host interactions; and 5) control through targeted inhibition by antibiotics[28,35,98]. PG cell-wall chemistry is intimately linked to each process, but typically by way of the variability in muropeptide(s) and/or their linkages. Glycan strands stoichiometry, on the other hand, were thought to be invariable. This was the impetus for our studies— an unknown Hex*N*Ac in place of a Mur*N*Ac moiety that lacked a stem peptide[46,99], we sought to determine the structure and role of the unknown Hex*N*Ac. Our finding that PG from

multiple strains of *B. burgdorferi* contain glycans with G-G-anhM (Fig. 1D) constitute a new paradigm in bacterial cell-wall architecture.

Our in-depth, high-resolution analysis of *B. burgdorferi* PG was able of to assign muropeptide identity to 17 unique species (Fig. 1C and Supplemental Data Tables S1-3), which constitutes >80% of all PG and an improvement of >45% (Supplementary Table S1), relative to earlier studies[46]. G-G-anhM was abundant, but exclusively found at glycan termini (Supplemental Data Tables S1-3, Fig. S8, S11, S20, S26, S29), which has several important implications. First, apart from the number of peptides participating in cross-bridges[98], terminal G-G-anhM affords larger distances between adjacent peptides and a novel means to increase PG flexibility (Fig. 6). The latter is remarkable given that, on average, *B. burgdorferi* glycan strand length is 30 disaccharides[46,100] and thus, G-G-anhM can only constitute ~3.3% of all muropeptides (Supplementary Table S1-3). Next, the exclusivity of G-G-anhM position hints at a novel chemical and/or structural bias towards incorporation into the existing sacculus. Finally, since termini are also the site of new muropeptide incorporation during PG elongation, G-G-anhM may also be important in the pathogenicity of released *B. burgdorferi* muropeptides[46].

B. burgdorferi adapts to its environment by sensing environmental cues and responding[101], producing and repressing factors as needed. Production of the chitobiose transporter is upregulated under conditions similar to the tick mid-gut[82], when spirochete replication rate is slow[102] and sugar metabolism is at a premium. Others have speculated that chitobiose utilization may be necessary for cell-wall biosynthesis[66,82,84], but direct evidence was lacking. Our studies provide direct evidence that chitobiose import is an integral part of both PG composition (Fig. 3) and continuity (Fig. 4). Despite the abnormalities in cell morphology (Figs. 5A and B) and motility (Fig. 5C), chitobiose transport is not required to successfully complete the tick-vertebrate enzootic life cycle

of *B. burgdorferi*[66], but may cause a defect in fitness. Chitobiose transport accounts for ~37% of PG G-G-anhM (Supplemental Data Table S6), which is not surprising— chitobiose is not present in mammals. Thus, *B. burgdorferi* must possess additional, yet to be determined, means by which G-G-anhM is synthesized.

The evolutionary landscape of arthropods, and their resident microbial symbionts, is beginning to come into focus. Co-evolutionary adaptive mechanisms have been fine- tuned for tens of millions of years[103]. For instance, *I. scapularis* has co-opted a PG hydrolase of bacterial origins to limit *B. burgdorferi* expansion[89], while protecting itself from pathogen acquisition. Microbial communities act in concert to alter tick midgut physiology, impacting the frequency and transmissibility of its resident[104,105]. *B. burgdorferi* has foregone the need for seemingly essential vitamins like thiamine, which are likely not present in tick midguts[106]. Our findings are yet another example of how an endo-parasitic bacterium has evolved to hijack arthropod components for their own, incredibly specific, biophysical vices.

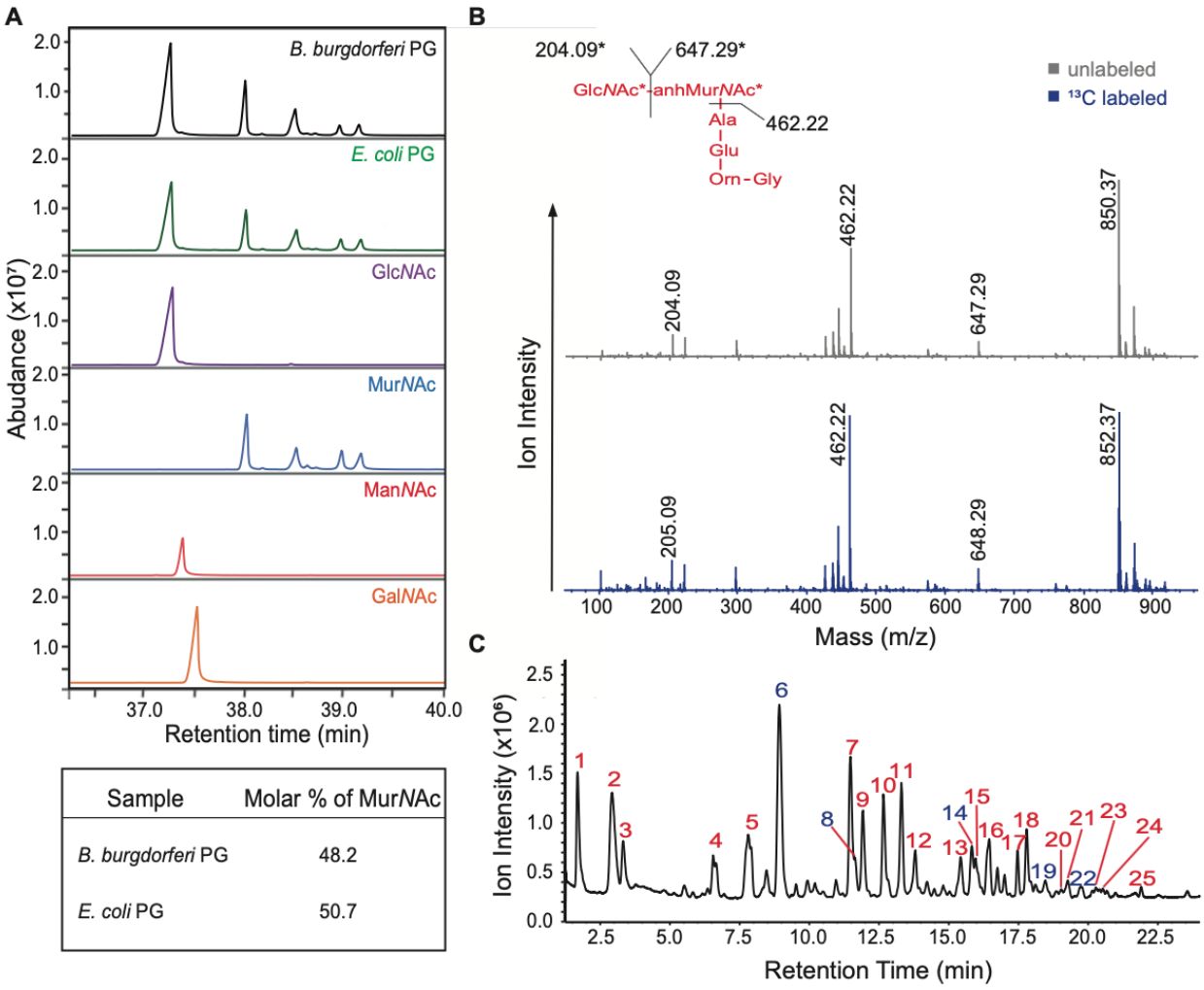

Sample	Molar % of MurNAc
B. burgdorferi PG	48.2
E. coli PG	50.7

Figure 1: Elucidating the PG glycan strand composition of *B. burgdorferi*. A) Monosaccharide analysis of purified peptidoglycan isolated from 5A11 *B. burgdorferi* 5A11 and *E. coli* K-12. Results were compared to reference standards Glc*N*Ac, Mur*N*Ac, Man*N*Ac, and Gal*N*Ac below. The inset table highlights the molar percent of Mur*N*Ac present in each bacterial sample. **B)** MS/MS of Glc*N*Ac-Mur*N*Ac-Ala-Glu-Orn ($[M+H]^+$ = 850.3718, gray) and Glc*N*Ac-Mur*N*Ac-Ala-Glu-Orn ($[M+H]^+$ = 852.3718, blue) muropeptide attained from *B. burgdorferi* 5A11 cultured in unlabeled and 1- ^{13}C Man*N*Ac, respectively. Theoretical cleavages shown on example muropeptide correspond to masses observed in MS/MS. Asterisks indicate the sugar masses increased by 1 in the 1- ^{13}C sample. **C)** Liquid chromatography mass spectroscopy (LCMS)

chromatogram of *B. burgdorferi* 5A11 peptidoglycan. *B. burgdorferi* PG was purified, digested with mutanolysin, and analyzed by LC-MS. Each peak corresponds to one or more muropeptides of interest; peaks are labeled as red (Glc*N*Ac/-Mur*N*Ac muropeptides) or blue (Hex*N*Ac-Glc*N*Ac-Mur*N*Ac muropeptides).

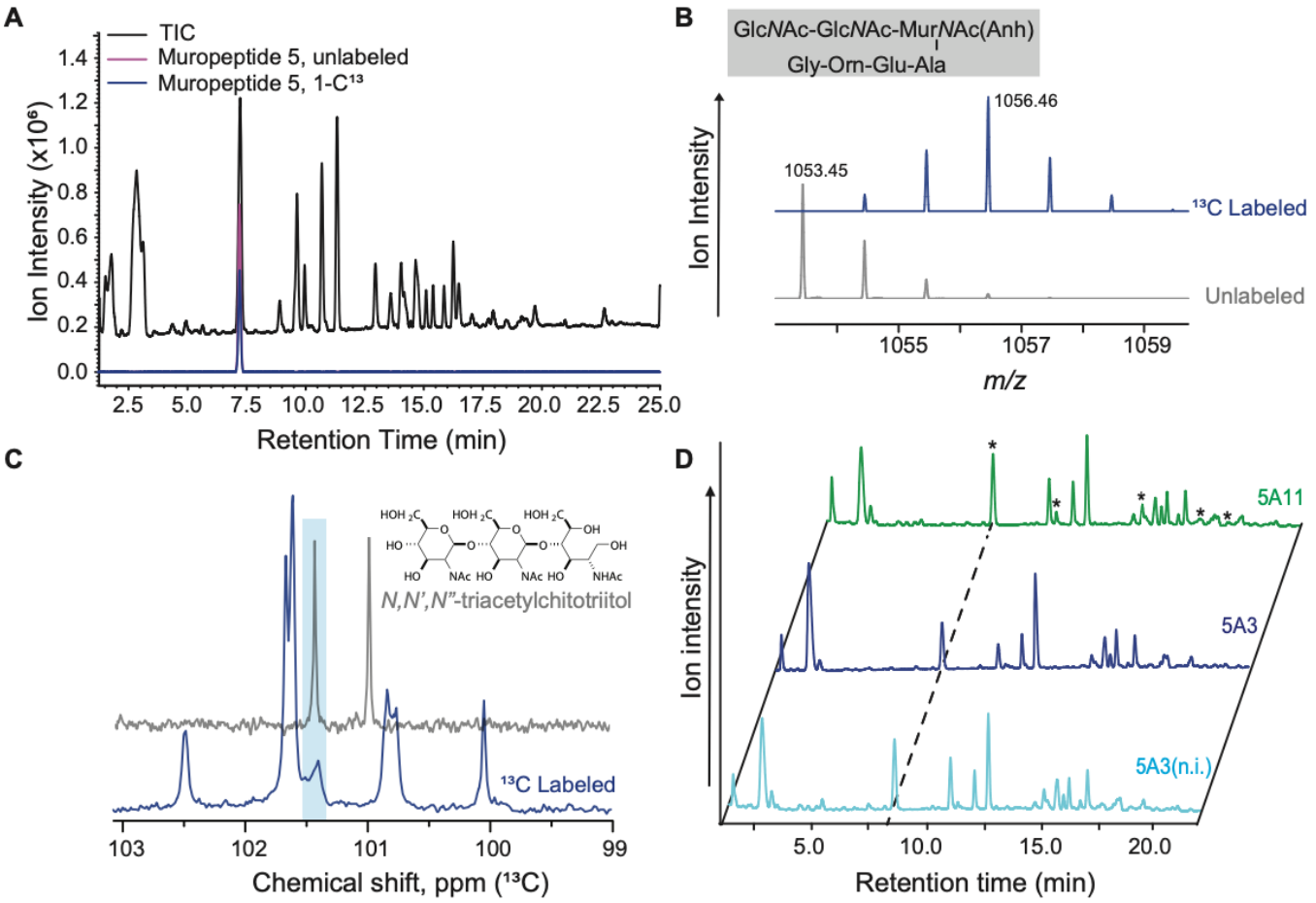

Figure 2: *B. burgdorferi* PG glycan strands contain the trisaccharide Glc*N*Ac-Glc*N*Ac-anhydroMur*N*Ac (G-G-anhM). A) LCMS chromatogram of unlabeled *B. burgdorferi* 5A11 PG. Total ion chromatogram is shown in black with an unlabeled and 1-C^{13} labeled G-G-anhM muropeptide overlaid in pink and blue, respectively. **B)** LCMS chromatogram of 1-C^{13} Glc*N*Ac metabolically labeled *B. burgdorferi* 5A11 PG produces a mass shift corresponding to a G-G-anhM muropeptide. *B. burgdorferi* was cultured with unlabeled Glc*N*Ac or 1-^{13}C Glc*N*Ac prior to PG purification and LCMS analysis. The proposed G-G-anhM species 1053 *m/z* in unlabeled PG and the shifted mass to the predicted 1056 *m/z* when labeled with 1-^{13}C Glc*N*Ac are shown. **C)** H-NMR from 1-C^{13} labeled *B. burgdorferi* PG. Chemical shifts associated with bulk muropeptide H-NMR analysis of 1-C^{13} Glc*N*Ac labeled PG, relative to a *N*,*N*',*N*"-triacetylchitotriitol reference

standard, indicate *B. burgdorferi* glycan strands contain G-G-anhM. **D)** A comparative muropeptide analysis of *B. burgdorferi* PG isolated from different strains. Three laboratory strains of *B. burgdorferi*, two fully infectious clones of the type strain (5A11, 5A3), and non-infectious (n.i.) derivative of 5A3 were cultured to mid-log, PG was purified, digested, and muropeptide profiles compared by LC. All samples contained similar levels of G-G-anhM muropeptides (*).

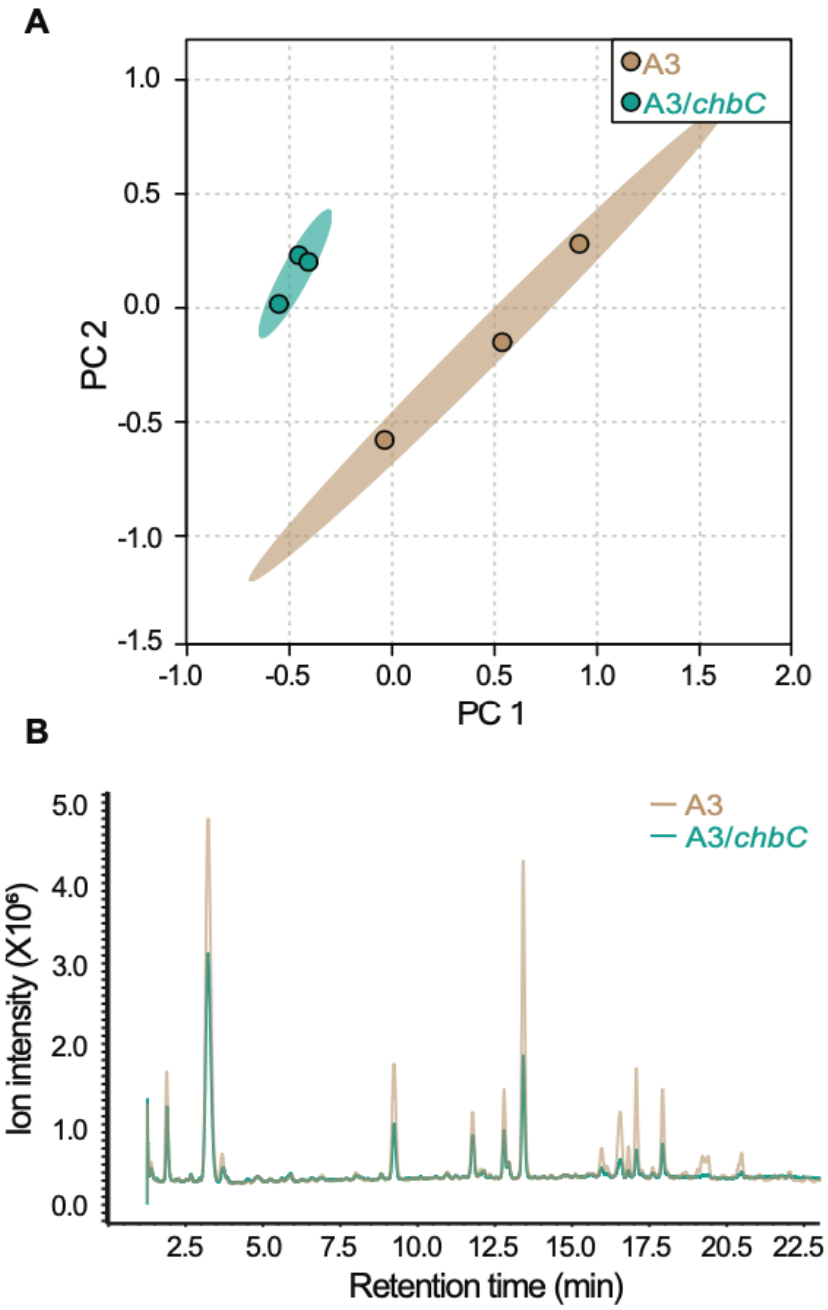

Figure 3: Comparative analysis of muropeptide profiles attained from *B. burgdorferi* A3 and chitobiose transport mutant A3/*chbC*. A) Principal component analysis of 37 distinct muropeptides features collected from LC-MS data of three biological replicates, from wild-type A3 strain (tan) and A3/*chbC* (teal) PG. **B)** Representative LC spectra from our comparative

muropeptide analysis (in **A**) in which the amount of purified and injected PG was normalized by the total number of cells present in each culture.

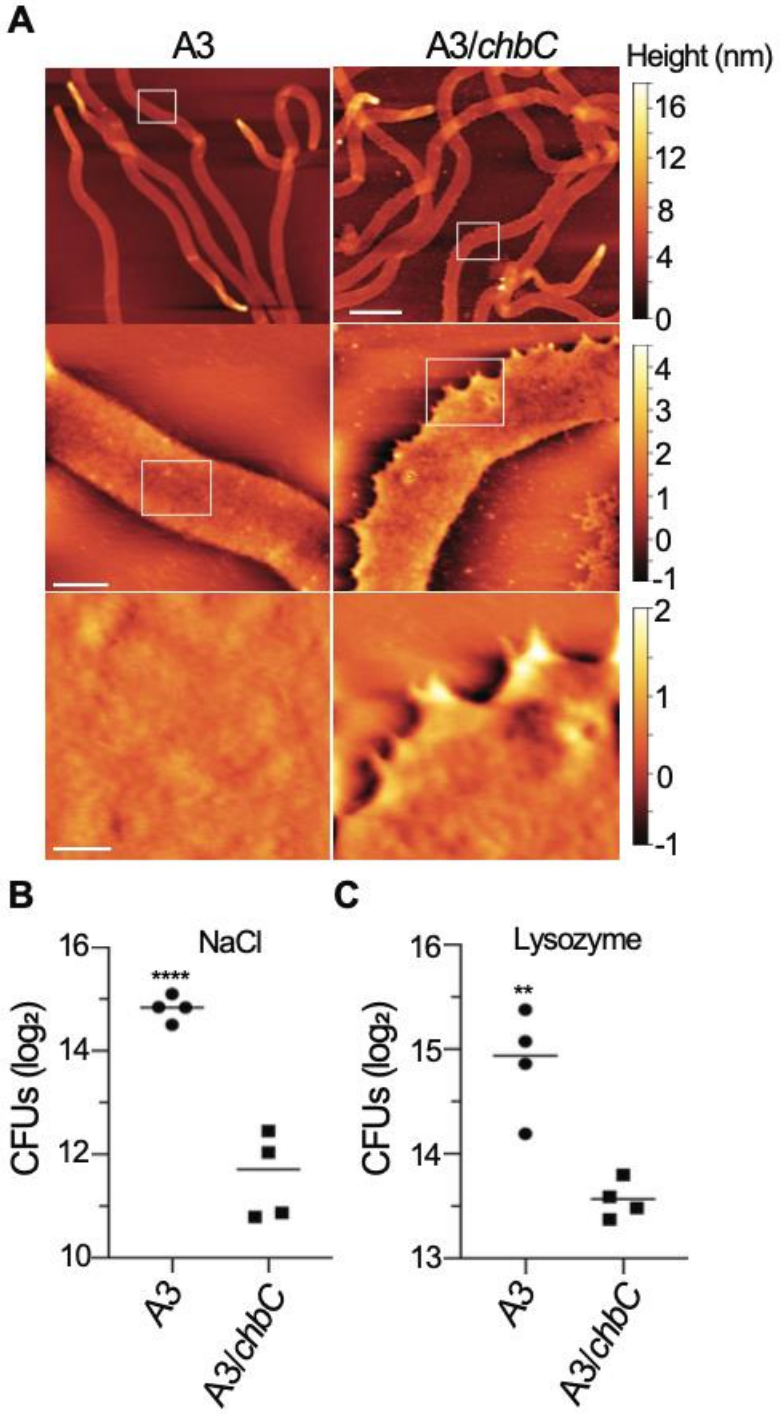

Figure 4: Impact of chitobiose (Glc*N*Ac-Glc*N*Ac) transport on PG and cell-wall stress. A) Comparative Atomic Force Microscopy (AFM) analysis of purified PG. PG from both the wild-type A3 strain and A3/*chbC* chitobiose mutant transporter strain were deposited on mica and

topological features imaged in amplitude modulate frequency modulated (AM-FM) mode. Height features for each image are shown as color maps (right). Scale bars 5 µm (upper panel), 500 nm (middle panel), and 50 nm (lower panel). **B and C)** Recovery after cell-wall stress. Wild-type A3 and A3/*chbC* strains were exposed to 0.25M NaCl **(B)** or 1mg/mL lysozyme **(C)** for 24 hours. After removing exogenous stress, cultures were plated in quadruplicate, and colony forming units were determined 9 days later. Statistical significance was determined by unpaired *t*-test (**** $p < 0.001$, ** $p < 0.01$).

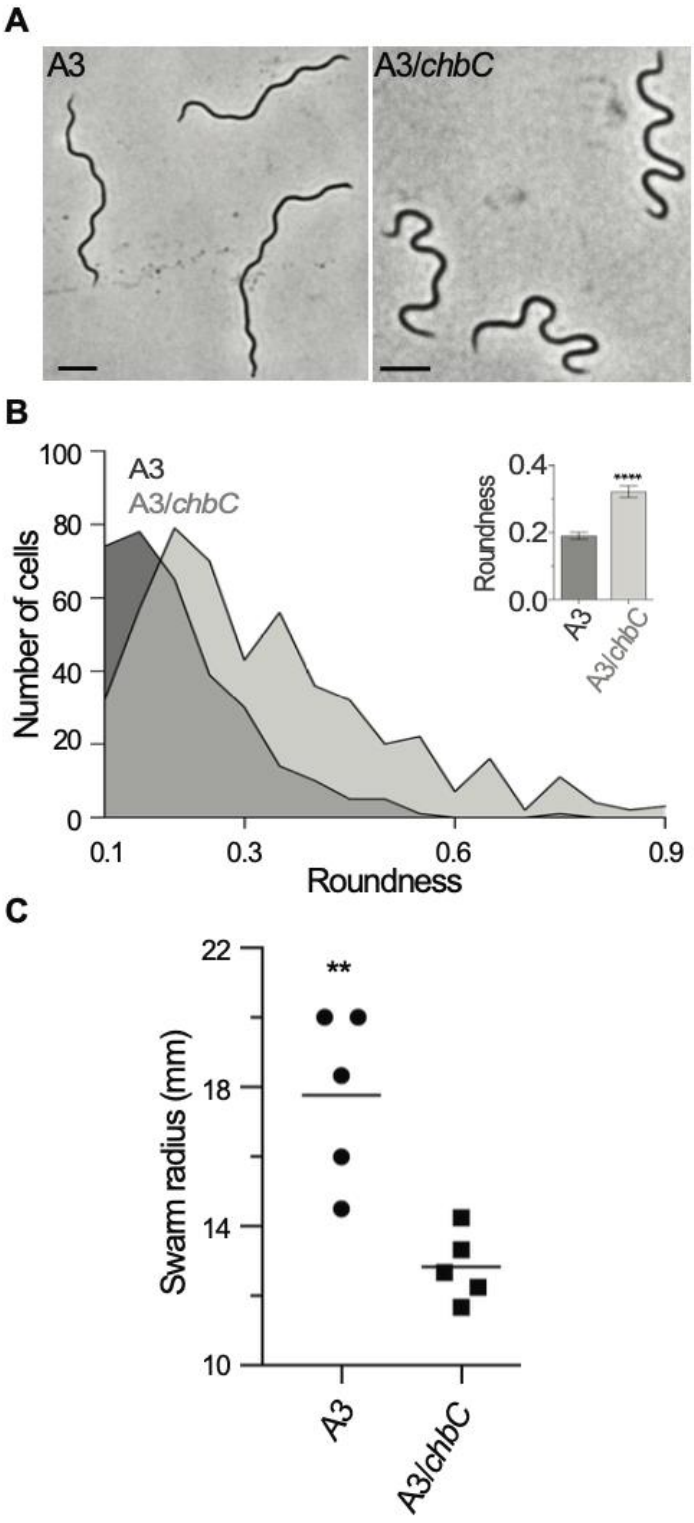

Figure 5: Morphological and motility defects in A3/*chbC* mutant bacteria. A) Comparative, quantitative, population-level morphological analysis of A3 and A3/*chbC* strains. Both strains

were cultured to mid-log exponential growth, fixed with paraformaldehyde to preserve cellular helicity, and imaged on agarose pads by phase-contrast microscopy (left, scale bar 5 µm). **B)** Morphometric, population-level analysis of differences in helical pitch between strains were estimated by the object analysis feature *Roundness*. Values, attained from n = 307 (A3) and n = 345 (A3/*chcC*) cells were binned and plotted by frequency, or as absolute values (inset). Statistical significance was evaluated by a one-way ANOVA (**** $p < 0.001$). **C)** Swarm plate assay to measure differences in bacterial motility. Liquid A3 and A3/*chcC* cultures were enumerated and equal amounts used to inoculate the same semi-soft agar plate, equidistant from one another. After 5 days swarming distance was measured from 5 replicate plates. Statistical analysis *t*-test (** $p < 0.01$).

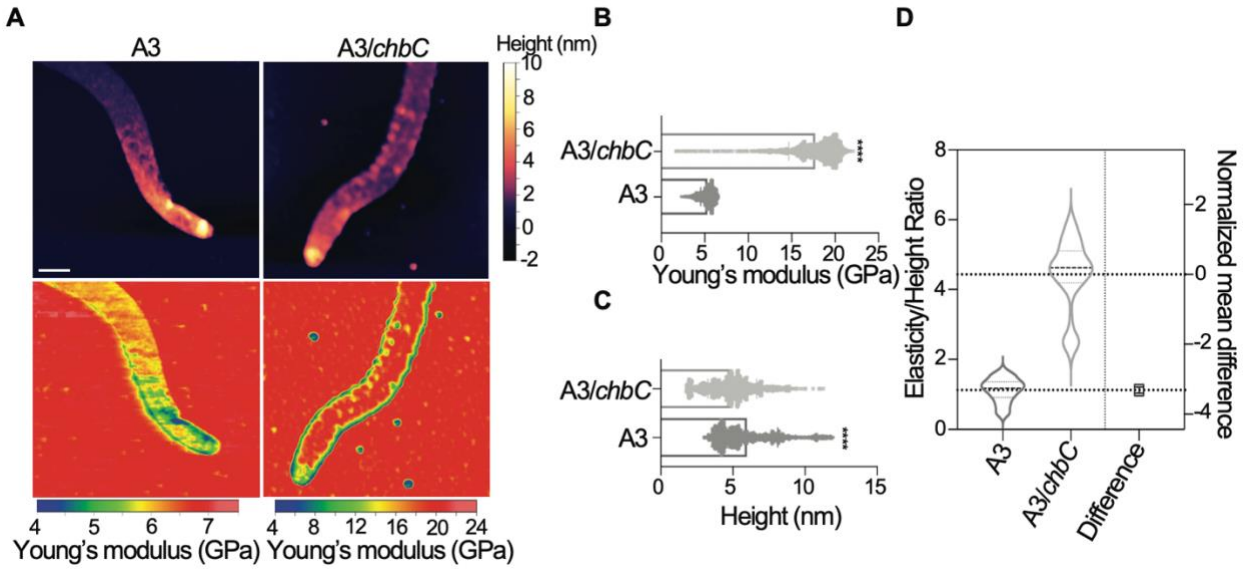

Figure 6: Biophysical properties of *B. burgdorferi* PG with reduced levels of G-G-anhM. A) AM-FM topological mapping (upper) and elasticity measurements (lower) using the Hertz Contact Model on purified PG sacculi from each strain. Note that measurements collected for each sample had dramatically different force ranges, which is reflected in color maps (below). These images are representative data collected from 8 independent sacculi per sample. Scale bar 2 µm. **B)** Line-scan analysis of force measurements were collected from each pixel (n > 3000), in 8 independent sacculi per sample. **C)** The same line-scans in **B** were used to measure pixel-level height differences in each sample. Statistical significance for panels **B** and **C** was assessed by ANOVA (**** $p < 0.0001$). **D)** Fold-change of the elasticity of A3/*chbC* PG, relative to A3, normalized by PG height.

Chapter IV

Lyme disease and relapsing fever *Borrelia* incorporate a conserved tick sugar into the glycan strands of their peptidoglycan

Introduction

Borrelia is a genus of spirochete bacteria responsible for causing a plethora of diseases in humans and animals around the world. This genus can be divided into two major groups, based on the disease state they cause: Lyme disease *Borrelia* or relapsing fever *Borrelia*[107]. Lyme disease is one of the most common tick-borne illnesses in developed northern-hemisphere countries and is transmitted by hard-bodied *Ixodes* ticks[59-61,108]. The causative agent varies with geographical location — *Borrelia burgdorferi* is the primary pathogen in the United States, while *Borrelia afzelii* and *Borrelia garinii* are responsible for the majority of cases in Eurasia[108]. Hard-bodied *Ixodes* ticks harbor Lyme disease *Borrelia* within their midguts and feed over the course of multiple days. Spirochetes travel from the midgut to the salivary glands, and eventually, into the host during this time[109]. Spirochete transmission to a host rarely occurs before 24 hours of tick-feeding has elapsed and becomes increasingly efficient as feeding progresses[109]. Relapsing fever is more common in tropical, underdeveloped and developing countries, and is caused by *Borrelia hermsii*, *B. miyamotoi*, and *B. recurrentis*, among other *Borrelia* species[110]. These particular pathogens are transmitted by the soft-bodied *Ornithodoros hermsi* tick, hard-bodied *Ixodes* tick, and the human body louse, respectively[111,112]. Outside of the two outlying species listed prior, relapsing fever *Borrelia* are almost exclusively transmitted by soft-bodied ticks. Soft-bodied ticks harbor relapsing fever *Borrelia* in their midguts upon initial spirochete infection, after which, the bacteria disseminate to various tissues, including the salivary glands[109,112]. These ticks feed in only

15 to 90 minutes; yet, are still infectious due to the spirochetes actively residing within their salivary glands, among other mechanisms[109].

As members of the same genus, the genomes of Lyme disease and relapsing fever *Borrelia* are relatively conserved[57]; yet, their disease manifestations are very diverse, even between members of the same group. For example, *B. burgdorferi*, *B. afzelii*, and *B. garinii* all cause Lyme disease, but typically manifest as Lyme arthritis[21], acrodermatitis[62], and neuroborreliosis[63], respectively. The relapsing fever *Borrelia* share similar distinctions, as fever duration, time between episodes, and occurrence of neurological manifestations vary between species[111,113]. While the clinical manifestations of each *Borrelia* species are well documented, little information exists explaining the variation in disease states between, and within, *Borrelia* subgroups.

One possible explanation for the disparity between disease manifestations could be differences in peptidoglycan and muropeptide profile between species. Previous studies have shown that PG from *B. burgdorferi* is capable of inducing arthritis in a murine model just 24 hours post-injection[46]. This suggests that *B. burgdorferi's* PG alone is capable of mimicking the disease manifestation associated with infection in a host. However, it is not known if PG composition between *Borrelia* species varies or if they share this pathogenicity and are capable of recapitulating disease states in a host. To answer these questions, we aim to provide a characterization of muropeptide profile in both Lyme disease and relapsing fever *Borrelia*.

Our work here is a continuation of the previous chapter and resulting published work. After observing, and characterizing, the inclusion of Glc*N*Ac-Glc*N*Ac in the glycans of *B. burgdorferi* PG, we sought to analyze the PG composition of other Lyme disease and relapsing fever spirochetes. In addition, an in-depth analysis of muropeptide profile may explain, in part, the great disparity between infection with various *Borrelia* species.

Results

Different *Borrelia* species contain conserved elements, but vary in overall PG composition

In hopes of providing a parsimonious explanation for the high degree of similarity between genomes, yet vast disparity between disease manifestations, we analyzed the PG composition of various *Borrelia* species. PG isolated from *B. burgdorferi*, *B. afzelii*, *B. garinii*, and *B. hermsii* was analyzed via LCMS; the resulting chromatograms are shown in Figure 7. The chromatograms all share a high degree of similarity suggesting many muropeptides may be conserved between *Borrelia* species. However, some differences in peaks are apparent.

The likeness of PG between *Borrelia* species, in triplicate, was analyzed (Fig. 8). The PG of each individual *Borrelia* species was found to cluster tightly within technical replicates. Separate species were easily differentiable from one another, suggesting that PG composition does vary between *Borrelia* species (Fig. 8). To further compare the PG profile between species, on a holistic level, a hierarchical clustering analysis was performed (Fig. 9). PG composition of *B. burgdorferi* and *B. garinii* were found to more closely resemble one another than that of *B. afzelii*, which was more similar to *B. hermsii* (Fig. 9). Although *B. burgdorferi*, *B. garinii*, and *B. afzelii* are all Lyme disease *Borrelia* who share a relatively conserved genome[57], *B. afzelii's* PG composition was more reminiscent of *B. hermsii*. While this suggests the PG of Lyme disease-causing *B. afzelii* is more similar to the relapsing fever spirochete *B. hermsii*, the analysis was performed holistically, at the total PG profile level. To better visualize differences in muropeptide profile between the *Borrelia* species, untargeted metabolomics data were gathered and concatenated into 47 distinct "features". Each feature consists of a retention time and at least two peaks with an individual *m/z* value and corresponding intensity. These features were manually assigned to matching previously identified muropeptides in *B. burgdorferi* using the *m/z* and

retention time data from each feature, when possible (Table 1; feature information shown in Supplemental Dataset 2). We were able to identify at least 73.2%, 76.0%, and 75.0% of *B. garinii*, *B. afzelii*, and *B. hermsii*'s muropeptide composition, respectively (Table 1). All samples were normalized to the sample with the lowest total PG present (*B. burgdorferi*, technical replicate 3). Percentages represent the average amount of PG we could identify in each species' replicates using our previously identified *B. burgdorferi* PG profile as a reference. Compared to our previous analysis of *B. burgdorferi* PG (Chapter III) which identified ~80% of muropeptide composition, here we identified ~69%. This decrease is likely a result of broadening our parameters to include all four *Borrelia* species rather than narrowing our focus to a single one (as demonstrated in Chapter III). The two *Borrelia* species containing the most similar muropeptide abundancies for each muropeptide are bolded (Table 1). Each muropeptide species contributing > 0.2% of total PG in Table 1 was normalized to the total amount of that muropeptide across all species, after which all muropeptide species normalized were assessed via heatmap (Fig. 10a). The normalized muropeptide abundancies were found to be most similar between *B. burgdorferi* and *B. garinii* and also between *B. afzelii* and *B. hermsii*, reinforcing our previous findings (Fig. 10a). Although these trends were observed, a preliminary assessment suggests normalized muropeptide abundances were different in the *Borrelia* species analyzed (Fig. 10b). Further studies will quantitatively evaluate the significance of these observed differences.

Lyme disease and relapsing fever *Borrelia* incorporate Glc*N*Ac-Glc*N*Ac-anhMur*N*Ac into their PG

We previously characterized the first known deviation in PG backbone architecture — Glc*N*Ac-Glc*N*Ac-anhydroMur*N*Ac in *B. burgdorferi* PG. However, we were left wondering if this

trait was unique to *B. burgdorferi*, or if it represents a genus-wide evolutionary adaptation to life inside a tick. To answer this question, PG from two additional Lyme disease *Borrelia* and one relapsing fever *Borrelia* was isolated and analyzed — *B. afzelii*, *B. garinii,* and *B. hermsii*, respectively. PG from *B. burgdorferi* was also included to serve as a reference for baseline Glc*N*Ac-Glc*N*Ac incorporation.

Each *Borrelia* species analyzed incorporated an appreciable amount of G-G-anhM into their peptidoglycan (Table 1). These G-G-anhM muropeptide species appeared to be the same as those identified in *B. burgdorferi*, based on *m/z* and retention time, and their relative abundance was found to vary between *Borrelia* species. G-G-anhM was found to constitute 0.5%, 1.1%, 0.6%, and 0.8% of total PG in *B. burgdorferi, B. garinii, B. afzelii, and B. hermsii*, respectively. The lower G-G-anhM abundance reported for *B. burgdorferi* in this experiment is likely a result of broadening our parameters to include other *Borrelia* species. In addition, differences in culture media composition (BSK-H in this experiment, BSK-II in Chapter III) may play a role in the uptake of sugars and incorporation of G-G-anhM into the PG. The reported values are relative, based on normalization between samples in an experiment, and cannot be directly compared to previous experiments. Nevertheless, our data suggest that *B. garinii*, *B. afzelii*, and *B. hermsii* incorporate similar, if not greater, amounts of G-G-anhM into their PG, relative to *B. burgdorferi*.

Occurrence of PG crosslinking varies between *Borrelia* species

In addition to variations in G-G-anhM incorporation, the relative abundance of the other muropeptides varied between *Borrelia* species as well (Table 1, Fig. 10a &b). Uncrosslinked muropeptides, such as muropeptide 1, 2, and 6 were found to vary in relative abundance by as much as 7% between *Borrelia* species (Table 1). The relative abundance of crosslinked

muropeptides, such as muropeptides 11 and 12, varied by much less, up to ~2% at most (Table 1). Differences in the abundance of G-G-anhM, crosslinked, and non-crosslinked muropeptides may play a role in many aspects of the biology of these pathogenic *Borrelia* species.

We previously demonstrated that G-G-anhM represents a novel means to increase the flexibility of *B. burgdorferi's* PG sacculi to better compensate for self-inflicted torsional stress. Other studies have shown that variations of crosslinking abundance in PG produces a similar effect on the strength of a sacculi[28]. Therefore, the observed differences in both G-G-anhM and crosslinking abundance are likely the result of each *Borrelia* species fine tuning its respective PG sacculi to best fit its specific needs. Further studies will better quantify the differences in, and abundance of, muropeptide crosslinking in *Borrelia* species.

B. burgdorferi has been shown to release its PG into the environment, rather than recycle, where it elicits a strong immune response in a host[46,47]. It is also known that crosslinked and non-crosslinked PG are recognized by the immune system in different ways[35,114]. Given G-G-anhM's exclusivity to glycan termini, and therefore the site of muropeptide incorporation, it may play a role in the pathogenicity of released *B. burgdorferi* PG. Furthermore, the abundance of crosslinked and non-crosslinked muropeptides released may also impact this pathogenicity. Continued studies will evaluate if other *Borrelia* species release muropeptides and to what extent their PG composition, and crosslinking abundance, affects pathogenicity.

While differences in the quantity of crosslinked PG were observed, differences in peptide chains involved in crosslinking could not be determined due to previously characterized muropeptide isomers (Supplemental Table S2). Our analyses reinforced our findings that *Borrelia* species utilize conserved muropeptides but differ in overall composition, which may play a role in the structure, function, and pathogenesis of *Borrelia* PG.

Discussion & Future Plans

Here we have 1) provided the first in-depth characterization of muropeptide profiles in *B. garinii*, *B. afzelii*, and *B. hermsii*, 2) demonstrated each *Borrelia* species analyzed incorporated appreciable amounts of G-G-anhM, and 3) reinforced the aforementioned claim that while *Borrelia* strains utilize the same muropeptides in their PG, they do so in different quantities, likely by varying the amount of crosslinking in their peptide chains. Our studies show that incorporation of G-G-anhM is highly conserved and may represent an evolutionary adaptation to life inside a tick. However, we were left with two further questions that we hope to address in the near future. 1) Could incorporation of G-G-anhM potentially pre-date the evolutionary divide between Lyme disease and relapsing fever *Borrelia*? And, 2) Does G-G-anhM incorporation expand outside of tick-borne *Borrelia*?

To address these questions, PG from two additional *Borrelia* species — *Borrelia mayonii* and *Borrelia reccurentis* — will be isolated and analyzed in a similar fashion to our previous studies. Native to the midwestern United States, *B. mayonii* is a relatively newly discovered, highly infectious, Lyme disease spirochete that resides within *I. scapularis*[115], the black-legged tick. We hypothesize that if muropeptide composition plays a role in pathogenesis, such a highly infectious species of *Borrelia* would have a relatively unique muropeptide profile. The relapsing fever spirochete, *B. reccurentis*, however, is spread by *Pediculus humanus corporis*, the human body louse[116]. Collectively, these represent distinct Lyme disease and relapsing fever *Borrelia* from both a hard-bodied tick and louse vector, respectively. When combined with our previous studies, we will have analyzed PG from Lyme disease and relapsing fever *Borrelia*, while also encompassing all known vectors — both hard and soft-bodied ticks as well as the human body louse. These

studies will allow us to assess if incorporation of G-G-anhM predates both the evolutionary divide between Lyme disease and relapsing fever *Borrelia* and expands outside of tick-borne *Borrelia*.

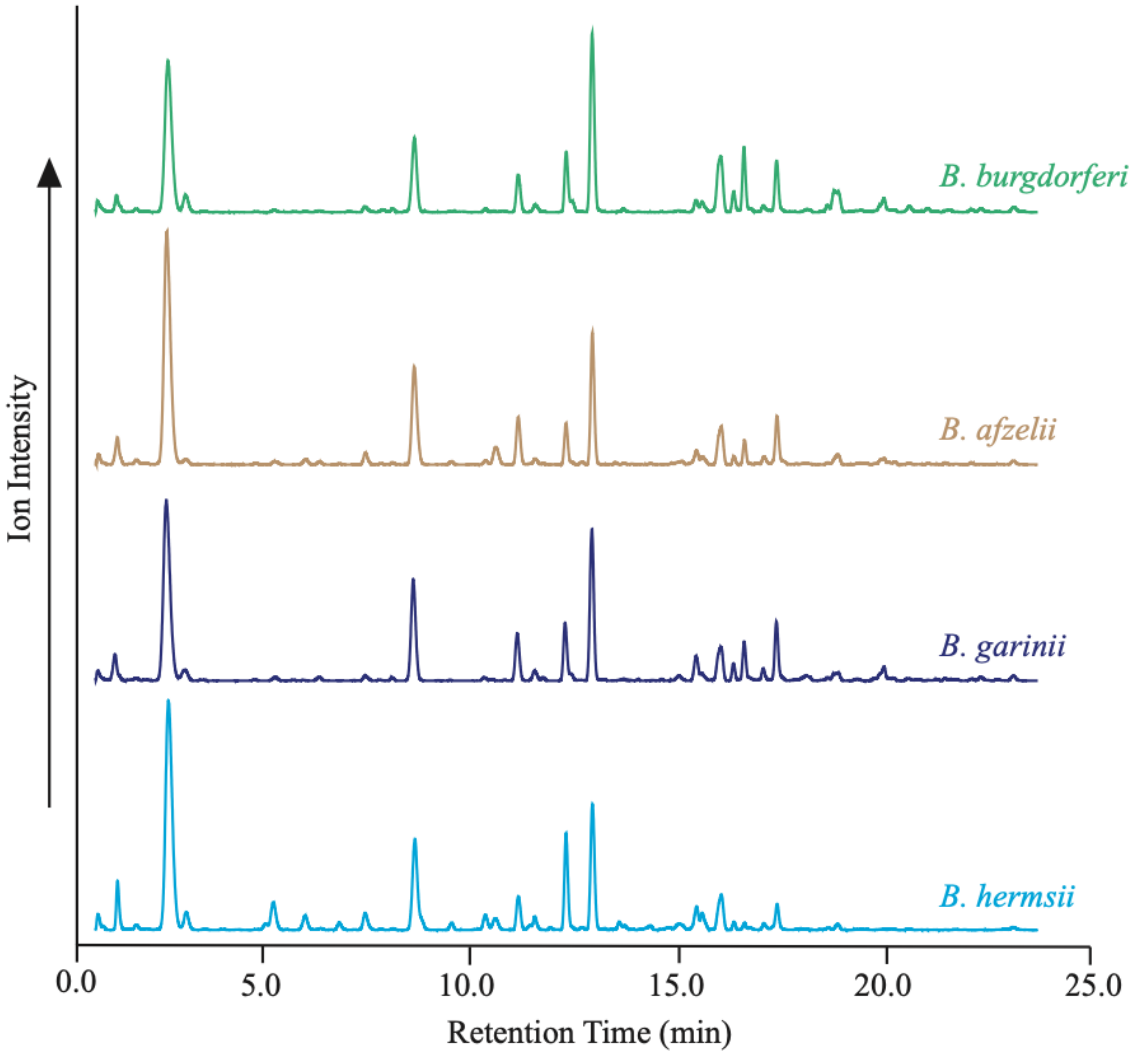

Figure 7: **PG profiles of *B. burgdorferi, B. afzelii, B. garinii,* and *B. hermsii*.** LC spectra of PG isolated from *B. burgdorferi* (green), *B. afzelii* (tan), *B. garinii* (dark blue), *and B. hermsii* (light blue). PG analyzed in each sample was purified from the same number of enumerated cells in culture.

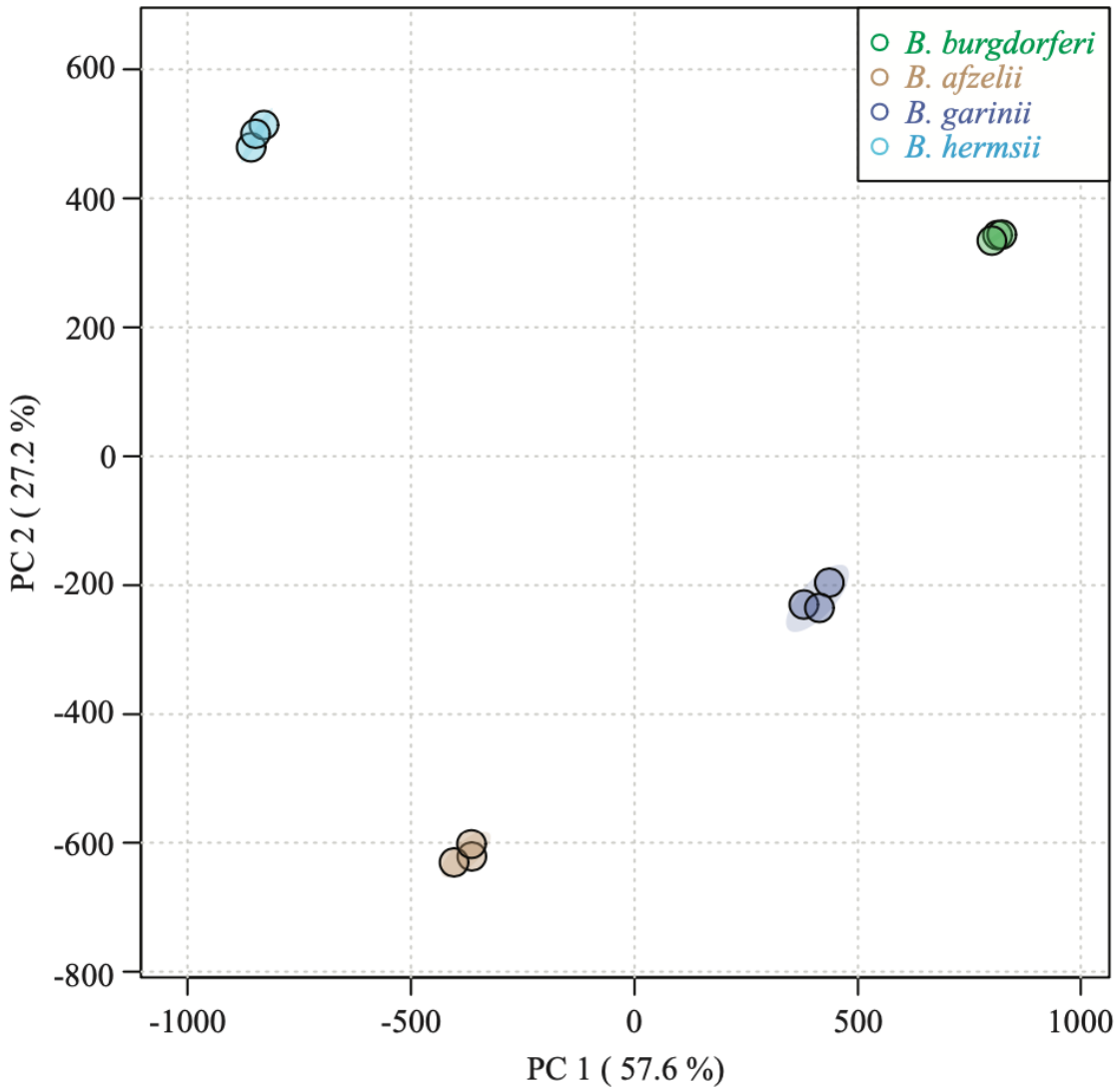

Figure 8: ***Borrelia* species can be differentiated based on their PG profiles.** Principal component analysis comparing the likeness of PG from *B. burgdorferi* (green), *B. afzelii* (tan), *B. garinii* (dark blue), and *B. hermsii* (light blue). PG analyzed in each sample was purified from the same number of enumerated cells in culture. Technical replicates were analyzed in triplicate. Data was formatted in R.

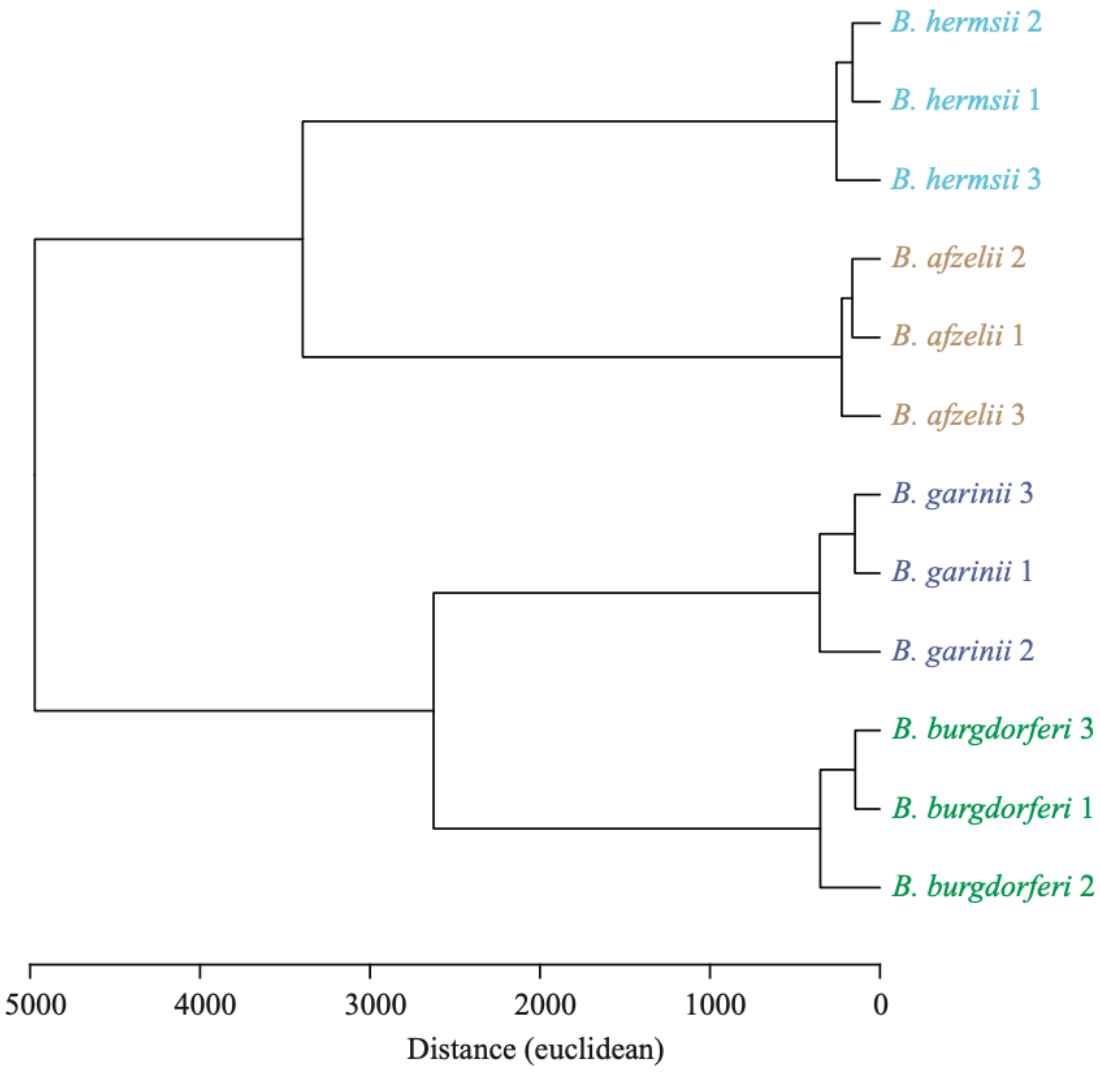

Figure 9: **Differences in *Borrelia* PG profiles transcend disease manifestation.** Hierarchical clustering of PG from *B. burgdorferi* (green), *B. afzelii* (tan), *B. garinii* (dark blue), and *B. hermsii* (light blue) shown as a dendrogram. PG analyzed in each sample was purified from the same number of enumerated cells in culture. Technical replicates were analyzed in triplicate. Data was formatted in R.

Table 1: **A comparison of PG composition between *Borrelia* species**. *Borrelia* species containing the most similar muropeptide abundancies for each muropeptide are bolded.

Muropeptide ID•	Structure	Muropeptide composition of each strain (%)			
		B. garinii	***B. burgdorferi***	***B. afzelii***	***B. hermsii***
1	MurNAc-Ala-Glu-Orn-Gly	**23.4**	**22.1**	25.2	27.9
2	GlcNAc-MurNAc-Ala-Glu-Orn-Gly	**21.6**	**19.7**	26.1	24.8
3	MurNAc-Ala-Glu-Orn-[Gly]- Ala-Gly-Orn-Glu-Ala	< 0.2	< 0.2	< 0.2	< 0.2
4	GlcNAc-MurNAc-Ala-Glu-Orn-[Gly]-Ala-Gly-Orn-Glu-Ala	< 0.2	< 0.2	< 0.2	< 0.2
5*	GlcNAc-GlcNAc-MurNAcAnh-Ala-Glu-Orn-Gly	0.6	**0.2**	**0.3**	**0.4**
6	GlcNAc-MurNAcAnh-Ala-Glu-Orn-Gly	**14.2**	11.7	**14.0**	10.3
7*	GlcNAc-GlcNAc-MurNAcAnh-Ala-Glu-Orn-[Gly]-Ala-Gly-Orn-Glu-Ala	< 0.2	< 0.2	< 0.2	< 0.2
8	GlcNAc-MurNAcAnh-Ala-Glu-Orn-[Gly]-Ala-Gly-Orn-Glu-Ala	< 0.2	< 0.2	< 0.2	< 0.2
9	MurNAc-Ala-Glu-Orn-[Gly]-Ala-Gly-Orn-Glu-Ala-MurNAc	1.4	**1.1**	0.8	**1.2**
10	GlcNAc-MurNAc-Ala-Glu-Orn-[Gly]-Ala-Gly-Orn-Glu-Ala-MurNAc	**1.6**	**1.8**	**1.7**	3.6

11	GlcNAc-MurNAc-Ala-Glu-Orn-[Gly]-Ala-Gly-Orn-Glu-Ala-MurNAc-GlcNAc	3.6	4.8	**2.7**	**2.6**
12	GlcNAc-MurNAc-Ala-Glu-Orn-[Gly]-Ala-Gly-Orn-Glu-Ala-MurNAcAnh-GlcNAc	**3.5**	4.4	**2.8**	1.9
13*	GlcNAc-GlcNAc-MurNAcAnh-Ala-Glu-Orn-[Gly]-Ala-Gly-Orn-Glu-Ala-MurNAc-GlcNAc	0.5	**0.3**	**0.3**	0.4
14	GlcNAc-MurNAcAnh-Ala-Glu-Orn-[Gly]-Ala-Gly-Orn-Glu-Ala-MurNAc	2.8	2.7	**2.1**	**1.9**
15*	GlcNAc-GlcNAc-MurNAcAnh-Ala-Glu-Orn-Gly-Ala-Orn-[Gly]-Glu-Ala-MurNAcAnh-GlcNAc	< 0.2	< 0.2	< 0.2	< 0.2
16	MurNAc-(Ala-Glu-Orn-Gly-Ala)-GlcNAc-MurNAc-(Ala-Glu-Orn-Gly-Ala)-GlcNAc-MurNAcAnh-(Ala-Glu-Orn-Gly)	< 0.2	< 0.2	< 0.2	< 0.2
17	GlcNAc-MurNAcAnh-Ala-Glu-Orn-[Gly]-Ala-Gly-Orn-Glu-Ala-MurNAcAnh-GlcNAc	< 0.2	< 0.2	< 0.2	< 0.2
Total % Identified°		73.2	69.0	76.0	75.0
% G-G-anhM		1.1	0.5	0.6	0.8

•Muropeptide IDs refer to previous identification in Chapter III. Supplemental figures for each muropeptide can be found in the Appendix (Fig. S3-S32).

*Muropeptide contains G-G-anhM

°The total % of PG identified in each strain does not take into account any muropeptide species listed as < 0.2%; rather, it reports the minimum amount of muropeptide composition confidently identified.

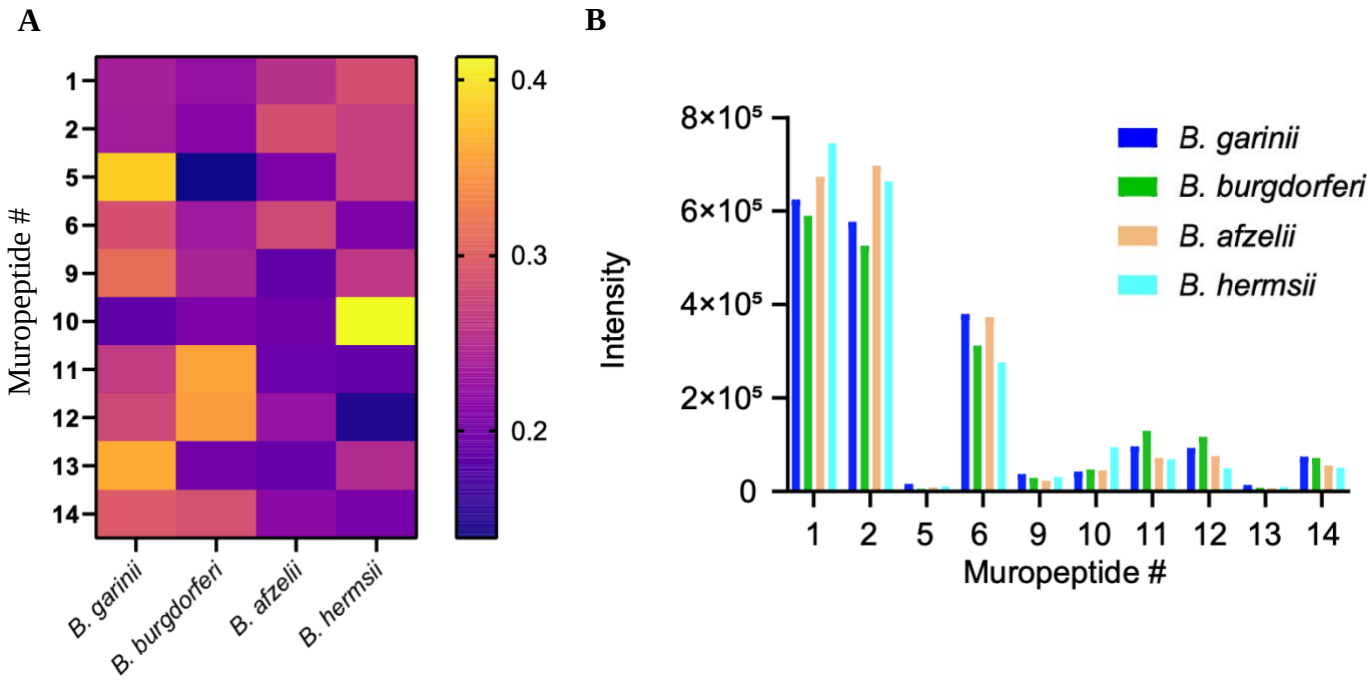

Figure 10: ***Borrelia* species incorporate conserved muropeptides in different abundances. A)** Differences in muropeptide abundance between *B. garinii*, *B. burgdorferi*, *B. afzelii*, and *B. hermsii* displayed as a heat map. Muropeptide relative abundance was normalized by row, by the total amount of that muropeptide present in each *Borrelia* species combined, for each individual muropeptide. **B)** The intensity of each muropeptide, for each *Borrelia* species, was normalized to the sample with the least total PG present (*B. burgdorferi* sample 3). **A & B)** Only muropeptides constituting > 0.2% of total PG in each species are shown. Data represents the average of technical triplicates and was formatted in GraphPad Prism 9.0.

Chapter V

Cellular and molecular characterization of a putative peptidoglycan synthesis enzyme in *Borrelia burgdorferi*, the Lyme disease spirochete

Introduction

The vast majority of bacteria require the cell wall biopolymer peptidoglycan (PG) to survive. PG is composed of glycan strands of alternating *N*-acetylglucosamine (Glc*N*Ac) and *N*-acetylmuramic acid (Mur*N*Ac) crosslinked by peptide chains of L- and D- amino acids and diamines. While PG composition is known to vary between bacterial species, its overall functions are highly conserved. In nearly all bacteria that incorporate PG it plays a role in 1) cell strength and morphology, 2) cell elongation and division, 3) serving as an antibiotic target, and 4) host immune detection and modulation[28]. Given the importance of PG's roles in the cell, many bacteria have an array of enzymes dedicated to the synthesis and maintenance of PG.

PG synthesis begins in the cytoplasm where the Mur enzyme pathway (MurA-MurF) catalyzes the conversion of uridine diphosphate (UDP)-Glc*N*Ac into UDP-Mur*N*Ac followed by five subsequent amino acids additions to generate UDP-Mur*N*Ac-pentapeptide[51]. UDP-Mur*N*Ac-pentapeptide is then attached to the cytosolic membrane through the enzyme MraY, creating Lipid I[117]. The addition a UDP-Glc*N*Ac molecule to Lipid I, through the enzyme MurG, results in Lipid II — the disaccharide-pentapeptide precursor of PG[118]. Finally MurJ, a "flippase" enzyme, "flips" the disaccharide-pentapeptide across the cytoplasmic membrane where Penicillin-Binding Proteins (PBPs) utilize Lipid II in the synthesis of PG[119].

PBPs are essential PG-synthesis enzymes bound to the exterior of the cytosolic membrane in bacteria that incorporate PG[51]. These essential PG synthesis enzymes are divided into classes based on their molecular weight — high vs low molecular weight PBPs — and subdivided by their

type of function. Type A PBPs possess transglycosylase and transpeptidase activity, both polymerizing the extension of glycan strands and crosslinking peptide chains in PG. Additionally, these PBPs play a large role in the overall maintenance of the bacterial cell wall — working to upkeep cell wall integrity by repairing defects[120]. Type B PBPs are monofunctional transpeptidases but have a much higher affinity for the D-Ala-D-Ala moieties on peptide stems. This affinity aids in crosslinking, as Type B PBPs are typically associated with protein complexes involved in cellular elongation and division[52]. Due to their importance in PG synthesis and maintenance, inhibition of PBPs can be detrimental, and often lethal, to a cell. The vital nature of PBPs as essential PG synthesis enzymes makes them a lucrative drug target.

As their name suggests, PBPs are the target of β-lactam antibiotics. These antibiotics structurally resemble the D-Ala-D-Ala moiety bound by the PBP's transpeptidase domain during peptide chain crosslinking[121]. If bound, β-lactam antibiotics form a covalent linkage to the PBP's transpeptidase domain, permanently inhibiting the enzyme's function[122]. This inhibition proves lethal for many bacteria; however, some have evolved mechanisms to elude or disable β-lactam antibiotics. The most widely known example of β-lactam resistance is Methicillin Resistant *Staphylococcus aureus* (MRSA) and its PBP2a — capable of tolerating β-lactam antibiotics and compensating for the inhibition of other PBPs[56]. However, other bacteria have evolved separate, and increasingly medically relevant, mechanisms for dealing with β-lactam treatment. For example, some bacteria secrete β-lactamases — enzymes capable of degrading β-lactam antibiotics in the environment, effectively safeguarding their PBPs from inhibition[123]. Regardless of the method employed, resistance to β-lactam antibiotics is a current, and growing, issue in the medical world.

The work in this chapter addresses a crucial knowledge gap in the treatment of Lyme disease and biology of *Borrelia burgdorferi*. While much is known about PBPs in model organisms such as *Escherichia coli*, boasting 12 characterized PBPs[124], and MRSA wielding its PBP2a[56], virtually nothing is known about the function of PBPs in *B. burgdorferi*. Although β-lactam antibiotics are the most common treatment for *B. burgdorferi* infection, we lack a mechanistic understanding of how or why they work. Addressing this void of knowledge about these potentially essential PG synthesis enzymes in *B. burgdorferi* may lead to the discovery and development of novel Lyme disease treatments.

Results

BB0718 shares sequence, structure, and transpeptidase motif identity with known PBPs

A putative PBP2a gene homologue, *bb0718*, was identified in *B. burgdorferi*. Upon a sequence alignment comparison using RCSB Protein Data Bank this gene, encoding for the *B. burgdorferi* protein BB0718, was found to share sequence identity with many known and characterized bacterial PBPs. A similar match was found to be PBP2 in *Helicobacter pylori* — upwards of 30% of the two sequences were identical and an additional 46% of the sequences shared amino acid similarity. BB0718's amino acid sequence was then aligned with the characterized amino acid sequence of PBP2 from *H. pylori* (courtesy of Dr. Anne Brown, Virginia Tech). When superimposed upon PBP2 from *H. pylori*, both appeared structurally similar (Fig. 11). In addition, three highly conserved PBP transpeptidase motifs were observed in BB0718: SxxK, SxN, and KTG. Shown in magenta, these transpeptidase motifs overlap with those found in *H. pylori's* PBP2, suggesting that BB0718 may possess transpeptidase activity (Fig. 11).

Expression of *bb0718* in *E. coli* has adverse effects on cell growth

To better understand BB0718's role in the cell, *E. coli* — a model organism for both cell biology and PBP function — was chosen as a surrogate host for our studies. We created two strains of LOBSTR *E. coli*, one containing *bb0718* and one without (Methods, page 20), as a control — LOBSTR/pET200::*bb0718* and LOBSTR/pET200::empty *E. coli*, respectively.

Expression of *bb0718* in LOBSTR/pET200::*bb0718 E. coli* was accomplished through induction with isopropyl β-d-1-thiogalactopyranoside (IPTG). Induction conditions were optimized in an attempt to maximize protein expression without becoming too detrimental to the cell (Fig. 12). It was found that expression of *bb0718* in LOBSTR/pET200::*bb0718 E. coli* was inversely related to viability; higher induction concentrations resulted in less cell growth (Fig. 12). Conversely, induction of the LOBSTR/pET200::empty *E. coli* with IPTG showed no differences in growth regardless of concentration. To ensure the observed differences were a result of *bb0718* expression, and that BB0718 was being produced by LOBSTR/pET200::$bb0718^{Bb}$ *E. coli*, protein purification was performed.

BB0718 elutes as a protein doublet — a trait common in PBPs

LOBSTR/pET200::*bb0718* and LOBSTR/pET200::empty *E. coli* were cultured and induced as described in the methods (Methods, pages 21-23). Samples were taken pre- and post-induction with IPTG, post-affinity-chromatography isolation, and post-dialysis to assess BB0718 abundance and the overall effectiveness of our techniques. Samples were analyzed via Coomassie stain on a polyacrylamide gel (Fig. 13). BB0718 (MW 64,413 in native system) is absent pre-induction, but apparent post-induction with IPTG. Additionally, background was almost entirely removed after affinity-chromatography isolation and subsequent dialysis, suggesting BB0718 is

purifying to a reasonable extent (Fig. 13). In samples where BB0718 was produced, protein doublets are visible at BB0718's anticipated MW of ~65,500 (including N-terminal His-tag). The occurrence of these doublets, which are common for PBP migration in a polyacrylamide gel[125], reinforces the hypothesis that our protein, BB0718, is in fact, a PBP.

E. coli cells expressing *bb0718* are less tolerant to osmotic and enzymatic stress

If BB0718 is a PBP, we expected its expression in a non-native system would result in compromises in cell wall integrity. To test this hypothesis, LOBSTR/pET200::*bb0718 E. coli* with and without IPTG induction, were subjugated to various concentrations of lysozyme and dilutions of cell concentration in water (Fig. 14). These incubations represented enzymatic and osmotic stress conditions, respectively. LOBSTR/pET200::*bb0718 E. coli* induced with IPTG were found to be significantly more susceptible to both lysozyme and osmotic pressure relative to their non-induced counterparts. This notable decrease in enzymatic and osmotic stress tolerance suggested that BB0718 was affecting the integrity of *E. coli's* cell wall.

Production of *B. burgdorferi's* putative PBP2a in *E. coli* results in an inability to regulate growth and division

After observing the production of, and adverse effects resulting from, BB0718 in LOBSTR/pET200::*bb0718 E. coli*, we sought to characterize its morphological phenotype. Under phase contrast microscopy, LOBSTR/pET200::*bb0718 E. coli* appeared to have two distinct morphologies. The first morphology was drastically and abnormally elongated cells (Fig. 15b). The second represented *E. coli* that were slightly longer than average but possessed noticeable cell wall perturbations (Fig. 15b). The LOBSTR/pET200::empty *E. coli* control strain possessed no

defects when induced with IPTG at the same concentration as the LOBSTR/*bb0718 E. coli* (Fig. 15a). To quantitatively analyze the morphological differences of *bb0718* expression in *E. coli*, a cell-length distribution analysis was performed. LOBSTR/pET200::*bb0718 E. coli* were found to have an average cell-length of over 10 μm — nearly 4 times longer than the average wild type *E. coli* (Fig. 15c). However, nearly 2% of LOBSTR/*bb0718 E. coli* were found to exceed 100 μm in length. This noticeable perturbation and drastic elongation suggest BB0718 may be impacting *E. coli's* ability to grow and divide. Conversely, LOBSTR/empty *E. coli* showed only minor deviation in phenotype, with an average length approaching 3 μm, hardly longer than the average wild type *E. coli*[126]. Given BB0718's apparent involvement with elongation and division, we investigated localization of its activity.

BB0718 appears to act on the PG elongasome and divisome in *E. coli*

To assess the localization of BB0718 in *E. coli*, a DH5α/BSV2::mCherry-*bb0718* fluorescent fusion was created (Methods, page 20). Upon live-cell epifluorescent microscopy, we observed two distinct localization patterns of BB0718 in *E. coli* (Fig. 16). The first, and more common, was homologous expression throughout the cell cylinder — suggesting an even distribution of BB0718 activity. The second, less common pattern, was a punctate localization to mid-cell or the poles. This is interesting, given as *E. coli* grow, their PG is synthesized throughout their cell cylinder, before division occurs at mid-cell[29]. Collectively, these phenotypes of homologous expression and punctate localization appear to represent BB0718's involvement with PG elongation and division, respectively.

BB0718 binds to penicillin and other β-lactams derivatives

With BB0718 possessing a multitude of PBP-like functions, our attention shifted to testing its affinity for β-lactam antibiotics. BB0718 was isolated from LOBSTR/pET200::*bb0718* as described (Methods, pages 21-23) and was found to bind bocillin, a fluorescent derivative of penicillin (data not shown). To gauge the affinity of this interaction, a competitive inhibition assay was performed between bocillin and various concentrations of penicillin G (Fig. 17). Doublets were observed in all lanes barring the negative control. As penicillin G concentration increased, the doublet's intensity decreased, verifying that BB0718 bound penicillin G and bocillin in a competitive manner. In a separate experiment, the affinity of multiple β-lactam and cephalosporin antibiotics for BB0718 was tested (Fig. 18). Here, we observed that aztreonam possessed the highest overall affinity, as indicated by the lowest fluorescence of bocillin-bound BB0718. While these data serve as an indication that BB0718 has penicillin-binding capabilities, further research, and higher protein concentrations, will be needed assess our findings in more detail.

Discussion & Future Plans

BB0718 has many notable hallmarks of a typical PBP: presentation as a doublet in size-exclusion chromatography (Fig. 13), localization to sites of PG elongation and division in *E. coli* (Fig. 16), and its ability to bind β-lactam antibiotics (Figs. 17 & 18). However, there are multiple studies and adaptations we plan to perform to finalize its characterization as a PBP. A major inhibition to our work was the amount of BB0718 that could be isolated from any given sample. Natively from *B. burgdorferi*, BB0718's apparent function in *E. coli* proved highly toxic. As a result, protein yields were exceedingly low — sub microgram amounts were obtained from

multiple liters of culture combined. This scarcity prohibited us from performing a variety of experiments to crystallize, and further assess the capabilities of, BB0718.

To compensate for this lack of protein production, work has begun on transforming pET200::*bb0718* into "Vmax Express" cells. "Vmax Express" is a novel bacterial strain of bioengineered *Vibrio natriegens* developed specifically for protein expression[127]. Due to their significantly higher protein yields and faster doubling times compared to *E. coli* expression systems, we expect the Vmax cell line to produce superior quantities of BB0718, allowing for more in-depth studies.

Preliminary results suggest BB0718 may possess transpeptidase activity in *E. coli* (data not shown). Utilization of Vmax cells as an enhanced expression system will allow for the validation of this observation. PG isolated from Vmax cells expressing, and not expressing, BB0718 will be compared through LCMS. Differences in LC spectra of PG from each sample will be indicative of transpeptidase function. MS analysis will allow for the determination of the exact bonds being cleaved.

Among the first studies we will perform with BB0718 isolated from the Vmax cell line will be further characterization of BB0718's transpeptidase activity. Nucleotide primers have been designed, capable of inducing site-directed mutagenesis on the serines and threonine of BB0718's three highly conserved transpeptidase motifs: SxxK, SxN, and KTG. The mutagenesis will replace the aforementioned serines and threonine with alanine. If these highly conserved PBP motifs are conferring the observed transpeptidase activity, we expect function to be abolished upon conversion to alanine. To further assess the function of this enzyme, BB0718 and *B. burgdorferi* PG co-incubation assays will be performed. By co-incubating this putative PBP and PG from its native organism, we will be able to assess differences in muropeptide profile before and after

incubation. LCMS analysis of these samples will provide insights into BB0718's function in *B. burgdorferi* — any transpeptidase or transglycosylase activity will be apparent. Finally, crystallization of BB0718 will allow for a molecular, and stereochemical, analysis of the protein and its active sites. Once the function of BB0718 in *B. burgdorferi* has been elucidated, high-throughput antibiotic screens can be adapted and performed to test the affinity of various β-lactam derivative antibiotics.

Further studies of BB0718 will broaden our understanding of PG synthesis and antibiotic resistance/susceptibility in *B. burgdorferi*. Characterization of BB0718 will resolve molecular structure/function relationship(s) and lead to novel therapies in the treatment of Lyme disease.

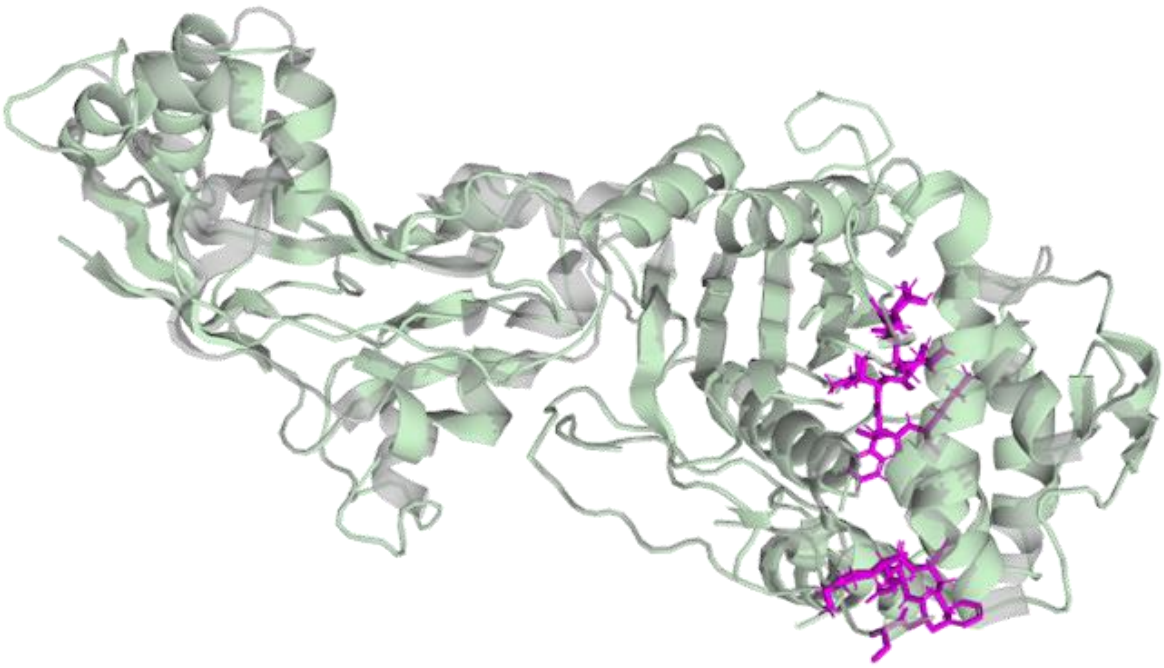

Figure 11: The predicted structure of BB0718. *B.* burgdorferi's BB0718 (green), based on amino acid sequence, superimposed on the crystal structure of PBP2 from *H. pylori* (gray). Highly conserved PBP transpeptidase motifs SxxK, SxN, and KTG are shown in magenta.

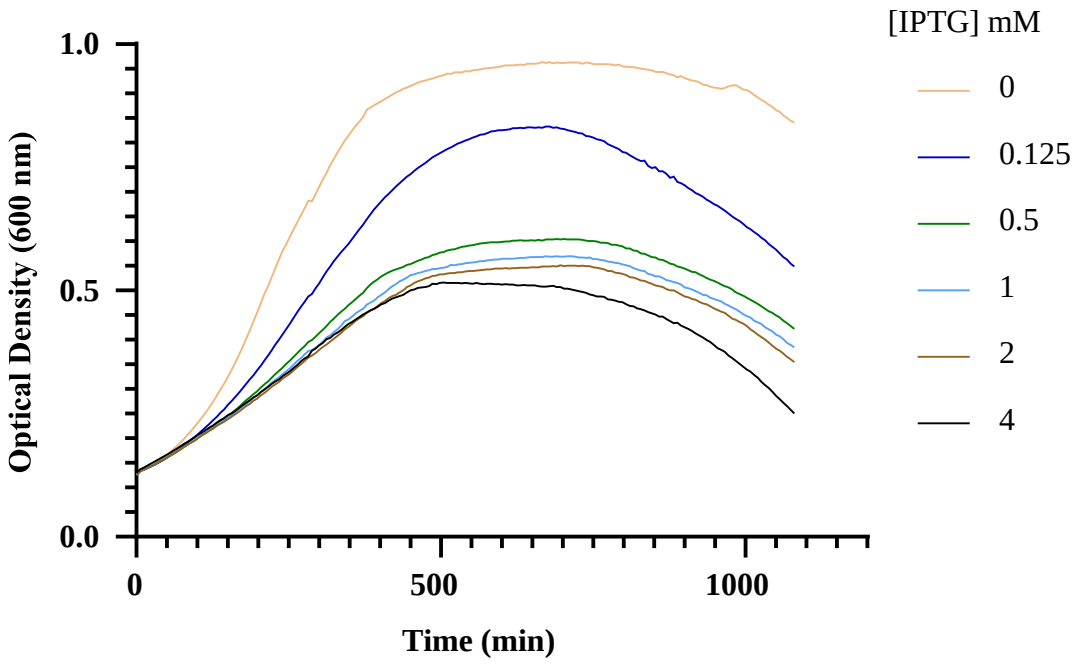

Figure 12: **Induction of *bb0718* has adverse effects on *E.* coli growth.** Growth curves of LOBSTR/pET200::*bb0718 E. coli* cells. Samples were induced with various concentrations of IPTG and optical density was monitored for a total of 18 hours post induction.

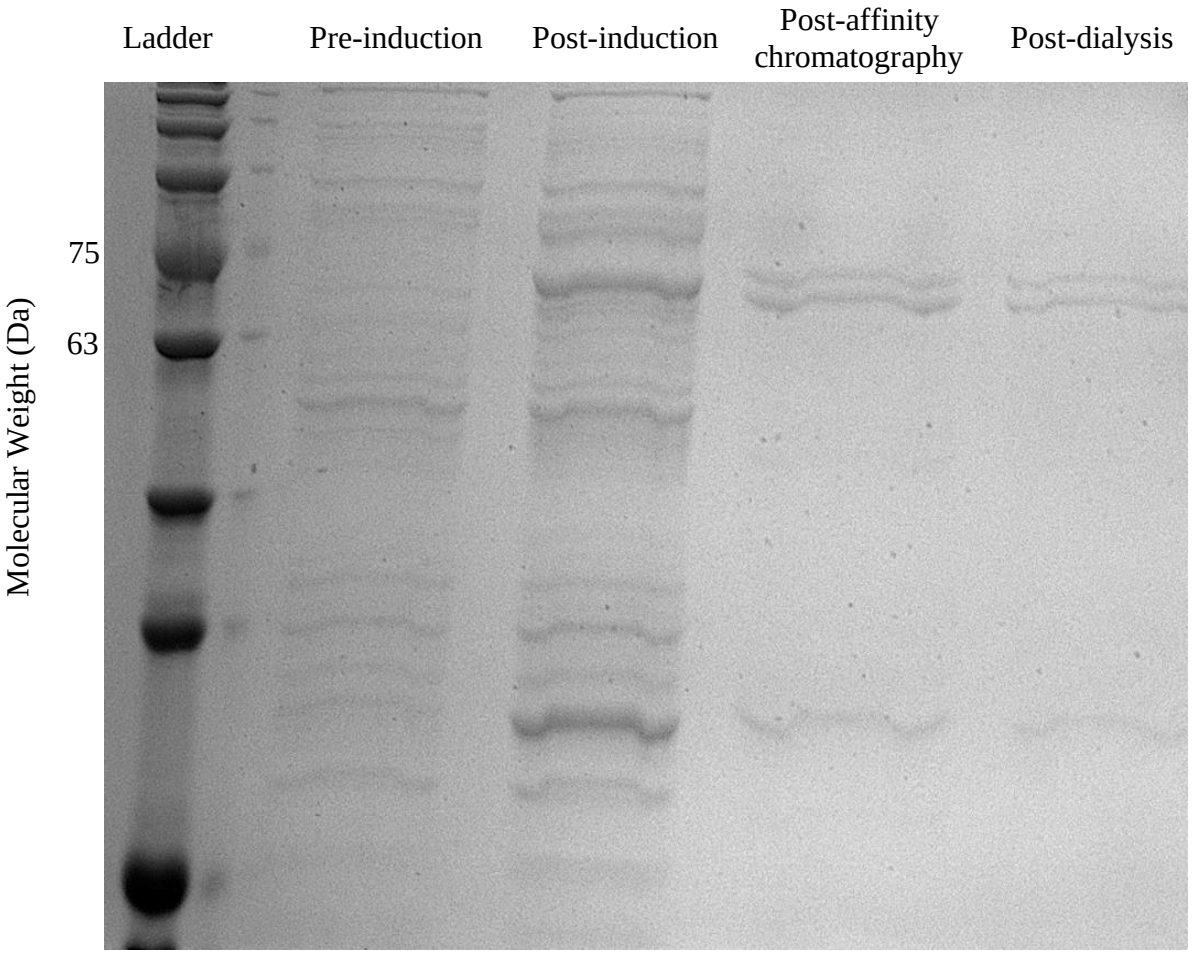

Figure 13: BB0718 elutes as a doublet in SDS-PAGE. Cell lysate samples isolated from LOBSTR/pET200::*bb0718 E. coli* cells. Samples were isolated pre-IPTG induction, post-IPTG induction, post-affinity chromatography induction with Ni beads, and post-dialysis with semipermeable membrane. SDS-PAGE gel electrophoresis was performed for 1 hour and protein bands were visualized with Coomassie blue. The expected molecular weight for BB0718 is ~65,500 Da, including N-terminal His-tag. Images were obtained using a G:Box imaging system (Syngene).

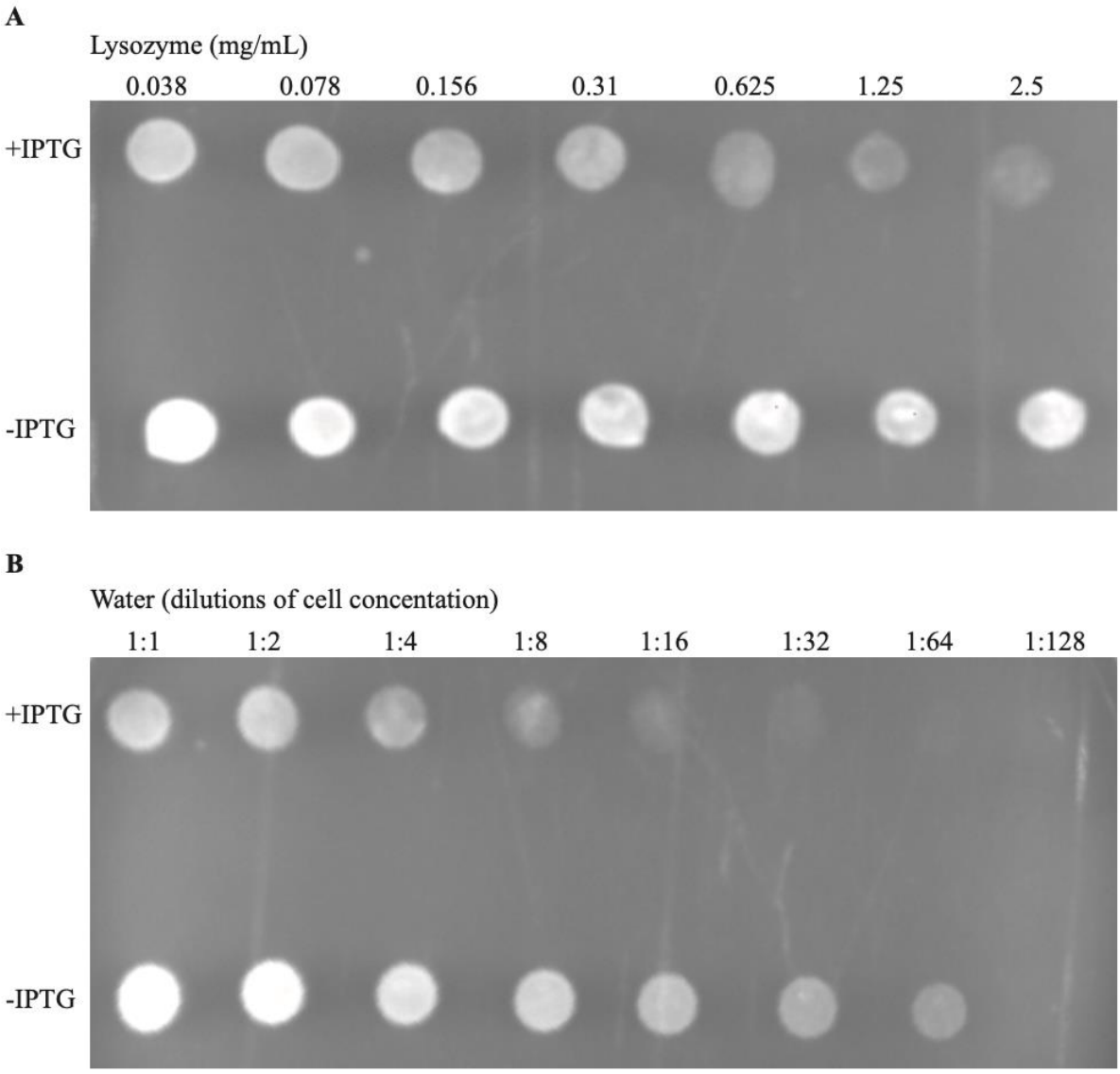

Figure 14: *E. coli* expressing *bb0718* are significantly more susceptible to enzymatic and osmotic stress. A) LOBSTR/pET200::*bb0718 E. coli* cells stressed with increasing concentrations of lysozyme, with and without IPTG induction. **B)** LOBSTR/pET200::*bb0718 E. coli* cells stressed with increasing osmotic pressure from diluting cell concentration, with and without IPTG induction. **A & B)** After incubation with corresponding stressor, 20 µL of cell suspension was spotted on an LB agar plate and allowed to incubate at 37°C for 24 h. Imaging was performed with a G:Box imaging system (Syngene).

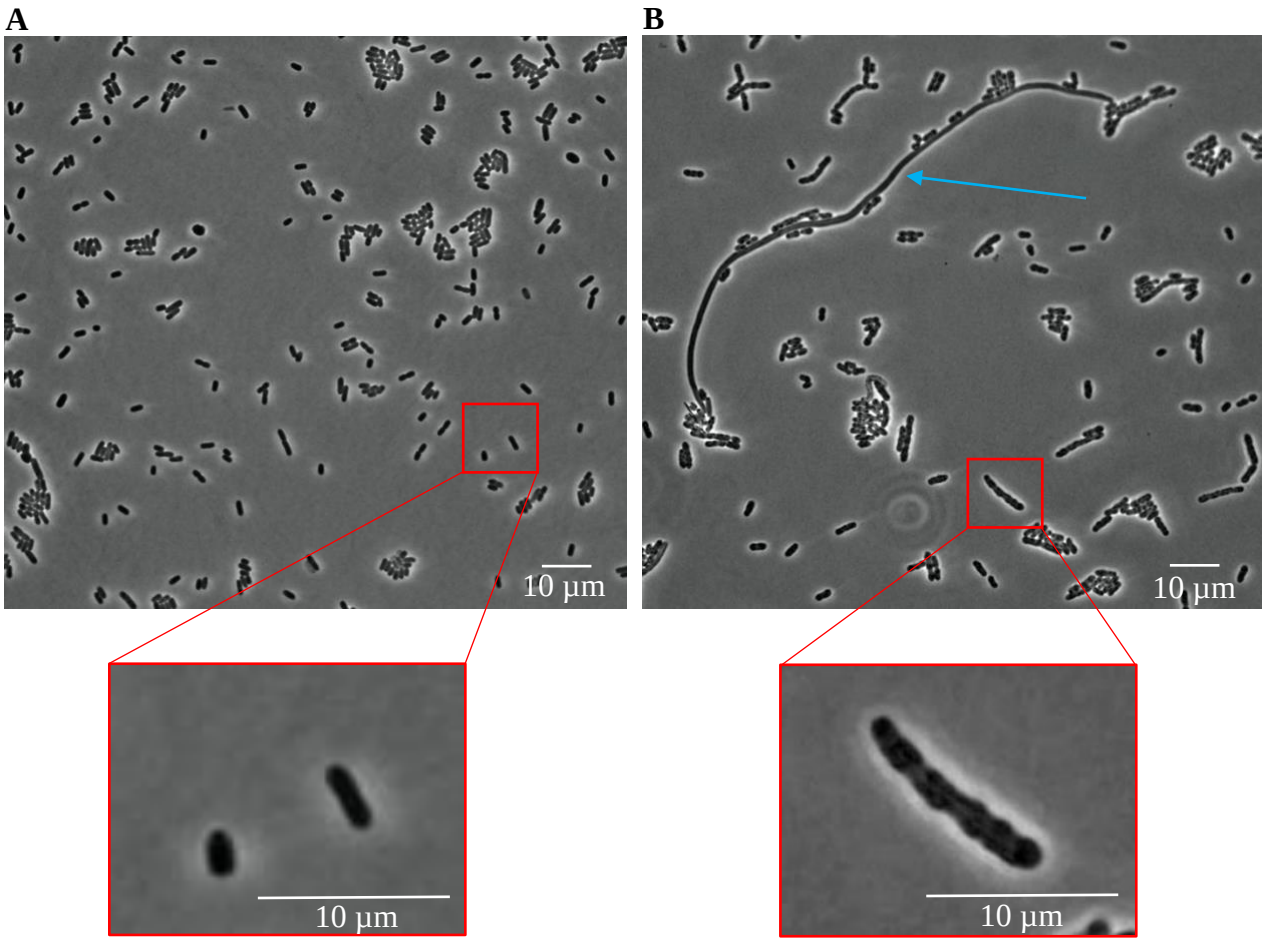
A
B
10 µm
10 µm
10 µm
10 µm

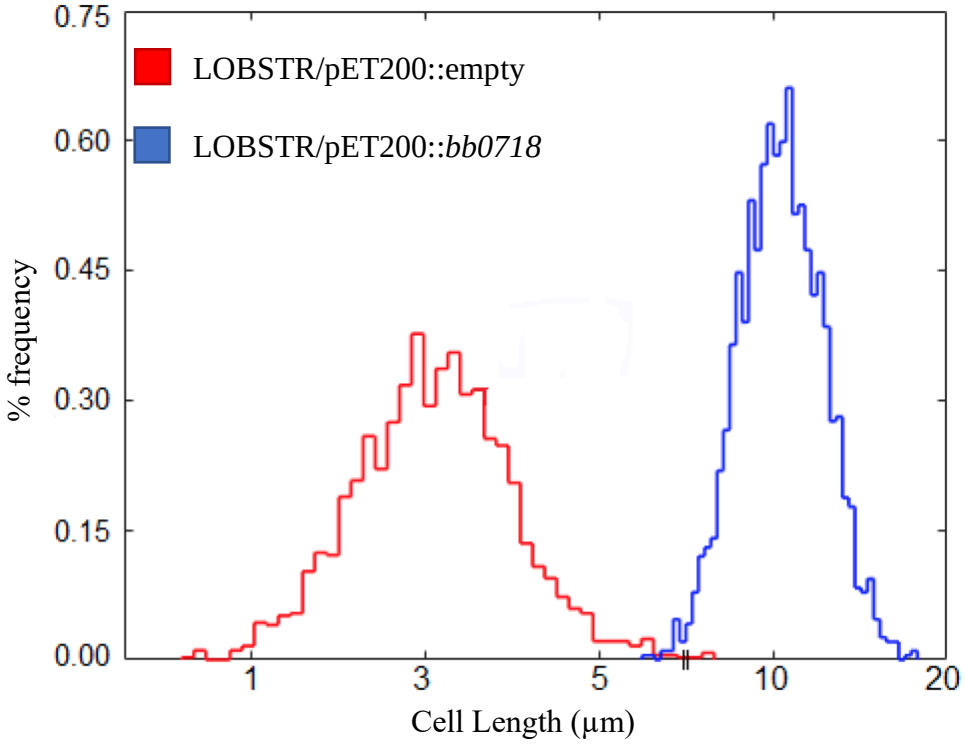
C
0.75
0.60
0.45
0.30
0.15
0.00
% frequency
LOBSTR/pET200::empty
LOBSTR/pET200::bb0718
1
3
5
10
20
Cell Length (µm)

Figure 15: A morphological analysis of *E. coli* producing BB0718. Phase microscopy of **A)** and **B)**. **A)** LOBSTR/pET200::empty *E. coli* induced with 1 mM IPTG. Inset image depicts morphology of a single cell. **B)** LOBSTR/pET200::*bb0718 E. coli* induced with 1 mM IPTG. Inset image depicts the morphology of a single cell. The cyan arrow indicates an *E. coli* cell that exceeds 100 µm in length. **C)** Cell length distribution histogram of LOBSTR/pET200::empty and LOBSTR/pET200::*bb0718 E. coli* in red and blue, respectively. For both samples, n = 1000.

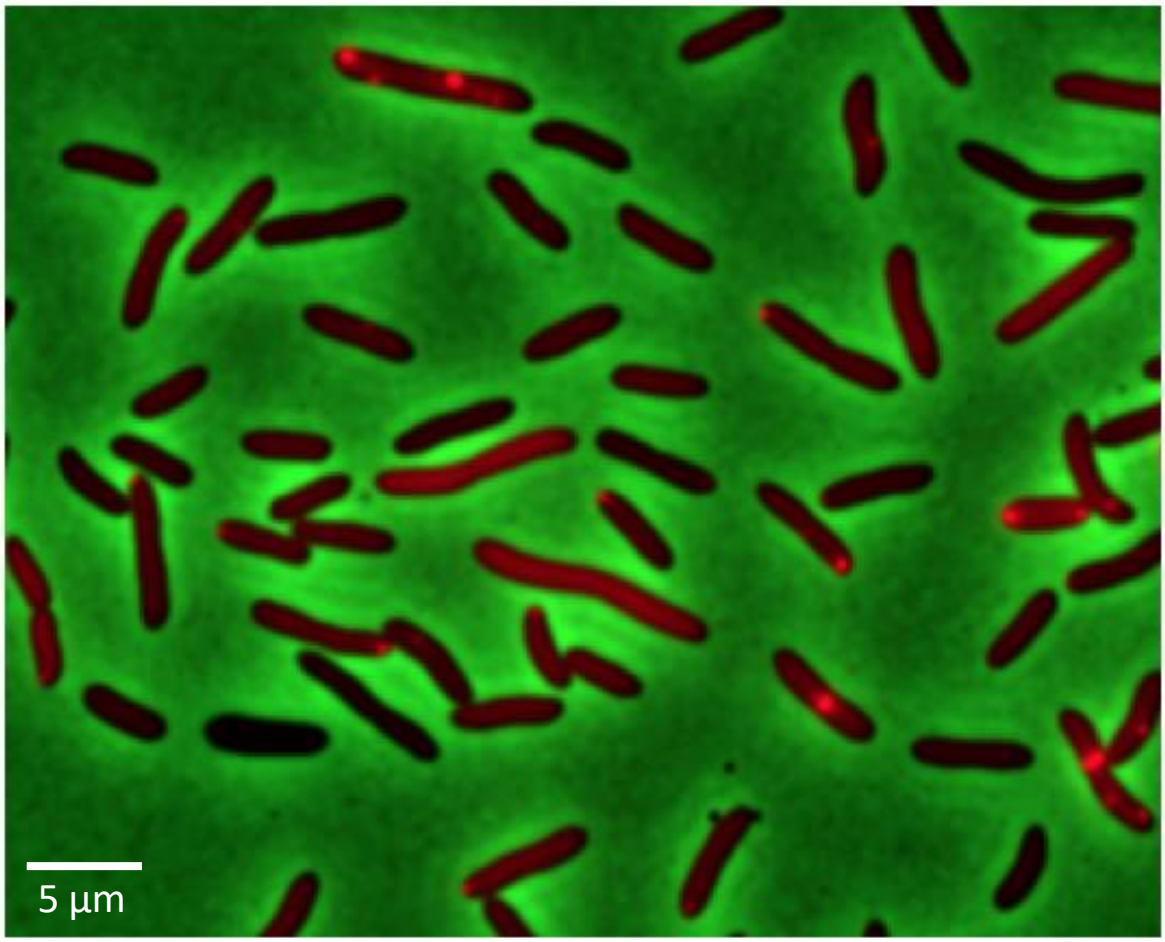

Figure 16: BB0718 has bipartite distribution in *E. coli*. Epifluorescent microscopy of DH5α/BSV2::mCherry-*bb0718* with native BB0718 promotor. The micrograph shown is a merge of phase contrast signal (green) and epifluorescence signal of fusion protein mCherry-BB0718 (red).

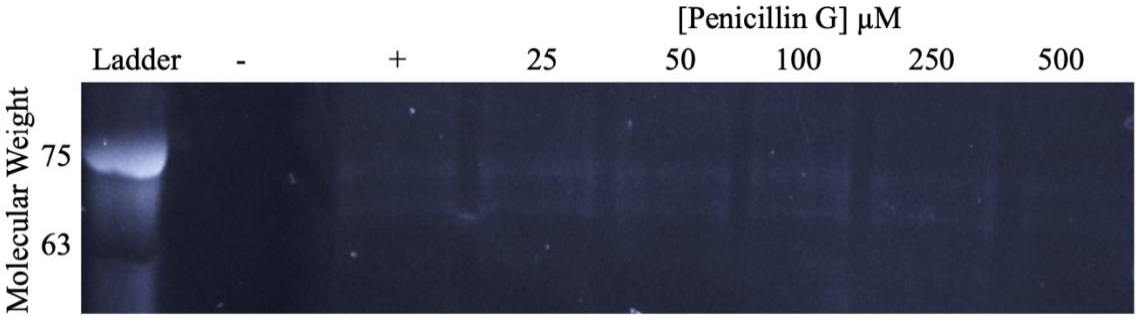

Figure 17: **Competitive binding of BB0718 between Bocillin and Penicillin G.** The negative control is BB0718 incubated with PBS. The positive control is BB0718 incubated with Bocillin. Each well after the positive control contains BB0718, Bocillin, and the listed concentration of Penicillin G.

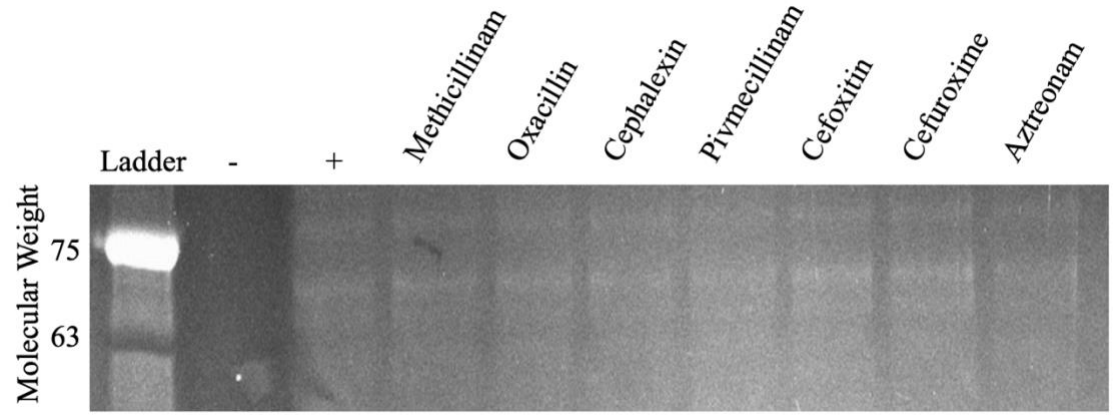

Figure 18: β-lactam and cephalosporin antibiotic affinity assay of BB0718. The negative control is BB0718 incubated in PBS. The positive control is BB0718 incubated with Bocillin. Each lane following the positive control contains BB0718, Bocillin, and the antibiotic listed.

Chapter VI

Summary

The findings presented in this thesis provide a characterization of peptidoglycan and the enzymes that synthesize it in *Borrelia burgdorferi*, while laying the foundations for similar studies throughout the genus of *Borrelia*. We have shown that glycan strands in *B. burgdorferi* peptidoglycan deviate from the previously established paradigm through incorporation of Glc*N*Ac-Glc*N*Ac — a structural subunit from their chitinous tick vector. Utilization of Glc*N*Ac-Glc*N*Ac likely evolved as a means to survive the sometimes nutrient-deficient tick midgut and its incorporation into the peptidoglycan serves to compensate for self-inflicted torsional stress. This novel inclusion affords flexibility, motility, and enzymatic and osmotic stress-tolerance to *B. burgdorferi* while enhancing its morphology. Muropeptide characterization identified ~80% of total muropeptides in *B. burgdorferi* peptidoglycan. Glc*N*Ac-Glc*N*Ac was found to exclusively occur at the glycan termini, anhMur*N*Ac — the site of novel muropeptide incorporation during elongation. Glc*N*Ac-Glc*N*Ac's localization to the glycan termini suggests a novel mechanism to spatially and temporally regulate Glc*N*Ac-Glc*N*Ac-anhMur*N*Ac inclusion and that Glc*N*Ac-Glc*N*Ac-anhMur*N*Ac may impact the pathogenicity of released muropeptides.

These findings paved the way for the characterization of peptidoglycan composition in other pathogenic *Borrelia* species. Two other Lyme disease spirochetes, *Borrelia afzelii* and *Borrelia garinii*, as well as a relapsing fever spirochete, *Borrelia hermsii*, were found to incorporate appreciable amounts of Glc*N*Ac-Glc*N*Ac-anhMur*N*Ac into their peptidoglycan. The conserved nature of this inclusion suggests it may be an evolutionary adaptation to life inside a tick predating the differentiation of Lyme disease and relapsing fever *Borrelia*. Additionally,

Glc*N*Ac-Glc*N*Ac-anhMur*N*Ac may be an evolutionary adaptation to withstanding self-inflicted torsional stress from periplasmic flagella conserved within the phylum Spirochaetes.

Finally, our studies provided the partial characterization of a putative *B. burgdorferi* peptidoglycan synthesis enzyme in *Escherichia coli*. *B. burgdorferi* protein BB0718 was found to have many hallmarks of penicillin-binding protein activity: elution as a doublet in size-exclusion chromatography, localization to, and activity at, sites of peptidoglycan elongation and division in *E. coli*, and affinity for β-lactam antibiotics. Preliminary data suggests BB0718 harbors transpeptidase motifs that are highly conserved in other bacterial penicillin-binding proteins, and that BB0718 may function as a transpeptidase in *E. coli*.

Through our efforts we are left with a greater understanding of peptidoglycan and the enzymes that synthesize it, in *B. burgdorferi*, and insights into the peptidoglycan profile of other pathogenic *Borrelia*. Continued studies will, 1) further elucidate the importance of Glc*N*Ac-Glc*N*Ac-anhMur*N*Ac and its implications for peptidoglycan structure, function, and pathogenesis throughout *Borrelia*. 2) Assess if Glc*N*Ac-Glc*N*Ac-anhMur*N*Ac is an evolutionary adaptation that predates the differentiation of Lyme disease and relapsing fever *Borrelia* as well as their arthropod vectors — soft and hard-bodied ticks and the human body louse. Or, if Glc*N*Ac-Glc*N*Ac-anhMur*N*Ac is an evolutionary adaptation within the phylum Spirochaetes to withstand the self-inflicted torsional stress of periplasmic flagella. And, 3) characterize structure/function relationship(s) of *B. burgdorferi's* putative penicillin-binding protein, BB0718, and discover novel therapies in the treatment of Lyme disease.

References:

1 Kugeler, K. J., Schwartz, A. M., Delorey, M. J., Mead, P. S. & Hinckley, A. F. Estimating the Frequency of Lyme Disease Diagnoses, United States, 2010-2018. *Emerg Infect Dis* **27**, 616-619, doi:10.3201/eid2702.202731 (2021).

2 CDC. *Lyme Disease: Recent Surveillance Data - Centers for Disease Control and Prevention*, <https://www.cdc.gov/lyme/datasurveillance/index.html> (2019).

3 Mead, P. S. Epidemiology of Lyme Disease. *Infectious Disease Clinics of North America* **29**, 187-210 (2015).

4 Donohoe, H., Pennington-Gray, L. & Omodior, O. Lyme disease: Current issues, implications, and recommendations for tourism management. *Tour Manag* **46**, 408-418, doi:10.1016/j.tourman.2014.07.006 (2015).

5 Eisen, R. J. & Eisen, L. The Blacklegged Tick, Ixodes scapularis: An Increasing Public Health Concern. *Trends Parasitol* **34**, 295-309, doi:10.1016/j.pt.2017.12.006 (2018).

6 Steere, A. C., Malawista, S. E., Snydman, D. R., Shope, R. E., Andiman, W. A., Ross, M. R. & Steele, F. M. Lyme Arthritis — an Epidemic of Oligoarticular Arthritis in Children and Adults in Three Connecticut Communities *Arthritis & Rheutology* (1977).

7 Steere, A. C., Broderick, T. F. & Malawista, S. E. Erythema Chronicum Migrans and Lyme Arthritis: Epidemiologic Evidence for a Tick Vector *American Journal of Epidemiology* **108** (1978).

8 Burgdorfer, W., Barbour, A. G., Hayes, S. F., Benach, J. L., Grunwaldt, E. & Davis, J. P. Lyme disease-a tick-borne spirochetosis? *Science* (1982).

9 Tilly, K., Rosa, P. A. & Stewart, P. E. Biology of Infection with Borrelia burgdorferi. *Infectious Disease Clinics of North America* (2008).

10 Donahue, J. G., Piesman, J. & Spielman, A. Reservoir Competence of White-Footed Mice for Lyme Disease Spirochetes. *The American Journal of Tropical Medicine and Hygiene* **36** (1987).

11 Rollend, L., Fish, D. & Childs, J. E. Transovarial transmission of Borrelia spirochetes by Ixodes scapularis: A summary of the literature and recent observations. *Ticks Tick-Borne Diseases* **4**, 46-51 (2013).

12 Giardina, A. R. S., K. A. & Schauber, E. M. O., R. S. Modeling the role of songbirds and rodents in the ecology of Lyme disease. *Canadian Journal of Zoology* (2000).

13 LoGiudice, K., Ostfeld, R. S., Schmidt, K. A. & Keesing, F. The ecology of infectious disease: effects of host diversity and community composition on Lyme disease risk. *Proc Natl Acad Sci U S A* **100**, 567-571, doi:10.1073/pnas.0233733100 (2003).

14 Mather, T. N., Wilson, M. L., Moore, S. I., Ribeiro, J. M. C. & Speilman, A. Comparing The Relative Potential Of Rodents As Reservoirs Of The Lyme Disease Spirochete (Borrelia Burgdorferi). *American Journal of Epidemiology* (1989).

15 Eisen, L. & Eisen, R. J. Critical Evaluation of the Linkage Between Tick-Based Risk Measures and the Occurrence of Lyme Disease Cases. *Journal of Medical Entomology* (2018).

16 Roome, A., Hill, L., Al-Feghali, V., Murnock, C. G., Goodsell, J. A., Spathis, R. & Garruto, R. M. Impact of white-tailed deer on the spread of Borrelia burgdorferi. *Med Vet Entomol* **31**, 1-5, doi:10.1111/mve.12191 (2017).

17 Huang, C. I., Kay, S. C., Davis, S., Tufts, D. M., Gaffett, K., Tefft, B. & Diuk-Wasser, M. A. High burdens of Ixodes scapularis larval ticks on white-tailed deer may limit Lyme

disease risk in a low biodiversity setting. *Ticks Tick Borne Dis* **10**, 258-268, doi:10.1016/j.ttbdis.2018.10.013 (2019).

18 Voordouw, M. J., Lachish, S. & Dolan, M. C. The lyme disease pathogen has no effect on the survival of its rodent reservoir host. *PLoS One* **10**, e0118265, doi:10.1371/journal.pone.0118265 (2015).

19 Steere, A. C. Medical Progress — Lyme Disease. *The New England Journal of Medicine* **321** (1989).

20 Hirsch, A. G., Herman, R. J., Rebman, A., Moon, K. A., Aucott, J., Heaney, C. & Schwartz, B. S. Obstacles to diagnosis and treatment of Lyme disease in the USA: a qualitative study. *BMJ Open* **8**, e021367, doi:10.1136/bmjopen-2017-021367 (2018).

21 Arvikar, S. L. & Steere, A. C. Diagnosis and treatment of Lyme arthritis. *Infect Dis Clin North Am* **29**, 269-280, doi:10.1016/j.idc.2015.02.004 (2015).

22 Esposito, S., Bosis, S., Sabatini, C., Tagliaferri, L. & Principi, N. Borrelia burgdorferi infection and Lyme disease in children. *Int J Infect Dis* **17**, e153-158, doi:10.1016/j.ijid.2012.09.014 (2013).

23 Steere, A. C., Strle, F., Wormser, G. P., Hu, L. T., Branda, J. A., Hovius, J. W., Li, X. & Mead, P. S. Lyme borreliosis. *Nat Rev Dis Primers* **2**, 16090, doi:10.1038/nrdp.2016.90 (2016).

24 Marques, A. R. Laboratory diagnosis of Lyme disease: advances and challenges. *Infect Dis Clin North Am* **29**, 295-307, doi:10.1016/j.idc.2015.02.005 (2015).

25 Vollmer, W. Structural variation in the glycan strands of bacterial peptidoglycan. *FEMS Microbiol Rev* **32**, 287-306, doi:10.1111/j.1574-6976.2007.00088.x (2008).

26 Vollmer, W. & Holtje, J. V. The architecture of the murein (peptidoglycan) in gram-negative bacteria: vertical scaffold or horizontal layer(s)? *J Bacteriol* **186**, 5978-5987, doi:10.1128/JB.186.18.5978-5987.2004 (2004).

27 van Heijenoort, J. Formation of the glycan chains in the synthesis of bacterial peptidoglycan. *Glycobiology* **11** (2001).

28 Vollmer, W., Blanot, D. & de Pedro, M. A. Peptidoglycan structure and architecture. *FEMS Microbiol Rev* **32**, 149-167, doi:10.1111/j.1574-6976.2007.00094.x (2008).

29 Scheffers, D. J. & Pinho, M. G. Bacterial cell wall synthesis: new insights from localization studies. *Microbiol Mol Biol Rev* **69**, 585-607, doi:10.1128/MMBR.69.4.585-607.2005 (2005).

30 Gumbart, J. C., Beeby, M., Jensen, G. J. & Roux, B. Escherichia coli peptidoglycan structure and mechanics as predicted by atomic-scale simulations. *PLoS Comput Biol* **10**, e1003475, doi:10.1371/journal.pcbi.1003475 (2014).

31 Kim, S. J., Chang, J. & Singh, M. Peptidoglycan architecture of Gram-positive bacteria by solid-state NMR. *Biochim Biophys Acta* **1848**, 350-362, doi:10.1016/j.bbamem.2014.05.031 (2015).

32 Typas, A., Banzhaf, M., Gross, C. A. & Vollmer, W. From the regulation of peptidoglycan synthesis to bacterial growth and morphology. *Nat Rev Microbiol* **10**, 123-136, doi:10.1038/nrmicro2677 (2011).

33 Egan, A. J., Cleverley, R. M., Peters, K., Lewis, R. J. & Vollmer, W. Regulation of bacterial cell wall growth. *FEBS J* **284**, 851-867, doi:10.1111/febs.13959 (2017).

34 Kohanski, M. A., Dwyer, D. J. & Collins, J. J. How antibiotics kill bacteria: from targets to networks. *Nat Rev Microbiol* **8**, 423-435, doi:10.1038/nrmicro2333 (2010).

35 Wolf, A. J. & Underhill, D. M. Peptidoglycan recognition by the innate immune system. *Nat Rev Immunol* **18**, 243-254, doi:10.1038/nri.2017.136 (2018).

36 Fraser, C. M., Casjens, S., Huang, W. M., Sutton, G. G., Clayton, R. & Lathriga, R. Genomic sequence of a Lyme disease spirochaete, Borrelia burgdorferi. *Nature* **390** (1997).

37 de Silva, A. M. & Fikrig, E. Arthropod- and host-specific gene expression by Borrelia burgdorferi. *J Clin Invest* **99**, 377-379, doi:10.1172/JCI119169 (1997).

38 Jutras, B. L., Savage, C. R., Arnold, W. K., Lethbridge, K. G., Carroll, D. W., Tilly, K., Bestor, A., Zhu, H., Seshu, J., Zuckert, W. R., Stewart, P. E., Rosa, P. A., Brissette, C. A. & Stevenson, B. The Lyme disease spirochete's BpuR DNA/RNA-binding protein is differentially expressed during the mammal-tick infectious cycle, which affects translation of the SodA superoxide dismutase. *Mol Microbiol* **112**, 973-991, doi:10.1111/mmi.14336 (2019).

39 Takayama, K., Rothenberg, R. J. & Barbour, A. G. Absence of Lipopolysaccharide in the Lyme Disease Spirochete, Borrelia burgdorferi. *Infection and Immunity* **55**, 2311-2313 (1987).

40 Crowley, J. T., Toledo, A. M., LaRocca, T. J., Coleman, J. L., London, E. & Benach, J. L. Lipid exchange between Borrelia burgdorferi and host cells. *PLoS Pathog* **9**, e1003109, doi:10.1371/journal.ppat.1003109 (2013).

41 Zuckert, W. R. Secretion of bacterial lipoproteins: through the cytoplasmic membrane, the periplasm and beyond. *Biochim Biophys Acta* **1843**, 1509-1516, doi:10.1016/j.bbamcr.2014.04.022 (2014).

42 Motaleb, M. A., Corum, L., Bono, J. L., Elias, A. F., Rosa, P., Samuels, D. S. & Charon, N. W. Borrelia burgdorferi periplasmic flagella have both skeletal and motility functions. *Proc Natl Acad Sci U S A* **97**, 10899-10904, doi:10.1073/pnas.200221797 (2000).

43 Dombrowski, C., Kan, W., Motaleb, M. A., Charon, N. W., Goldstein, R. E. & Wolgemuth, C. W. The elastic basis for the shape of Borrelia burgdorferi. *Biophys J* **96**, 4409-4417, doi:10.1016/j.bpj.2009.02.066 (2009).

44 Sultan, S. Z., Manne, A., Stewart, P. E., Bestor, A., Rosa, P. A., Charon, N. W. & Motaleb, M. A. Motility is crucial for the infectious life cycle of Borrelia burgdorferi. *Infect Immun* **81**, 2012-2021, doi:10.1128/IAI.01228-12 (2013).

45 Yang, J., Huber, G. & Wolgemuth, C. W. Forces and Torques on Rotating Spirochete Flagella. *Physical Review Letters* (2011).

46 Jutras, B. L., Lochhead, R. B., Kloos, Z. A., Biboy, J., Strle, K., Booth, C. J., Govers, S. K., Gray, J., Schumann, P., Vollmer, W., Bockenstedt, L. K., Steere, A. C. & Jacobs-Wagner, C. Borrelia burgdorferi peptidoglycan is a persistent antigen in patients with Lyme arthritis. *Proc Natl Acad Sci U S A* **116**, 13498-13507, doi:10.1073/pnas.1904170116 (2019).

47 Davis, M. M., Brock, A., DeHart, T. G., Boribong, B. P., Lee, K., McClune, M. E., Chang, Y., Cramer, N., Liu, J., Jones, C. N. & Jutras, B. L. The peptidoglycan-associated protein NapA plays an important role in the envelope integrity and in the pathogenesis of the Lyme Disease Spirochete. *PLoS Pathog* **In Press** (2021).

48 Cameron, T. A., Anderson-Furgeson, J., Zupan, J. R., Zik, J. J. & Zambryski, P. C. Peptidoglycan synthesis machinery in Agrobacterium tumefaciens during unipolar growth and cell division. *mBio* **5**, e01219-01214, doi:10.1128/mBio.01219-14 (2014).

49 Gray, A. N., Egan, A. J., Van't Veer, I. L., Verheul, J., Colavin, A., Koumoutsi, A., Biboy, J., Altelaar, A. F., Damen, M. J., Huang, K. C., Simorre, J. P., Breukink, E., den Blaauwen, T., Typas, A., Gross, C. A. & Vollmer, W. Coordination of peptidoglycan synthesis and outer membrane constriction during Escherichia coli cell division. *Elife* **4**, doi:10.7554/eLife.07118 (2015).

50 Jutras, B. L., Scott, M., Parry, B., Biboy, J., Gray, J., Vollmer, W. & Jacobs-Wagner, C. Lyme disease and relapsing fever Borrelia elongate through zones of peptidoglycan synthesis that mark division sites of daughter cells. *Proc Natl Acad Sci U S A* **113**, 9162-9170, doi:10.1073/pnas.1610805113 (2016).

51 Macheboeuf, P., Contreras-Martel, C., Job, V., Dideberg, O. & Dessen, A. Penicillin binding proteins: key players in bacterial cell cycle and drug resistance processes. *FEMS Microbiol Rev* **30**, 673-691, doi:10.1111/j.1574-6976.2006.00024.x (2006).

52 Sauvage, E., Kerff, F., Terrak, M., Ayala, J. A. & Charlier, P. The penicillin-binding proteins: structure and role in peptidoglycan biosynthesis. *FEMS Microbiol Rev* **32**, 234-258, doi:10.1111/j.1574-6976.2008.00105.x (2008).

53 Bush, K. & Bradford, P. A. beta-Lactams and beta-Lactamase Inhibitors: An Overview. *Cold Spring Harb Perspect Med* **6**, doi:10.1101/cshperspect.a025247 (2016).

54 Zapun, A., Contreras-Martel, C. & Vernet, T. Penicillin-binding proteins and beta-lactam resistance. *FEMS Microbiol Rev* **32**, 361-385, doi:10.1111/j.1574-6976.2007.00095.x (2008).

55 Stapleton, P. D. & Taylor, P. W. Methicillin resistance in Staphylococcus aureus. *Sci Prog.* **85**, 57-72 (2002).

56 Otero, L. H., Rojas-Altuve, A., Llarrull, L. I., Carrasco-Lopez, C., Kumarasiri, M., Lastochkin, E., Fishovitz, J., Dawley, M., Hesek, D., Lee, M., Johnson, J. W., Fisher, J. F., Chang, M., Mobashery, S. & Hermoso, J. A. How allosteric control of Staphylococcus aureus penicillin binding protein 2a enables methicillin resistance and physiological function. *Proc Natl Acad Sci U S A* **110**, 16808-16813, doi:10.1073/pnas.1300118110 (2013).

57 Barbour, A. G. Phylogeny of a relapsing fever Borrelia species transmitted by the hard tick Ixodes scapularis. *Infect Genet Evol* **27**, 551-558, doi:10.1016/j.meegid.2014.04.022 (2014).

58 Chomel, B. Lyme disease. *Rev Sci Tech Off Int Epiz* **34**, 569-576 (2015).

59 Rar, V., Livanova, N., Tkachev, S., Kaverina, G., Tikunov, A., Sabitova, Y., Igolkina, Y., Panov, V., Livanov, S., Fomenko, N., Babkin, I. & Tikunova, N. Detection and genetic characterization of a wide range of infectious agents in Ixodes pavlovskyi ticks in Western Siberia, Russia. *Parasit Vectors* **10**, 258, doi:10.1186/s13071-017-2186-5 (2017).

60 Yamaji, K., Aonuma, H. & Kanuka, H. Distribution of tick-borne diseases in Japan: Past patterns and implications for the future. *J Infect Chemother* **24**, 499-504, doi:10.1016/j.jiac.2018.03.012 (2018).

61 Wu, X., Na, R., Wei, S., Zhu, J. & Peng, H. Distribution of tick-borne diseases in China. *Parasites & Vectors* (2013).

62 Brandt, F. C., Ertas, B., Falk, T. M., Metze, D. & Böer-Auer, A. Histopathology and immunophenotype of acrodermatitis chronica atrophicans correlated with ospA and ospC genotypes of Borrelia species. *Journal of Cutaneous Pathology* (2015).

63 Hildenbrand, P., Craven, D. E., Jones, R. & Nemeskal, P. Lyme neuroborreliosis: manifestations of a rapidly emerging zoonosis. *AJNR Am J Neuroradiol* **30**, 1079-1087, doi:10.3174/ajnr.A1579 (2009).

64 Rudenko, N., Golovchenko, M., Grubhoffer, L. & Oliver, J. H., Jr. Updates on Borrelia burgdorferi sensu lato complex with respect to public health. *Ticks Tick Borne Dis* **2**, 123-128, doi:10.1016/j.ttbdis.2011.04.002 (2011).

65 Purser, J. E. N., S. J. Correlation between plasmid content and infectivity in Borrelia burgdorferi. *PNAS Microbiology* **97** (2000).

66 Tilly, K. G., D.; Bueschel, D. M.; Krum, J. G.; Rosa, P. Infectious Cycle Analysis of a Borrelia burgdorferi Mutant Defective in Transport of Chitobiose, a Tick Cuticle Component. *Vector-Borne and Zoonotic Diseases* **4**, 159-168 (2004).

67 Deatherage, D. E. & Barrick, J. E. Identification of mutations in laboratory-evolved microbes from next-generation sequencing data using breseq. *Methods Mol Biol* **1151**, 165-188, doi:10.1007/978-1-4939-0554-6_12 (2014).

68 Tautenhahn, R., Bottcher, C. & Neumann, S. Highly sensitive feature detection for high resolution LC/MS. *BMC Bioinformatics* **9**, 504, doi:10.1186/1471-2105-9-504 (2008).

69 R: A language and environment for statistical computing (R Foundation for Statistical Computing, Vienna, Austria, 2020).

70 RAMClustR: Mass Spectrometry Metabolomics Feature Clustering and Interpretation v. R Package Version 1.1.0 (2019).

71 Chong, J., Soufan, O., Li, C., Caraus, I., Li, S., Bourque, G., Wishart, D. S. & Xia, J. MetaboAnalyst 4.0: towards more transparent and integrative metabolomics analysis. *Nucleic Acids Res* **46**, W486-W494, doi:10.1093/nar/gky310 (2018).

72 Pena, M. J., Tuomivaara, S. T., Urbanowicz, B. R., O'Neill, M. A. & York, W. S. Methods for structural characterization of the products of cellulose- and xyloglucan-hydrolyzing enzymes. *Methods Enzymol* **510**, 121-139, doi:10.1016/B978-0-12-415931-0.00007-0 (2012).

73 Zückert, W. R. Laboratory Maintenance Of Borrelia. *Current Protocols in Microbiology* (2007).

74 Paintdakhi, A., Parry, B., Campos, M., Irnov, I., Elf, J., Surovtsev, I. & Jacobs-Wagner, C. Oufti: an integrated software package for high-accuracy, high-throughput quantitative microscopy analysis. *Mol Microbiol* **99**, 767-777, doi:10.1111/mmi.13264 (2016).

75 Hart, M., Lauer, J., Selig, M., Hanak, M., Walters, B. & Rolauffs, B. Shaping the Cell and the Future: Recent Advancements in Biophysical Aspects Relevant to Regenerative Medicine. *Journal of Functional Morphology and Kinesiology* **3**, doi:10.3390/jfmk3010002 (2017).

76 Gibson, D. G., Young, L., Chuang, R. Y., Venter, J. C., Hutchison, C. A., 3rd & Smith, H. O. Enzymatic assembly of DNA molecules up to several hundred kilobases. *Nat Methods* **6**, 343-345, doi:10.1038/nmeth.1318 (2009).

77 Branda, J. A., Body, B. A., Boyle, J., Branson, B. M., Dattwyler, R. J., Fikrig, E., Gerald, N. J., Gomes-Solecki, M., Kintrup, M., Ledizet, M., Levin, A. E., Lewinski, M., Liotta, L. A., Marques, A., Mead, P. S., Mongodin, E. F., Pillai, S., Rao, P., Robinson, W. H., Roth, K. M., Schriefer, M. E., Slezak, T., Snyder, J., Steere, A. C., Witkowski, J., Wong, S. J. & Schutzer, S. E. Advances in Serodiagnostic Testing for Lyme Disease Are at Hand. *Clin Infect Dis* **66**, 1133-1139, doi:10.1093/cid/cix943 (2018).

78 Steere, A. C. Treatment of Lyme Arthritis. *J Rheumatol* **46**, 871-873, doi:10.3899/jrheum.190320 (2019).

79 Beck, G. B., J. L.; Habicht G. S. Isolation, preliminary chemical characterization, and biological acitity of Borrelia burgdorferi peptidoglycan. *Biochemical and Biophysical Research Communications* **167**, 89-95 (1990).

80 Barbour, A. G. Isolation and Cultivation of Lyme Disease Spirochetes. *The Yale Journal of Biology and Medicine*, 521-525 (1984).

81 Schneider, E. M. & Rhodes, R. G. N-acetylmannosamine (ManNAc) supports the growth of Borrelia burgdorferi in the absence of N-acetylglucosamine (GlcNAc). *FEMS Microbiol Lett* **365**, doi:10.1093/femsle/fny243 (2018).

82 Tilly, K., Elias, A. F., Errett, J., Fischer, E., Iyer, R., Schwartz, I., Bono, J. L. & Rosa, P. Genetics and regulation of chitobiose utilization in Borrelia burgdorferi. *J Bacteriol* **183**, 5544-5553, doi:10.1128/JB.183.19.5544-5553.2001 (2001).

83 von Lackum, K. & Stevenson, B. Carbohydrate utilization by the Lyme borreliosis spirochete, Borrelia burgdorferi. *FEMS Microbiol Lett* **243**, 173-179, doi:10.1016/j.femsle.2004.12.002 (2005).

84 Sze, C. W., Smith, A., Choi, Y. H., Yang, X., Pal, U., Yu, A. & Li, C. Study of the response regulator Rrp1 reveals its regulatory role in chitobiose utilization and virulence of Borrelia burgdorferi. *Infect Immun* **81**, 1775-1787, doi:10.1128/IAI.00050-13 (2013).

85 Elias, A. F., Stewart, P. E., Grimm, D., Caimano, M. J., Eggers, C. H., Tilly, K., Bono, J. L., Akins, D. R., Radolf, J. D., Schwan, T. G. & Rosa, P. Clonal polymorphism of Borrelia burgdorferi strain B31 MI: implications for mutagenesis in an infectious strain background. *Infect Immun* **70**, 2139-2150, doi:10.1128/iai.70.4.2139-2150.2002 (2002).

86 Jewett, M. W., Lawrence, K., Bestor, A. C., Tilly, K., Grimm, D., Shaw, P., VanRaden, M., Gherardini, F. & Rosa, P. A. The critical role of the linear plasmid lp36 in the infectious cycle of Borrelia burgdorferi. *Mol Microbiol* **64**, 1358-1374, doi:10.1111/j.1365-2958.2007.05746.x (2007).

87 Kawabata, H., Norris, S. J. & Watanabe, H. BBE02 disruption mutants of Borrelia burgdorferi B31 have a highly transformable, infectious phenotype. *Infect Immun* **72**, 7147-7154, doi:10.1128/IAI.72.12.7147-7154.2004 (2004).

88 Coutte, L., Botkin, D. J., Gao, L. & Norris, S. J. Detailed analysis of sequence changes occurring during vlsE antigenic variation in the mouse model of Borrelia burgdorferi infection. *PLoS Pathog* **5**, e1000293, doi:10.1371/journal.ppat.1000293 (2009).

89 Chou, S., Daugherty, M. D., Peterson, S. B., Biboy, J., Yang, Y., Jutras, B. L., Fritz-Laylin, L. K., Ferrin, M. A., Harding, B. N., Jacobs-Wagner, C., Yang, X. F., Vollmer, W., Malik, H. S. & Mougous, J. D. Transferred interbacterial antagonism genes augment eukaryotic innate immune function. *Nature* **518**, 98-101, doi:10.1038/nature13965 (2015).

90 Zhu, Z., Gern, L. & Aeschlimann, A. The peritrophic membrane of Ixodes ricinus. *Parisitology Research* **77**, 635-641 (1991).

91 Charon, N. W., Goldstein, S. F., Marko, M., Hsieh, C., Gebhardt, L. L., Motaleb, M. A., Wolgemuth, C. W., Limberger, R. J. & Rowe, N. The flat-ribbon configuration of the periplasmic flagella of Borrelia burgdorferi and its relationship to motility and morphology. *J Bacteriol* **191**, 600-607, doi:10.1128/JB.01288-08 (2009).

92 Harman, M. W., Dunham-Ems, S. M., Caimano, M. J., Belperron, A. A., Bockenstedt, L. K., Fu, H. C., Radolf, J. D. & Wolgemuth, C. W. The heterogeneous motility of the Lyme

disease spirochete in gelatin mimics dissemination through tissue. *Proc Natl Acad Sci U S A* **109**, 3059-3064, doi:10.1073/pnas.1114362109 (2012).

93 Malawista, S. E. & de Boisfleury Chevance, A. Clocking the Lyme spirochete. *PLoS One* **3**, e1633, doi:10.1371/journal.pone.0001633 (2008).

94 Goldstein, S. F., Charon, N. W. & Kreiling, J. A. Borrelia burgdorferi swims with a planarwaveform similar to that of eukaryoticflagella. *PNAS* **91**, 3433-3437 (1994).

95 Milner, D. S., Ray, L. J., Saxon, E. B., Lambert, C., Till, R., Fenton, A. K. & Sockett, R. E. DivIVA Controls Progeny Morphology and Diverse ParA Proteins Regulate Cell Division or Gliding Motility in Bdellovibrio bacteriovorus. *Front Microbiol* **11**, 542, doi:10.3389/fmicb.2020.00542 (2020).

96 Takashimizu, Y. & Iiyoshi, M. New parameter of roundness R: circularity corrected by aspect ratio. *Progress in Earth and Planetary Science* **3**, doi:10.1186/s40645-015-0078-x (2016).

97 Charon, N. W. & Goldstein, S. F. Genetics of Motility and Chemotaxis of a Fascinating Group of Bacteria: The Spirochetes. *Annual Review of Genetics* **36**, 47-73 (2002).

98 Irazoki, O., Hernandez, S. B. & Cava, F. Peptidoglycan Muropeptides: Release, Perception, and Functions as Signaling Molecules. *Front Microbiol* **10**, 500, doi:10.3389/fmicb.2019.00500 (2019).

99 Radolf, J. D. & Samuels, D. S. *Lyme Disease and Relapsing Fever Spirochetes: Genomics, Molecular Biology, Host Interactions and Disease Pathogenesis*. 181-220 (Caister Academic Press, 2021).

100 Yao, X., Jericho, M., Pink, D. & Beveridge, T. Thickness and Elasticity of Gram-Negative Murein Sacculi Measured by Atomic Force Microscopy. *Journal Of Bacteriology* **181**, 6865–6875 (1999).

101 Radolf, J. D., Caimano, M. J., Stevenson, B. & Hu, L. T. Of ticks, mice and men: understanding the dual-host lifestyle of Lyme disease spirochaetes. *Nat Rev Microbiol* **10**, 87-99, doi:10.1038/nrmicro2714 (2012).

102 Jutras, B. L., Chenail, A. M. & Stevenson, B. Changes in bacterial growth rate govern expression of the Borrelia burgdorferi OspC and Erp infection-associated surface proteins. *J Bacteriol* **195**, 757-764, doi:10.1128/JB.01956-12 (2013).

103 Stewart, P. E. & Bloom, M. E. Sharing the Ride: Ixodes scapularis Symbionts and Their Interactions. *Front Cell Infect Microbiol* **10**, 142, doi:10.3389/fcimb.2020.00142 (2020).

104 Narasimhan, S., Rajeevan, N., Liu, L., Zhao, Y. O., Heisig, J., Pan, J., Eppler-Epstein, R., Deponte, K., Fish, D. & Fikrig, E. Gut microbiota of the tick vector Ixodes scapularis modulate colonization of the Lyme disease spirochete. *Cell Host Microbe* **15**, 58-71, doi:10.1016/j.chom.2013.12.001 (2014).

105 Abraham, N. M., Liu, L., Jutras, B. L., Yadav, A. K., Narasimhan, S., Gopalakrishnan, V., Ansari, J. M., Jefferson, K. K., Cava, F., Jacobs-Wagner, C. & Fikrig, E. Pathogen-mediated manipulation of arthropod microbiota to promote infection. *Proc Natl Acad Sci U S A* **114**, E781-E790, doi:10.1073/pnas.1613422114 (2017).

106 Zhang, K., Bian, J., Deng, Y., Smith, A., Nunez, R. E., Li, M. B., Pal, U., Yu, A. M., Qiu, W., Ealick, S. E. & Li, C. Lyme disease spirochaete Borrelia burgdorferi does not require thiamin. *Nat Microbiol* **2**, 16213, doi:10.1038/nmicrobiol.2016.213 (2016).

107 Barbour, A. G. *Borrelia: a Diverse and Ubiquitous Genus of Tick-Borne Pathogens*. (ASM Press, 2001).

108 Petrulioniene, A., Radzisauskiene, D., Ambrozaitis, A., Caplinskas, S., Paulauskas, A. & Venalis, A. Epidemiology of Lyme Disease in a Highly Endemic European Zone. *Medicina (Kaunas)* **56**, doi:10.3390/medicina56030115 (2020).

109 Schwan, T. G. & Piesman, J. Vector Interactions and Molecular Adaptations of Lyme Disease and Relapsing Fever Spirochetes Associated with Transmission by Ticks. *Emerging Infectious Diseases* (2002).

110 Cutler, S. J. Possibilities for Relapsing Fever Reemergence. *Emerging Infectious Diseases*, 369-374 (2006).

111 Dworkin, M. S., Schwan, T. G., Anderson, D. E., Jr. & Borchardt, S. M. Tick-borne relapsing fever. *Infect Dis Clin North Am* **22**, 449-468, viii, doi:10.1016/j.idc.2008.03.006 (2008).

112 Talagrand-Reboul, E., Boyer, P. H., Bergstrom, S., Vial, L. & Boulanger, N. Relapsing Fevers: Neglected Tick-Borne Diseases. *Front Cell Infect Microbiol* **8**, 98, doi:10.3389/fcimb.2018.00098 (2018).

113 Cadavid, D. & Barbour, A. G. Neuroborreliosis During Relapsing Fever- Review of the Clinical Manifestations, Pathology, and Treatment of Infections in Humans and Experimental Animals. *Clinical Infectious Diseases* **26** (1998).

114 Asong, J., Wolfert, M. A., Maiti, K. K., Miller, D. & Boons, G. J. Binding and Cellular Activation Studies Reveal That Toll-like Receptor 2 Can Differentially Recognize Peptidoglycan from Gram-positive and Gram-negative Bacteria. *J Biol Chem* **284**, 8643-8653, doi:10.1074/jbc.M806633200 (2009).

115 Pritt, B. S., Respicio-Kingry, L. B., Sloan, L. M., Schriefer, M. E., Replogle, A. J., Bjork, J., Liu, G., Kingry, L. C., Mead, P. S., Neitzel, D. F., Schiffman, E., Hoang Johnson, D. K., Davis, J. P., Paskewitz, S. M., Boxrud, D., Deedon, A., Lee, X., Miller, T. K., Feist, M. A., Steward, C. R., Theel, E. S., Patel, R., Irish, C. L. & Petersen, J. M. Borrelia mayonii sp. nov., a member of the Borrelia burgdorferi sensu lato complex, detected in patients and ticks in the upper midwestern United States. *Int J Syst Evol Microbiol* **66**, 4878-4880, doi:10.1099/ijsem.0.001445 (2016).

116 Meri, T., Cutler, S. J., Blom, A. M., Meri, S. & Jokiranta, T. S. Relapsing fever spirochetes Borrelia recurrentis and B. duttonii acquire complement regulators C4b-binding protein and factor H. *Infect Immun* **74**, 4157-4163, doi:10.1128/IAI.00007-06 (2006).

117 Bouhss, A., Crouvoisier, M., Blanot, D. & Mengin-Lecreulx, D. Purification and characterization of the bacterial MraY translocase catalyzing the first membrane step of peptidoglycan biosynthesis. *J Biol Chem* **279**, 29974-29980, doi:10.1074/jbc.M314165200 (2004).

118 Laddomada, F., Miyachiro, M. M., Jessop, M., Patin, D., Job, V., Mengin-Lecreulx, D., Le Roy, A., Ebel, C., Breyton, C., Gutsche, I. & Dessen, A. The MurG glycosyltransferase provides an oligomeric scaffold for the cytoplasmic steps of peptidoglycan biosynthesis in the human pathogen Bordetella pertussis. *Sci Rep* **9**, 4656, doi:10.1038/s41598-019-40966-z (2019).

119 Kuk, A. C. Y., Hao, A., Guan, Z. & Lee, S. Y. Visualizing conformation transitions of the Lipid II flippase MurJ. *Nat Commun* **10**, 1736, doi:10.1038/s41467-019-09658-0 (2019).

120 Vigouroux, A., Cordier, B., Aristov, A., Alvarez, L., Ozbaykal, G., Chaze, T., Oldewurtel, E. R., Matondo, M., Cava, F., Bikard, D. & van Teeffelen, S. Class-A penicillin binding proteins do not contribute to cell shape but repair cell-wall defects. *Elife* **9**, doi:10.7554/eLife.51998 (2020).

121 Palzkill, T. Metallo-beta-lactamase structure and function. *Ann N Y Acad Sci* **1277**, 91-104, doi:10.1111/j.1749-6632.2012.06796.x (2013).

122 Beadle, B. M., Nicholas, R. A. & Shoichet, B. K. Interaction energies between beta-lactam antibiotics and E. coli penicillin-binding protein 5 by reversible thermal denaturation. *Protein Sci* **10**, 1254-1259, doi:10.1110/ps.52001 (2001).

123 Fernandes, R., Amador, P. & Prudêncio, C. β-Lactams: chemical structure, mode of action and mechanisms of resistance. *Reviews in Medical Microbiology* **24**, 7-17, doi:10.1097/MRM.0b013e3283587727 (2013).

124 Kocaoglu, O. & Carlson, E. E. Profiling of beta-lactam selectivity for penicillin-binding proteins in Escherichia coli strain DC2. *Antimicrob Agents Chemother* **59**, 2785-2790, doi:10.1128/AAC.04552-14 (2015).

125 Kocaoglu, O. & Carlson, E. E. Penicillin-binding protein imaging probes. *Curr Protoc Chem Biol* **5**, 239-250, doi:10.1002/9780470559277.ch130102 (2013).

126 Reshes, G., Vanounou, S., Fishov, I. & Feingold, M. Cell shape dynamics in Escherichia coli. *Biophys J* **94**, 251-264, doi:10.1529/biophysj.107.104398 (2008).

127 Des Soye, B. J., Davidson, S. R., Weinstock, M. T., Gibson, D. G. & Jewett, M. C. Establishing a High-Yielding Cell-Free Protein Synthesis Platform Derived from Vibrio natriegens. *ACS Synth Biol* **7**, 2245-2255, doi:10.1021/acssynbio.8b00252 (2018).

Appendix

Characterization of Peptidoglycan, and the Enzymes that Synthesize it, in *Borrelia burgdorferi* and Insights into the Peptidoglycan of Other Pathogenic *Borrelia*

Tanner Gage DeHart

This appendix includes:

Figs. S1-S34
Tables S1-S6
Datasets S1-S2

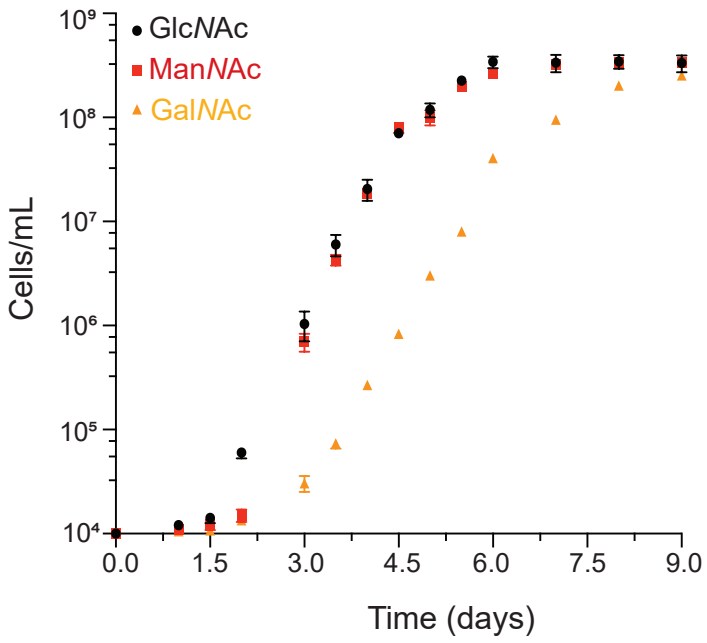

Supplemental Figure 1: Growth of 5A11 *B. burgdorferi* in BSK-II complete media supplemented with Glc*N*Ac, Man*N*Ac, or Gal*N*Ac.

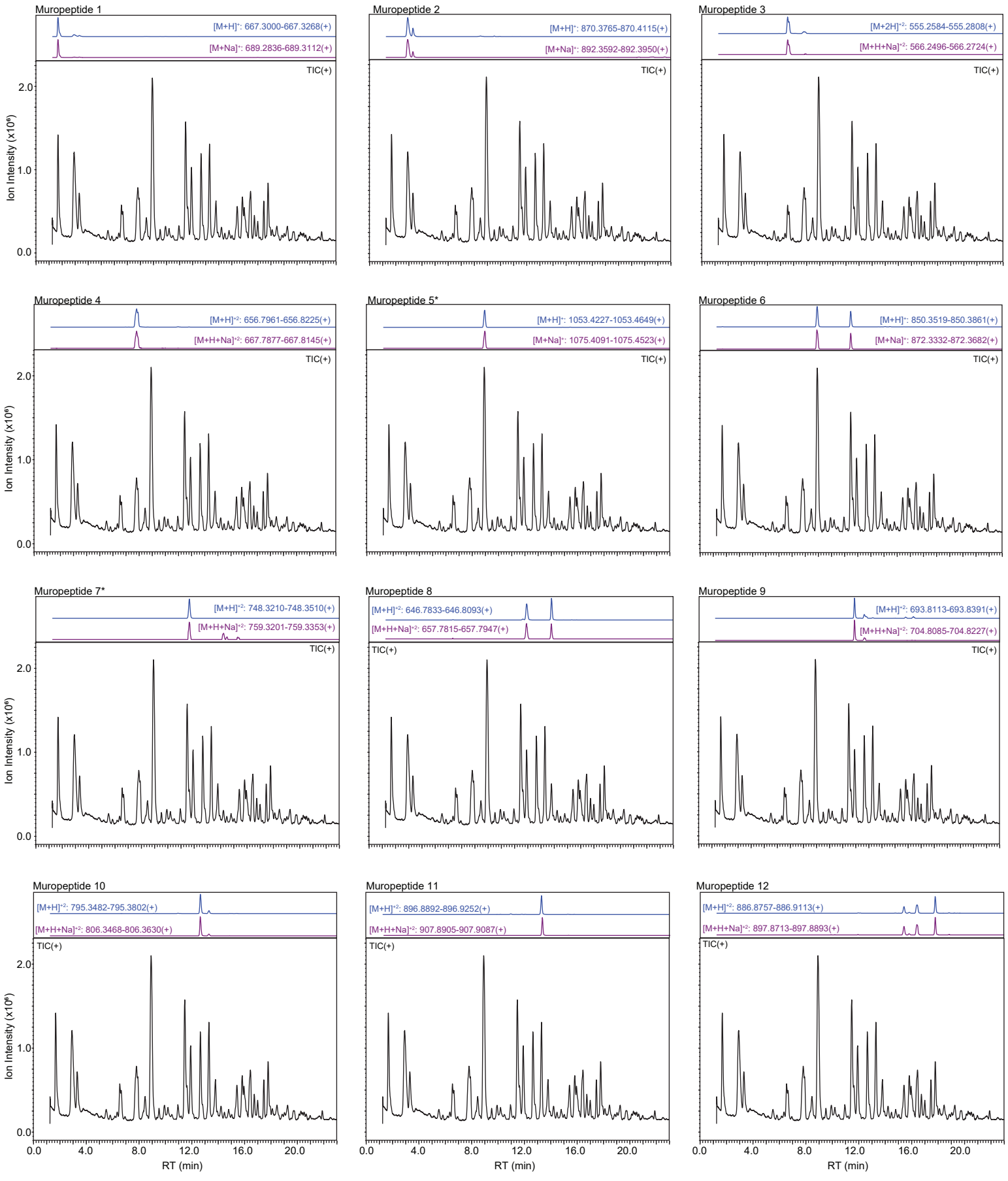
Muropeptide 1
[M+H]+: 667.3000-667.3268(+)
[M+Na]+: 689.2836-689.3112(+)
TIC(+)
Muropeptide 2
[M+H]+: 870.3765-870.4115(+)
[M+Na]+: 892.3592-892.3950(+)
TIC(+)
Muropeptide 3
[M+2H]+2: 555.2584-555.2808(+)
[M+H+Na]+2: 566.2496-566.2724(+)
TIC(+)
Muropeptide 4
[M+H]+2: 656.7961-656.8225(+)
[M+H+Na]+2: 667.7877-667.8145(+)
TIC(+)
Muropeptide 5*
[M+H]+: 1053.4227-1053.4649(+)
[M+Na]+: 1075.4091-1075.4523(+)
TIC(+)
Muropeptide 6
[M+H]+: 850.3519-850.3861(+)
[M+Na]+: 872.3332-872.3682(+)
TIC(+)
Muropeptide 7*
[M+H]+2: 748.3210-748.3510(+)
[M+H+Na]+2: 759.3201-759.3353(+)
TIC(+)
Muropeptide 8
[M+H]+2: 646.7833-646.8093(+)
[M+H+Na]+2: 657.7815-657.7947(+)
TIC(+)
Muropeptide 9
[M+H]+2: 693.8113-693.8391(+)
[M+H+Na]+2: 704.8085-704.8227(+)
TIC(+)
Muropeptide 10
[M+H]+2: 795.3482-795.3802(+)
[M+H+Na]+2: 806.3468-806.3630(+)
TIC(+)
Muropeptide 11
[M+H]+2: 896.8892-896.9252(+)
[M+H+Na]+2: 907.8905-907.9087(+)
TIC(+)
Muropeptide 12
[M+H]+2: 886.8757-886.9113(+)
[M+H+Na]+2: 897.8713-897.8893(+)
TIC(+)
Ion Intensity (x10⁶)
0.0
1.0
2.0
0.0
4.0
8.0
12.0
16.0
20.0
RT (min)

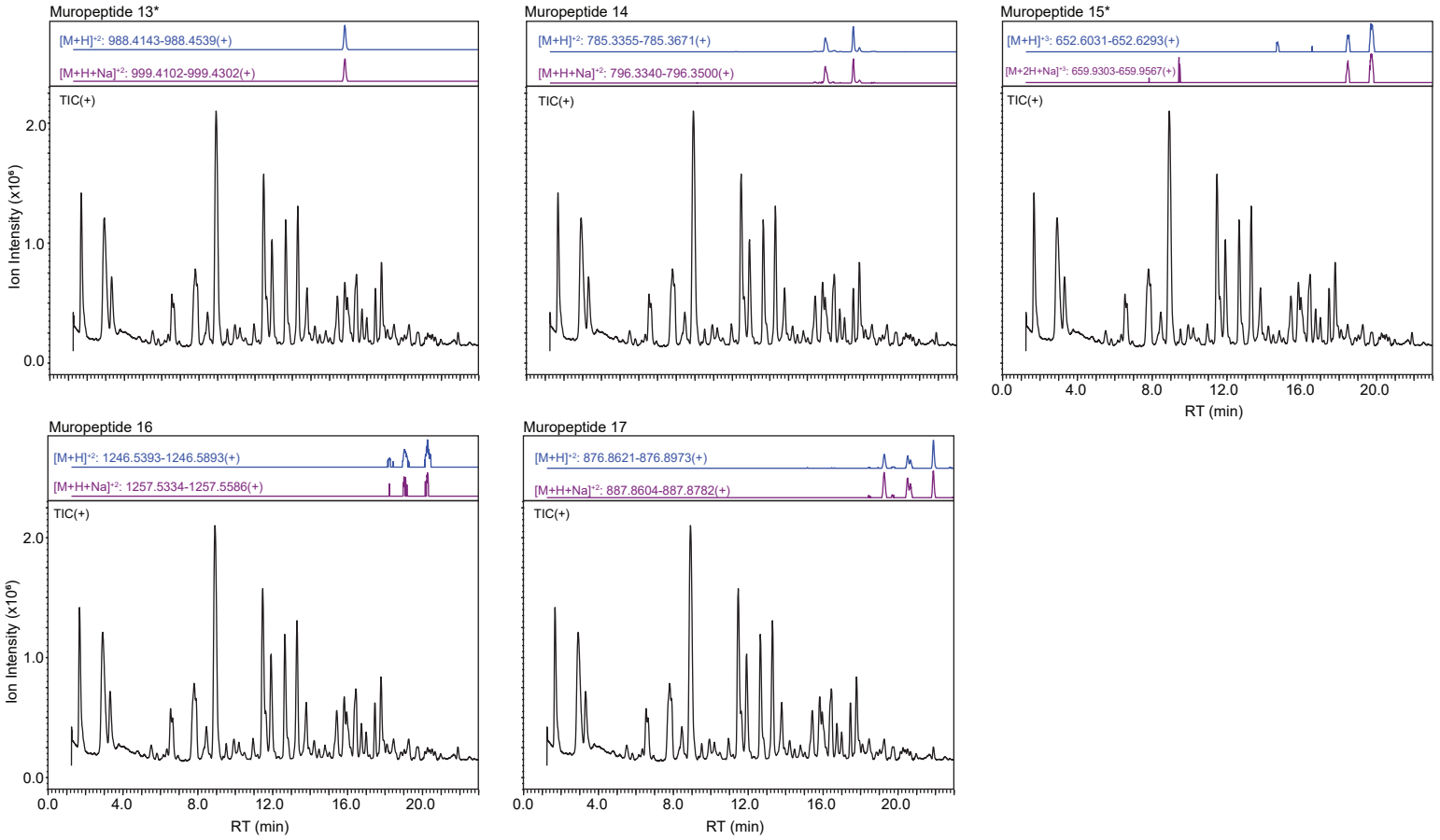

Supplemental Figure 2: LCMS chromatograms by muropeptide – TICs are shown in black with the [M+H]+ and [M+Na]+ for each muropeptide shown in blue and purple, respectively. *Muropeptides containing G-G-anhM are denoted by an asterick.

Supplemental Table 1: Analysis of muropeptides present in 5A11 *B. burgdorferi* peptidoglycan.

Muropeptide ID	Structure	Relative % of PG	Theoretical $[M+H]^+$	Previously Identified as[1]
1	MurNAc-Ala-Glu-Orn-Gly	16.9	667.3145	Peak 1
2	GlcNAc-MurNAc-Ala-Glu-Orn-Gly	27.4	870.3938	Peak 2
3	MurNAc-Ala-Glu-Orn-[Gly]-Ala-Gly-Orn-Glu-Ala	1.7	1109.5321	NM
4	GlcNAc-MurNAc-Ala-Glu-Orn-[Gly]-Ala-Gly-Orn-Glu-Ala	<0.5	1312.6114	NM
5*	GlcNAc-GlcNAc-MurNAcAnh-Ala-Glu-Orn-Gly	0.6	1053.4470	Peak 3
6	GlcNAc-MurNAcAnh-Ala-Glu-Orn-Gly	5.4	850.3676	Peak 4 & 7
7*	GlcNAc-GlcNAc-MurNAcAnh-Ala-Glu-Orn-[Gly]-Ala-Gly-Orn-Glu-Ala	<0.5	1495.6646	NM
8	GlcNAc-MurNAcAnh-Ala-Glu-Orn-[Gly]-Ala-Gly-Orn-Glu-Ala	<0.5	1292.5852	NM
9	MurNAc-Ala-Glu-Orn-[Gly]-Ala-Gly-Orn-Glu-Ala-MurNAc	4.7	1386.6482	Peak 6
10	GlcNAc-MurNAc-Ala-Glu-Orn-[Gly]-Ala-Gly-Orn-Glu-Ala-MurNAc	3.0	1589.7276	Peak 8
11	GlcNAc-MurNAc-Ala-Glu-Orn-[Gly]-Ala-Gly-Orn-Glu-Ala-MurNAc-GlcNAc	11.7	1792.8070	Peak 9
12	GlcNAc-MurNAc-Ala-Glu-Orn-[Gly]-Ala-Gly-Orn-Glu-Ala-MurNAcAnh-GlcNAc	6.0	1772.7808	Peak 10 & 11
13*	GlcNAc-GlcNAc-MurNAcAnh-Ala-Glu-Orn-[Gly]-Ala-Gly-Orn-Glu-Ala-MurNAc-GlcNAc	0.8	1975.8601	NM
14	GlcNAc-MurNAcAnh-Ala-Glu-Orn-[Gly]-Ala-Gly-Orn-Glu-Ala-MurNAc	1.0	1569.7014	NM

15*	GlcNAc-GlcNAc-MurNAcAnh-Ala-Glu-Orn-Gly-Ala-Orn-[Gly]-Glu-Ala-MurNAcAnh-GlcNAc	<0.5	1955.8339	NM
16°	MurNAc-(Ala-Glu-Orn-Gly-Ala)-GlcNAc-MurNAc-(Ala-Glu-Orn-Gly-Ala)-GlcNAc-MurNAcAnh-(Ala-Glu-Orn-Gly)	<0.5	2492.1145	NM
17	GlcNAc-MurNAcAnh-Ala-Glu-Orn-[Gly]-Ala-Gly-Orn-Glu-Ala-MurNAcAnh-GlcNAc	<0.5	1752.7545	NM

1 – As previously identified in Jutras et. al., 2019, PNAS. NM denotes newly identified muropeptides.
* Muropeptide contains G-G-anhM.

Supplemental Table 2: Muropeptide-containing peaks from 5A11 *B. burgdorferi* peptidoglycan analyzed via LCMS.

Peak #	Muropeptide ID	$[M+H]^+$	Structure	RT (mins)
1	1	667.3145	MurNAc-Ala-Glu-Orn-Gly	1.688
2	2a	870.3939	GlcNAc-MurNAc-Ala-Glu-Orn-Gly	2.935
3	2b	870.3939	GlcNAc-MurNAc-Ala-Glu-Orn-Gly	3.342
4	3	1109.5321	MurNAc-Ala-Glu-Orn-[Gly]-Ala-Gly-Orn-Glu-Ala	6.548
5	4	1312.6115	GlcNAc-MurNAc-Ala-Glu-Orn-[Gly]-Ala-Gly-Orn-Glu-Ala	7.842
6	5*	1053.4470	GlcNAc-GlcNAc-MurNAcAnh-Ala-Glu-Orn-Gly	8.935
	6a	850.3676	GlcNAc-MurNAcAnh-Ala-Glu-Orn-Gly	
7	6b	850.3676	GlcNAc-MurNAcAnh-Ala-Glu-Orn-Gly	11.477
8	7*	1495.6646	GlcNAc-GlcNAc-MurNAcAnh-Ala-Glu-Orn-[Gly]-Ala-Gly-Orn-Glu-Ala	11.627
9	8a	1292.5853	GlcNAc-MurNAcAnh-Ala-Glu-Orn-[Gly]-Ala-Gly-Orn-Glu-Ala	11.918
	9a	1386.6482	MurNAc-Ala-Glu-Orn-[Gly]-Ala-Gly-Orn-Glu-Ala-MurNAc	
10	9b	1386.6482	MurNAc-Ala-Glu-Orn-[Gly]-Ala-Gly-Orn-Glu-Ala-MurNAc	12.652
	10a	1589.7276	GlcNAc-MurNAc-Ala-Glu-Orn-[Gly]-Ala-Gly-Orn-Glu-Ala-MurNAc	
11	10b	1589.7276	GlcNAc-MurNAc-Ala-Glu-Orn-[Gly]-Ala-Gly-Orn-Glu-Ala-MurNAc	13.302
	11	1792.8070	GlcNAc-MurNAc-Ala-Glu-Orn-[Gly]-Ala-Gly-Orn-Glu-Ala-MurNAc-GlcNAc	
12	8b	1292.5853	GlcNAc-MurNAcAnh-Ala-Glu-Orn-[Gly]-Ala-Gly-Orn-Glu-Ala	13.802
13	12a	1772.7808	GlcNAc-MurNAc-Ala-Glu-Orn-[Gly]-Ala-Gly-Orn-Glu-Ala-MurNAcAnh-GlcNAc	15.428
14	13*	1975.8601	GlcNAc-GlcNAc-MurNAcAnh-Ala-Glu-Orn-[Gly]-Ala-Gly-Orn-Glu-Ala-MurNAc-GlcNAc	15.828
15	14a	1569.7014	GlcNAc-MurNAcAnh-Ala-Glu-Orn-[Gly]-Ala-Gly-Orn-Glu-Ala-MurNAc	15.962
16	12b	1772.7808	GlcNAc-MurNAc-Ala-Glu-Orn-[Gly]-Ala-Gly-Orn-Glu-Ala-MurNAcAnh-GlcNAc	16.433
17	14b	1569.7014	GlcNAc-MurNAcAnh-Ala-Glu-Orn-[Gly]-Ala-Gly-Orn-Glu-Ala-MurNAc	17.478

18	14c	1569.7014	GlcNAc-MurNAcAnh-Ala-Glu-Orn-[Gly]-Ala-Gly-Orn-Glu-Ala-MurNAc	17.803
	12c	1772.7808	GlcNAc-MurNAc-Ala-Glu-Orn-[Gly]-Ala-Gly-Orn-Glu-Ala-MurNAcAnh-GlcNAc	
19	15a*	1955.8339	GlcNAc-GlcNAc-MurNAcAnh-Ala-Glu-Orn-Gly-Ala-Orn-[Gly]-Glu-Ala-MurNAcAnh-GlcNAc	18.490
20	16a	2492.1145	MurNAc-(Ala-Glu-Orn-Gly-Ala)-GlcNAc-MurNAc-(Ala-Glu-Orn-Gly-Ala)-GlcNAc-MurNAcAnh-(Ala-Glu-Orn-Gly)	19.043
21	17a	1752.7546	GlcNAc-MurNAcAnh-Ala-Glu-Orn-[Gly]-Ala-Gly-Orn-Glu-Ala-MurNAcAnh-GlcNAc	19.277
22	15b*	1955.8339	GlcNAc-GlcNAc-MurNAcAnh-Ala-Glu-Orn-Gly-Ala-Orn-[Gly]-Glu-Ala-MurNAcAnh-GlcNAc	19.717
23	16b	2492.1145	MurNAc-(Ala-Glu-Orn-Gly-Ala)-GlcNAc-MurNAc-(Ala-Glu-Orn-Gly-Ala)-GlcNAc-MurNAcAnh-(Ala-Glu-Orn-Gly)	20.265
24	17b	1752.7546	GlcNAc-MurNAcAnh-Ala-Glu-Orn-[Gly]-Ala-Gly-Orn-Glu-Ala-MurNAcAnh-GlcNAc	20.523
25	17c	1752.7546	GlcNAc-MurNAcAnh-Ala-Glu-Orn-[Gly]-Ala-Gly-Orn-Glu-Ala-MurNAcAnh-GlcNAc	21.905

* Muropeptide contains G-G-anhM

Supplemental Table 3: Theoretical vs. observed *m/z* for each muropeptide after mass correction using an internal standard.

Muropeptide	Molecular formula	Observed Ion	Theoretical *m/z*	Observed *m/z*	Difference (Da)
1	$C_{26}H_{46}N_6O_{14}$	$[M+H]^+$	667.3145	667.3115	0.0030
2	$C_{34}H_{59}N_7O_{19}$	$[M+H]^+$	870.3938	870.3939	-0.0001
3	$C_{44}H_{76}N_{12}O_{21}$	$[M+2H]^{+2}$	555.2697	555.2676	0.0021
4	$C_{52}H_{89}N_{13}O_{26}$	$[M+2H]^{+2}$	656.8094	656.8069	0.0025
5*	$C_{42}H_{68}N_8O_{23}$	$[M+H]^+$	1053.4470	1053.4425	0.0045
6	$C_{34}H_{55}N_7O_{18}$	$[M+H]^+$	850.3676	850.3639	0.0037
7*	$C_{60}H_{98}N_{14}O_{30}$	$[M+2H]^{+2}$	748.3359	748.3331	0.0028
8	$C_{52}H_{85}N_{13}O_{25}$	$[M+2H]^{+2}$	646.7963	646.7936	0.0027
9	$C_{55}H_{95}N_{13}O_{28}$	$[M+2H]^{+2}$	693.8278	693.8250	0.0028
10	$C_{63}H_{108}N_{14}O_{33}$	$[M+2H]^{+2}$	795.3674	795.3644	0.0030
11	$C_{71}H_{121}N_{15}O_{38}$	$[M+2H]^{+2}$	896.9071	896.9034	0.0037
12	$C_{71}H_{117}N_{15}O_{37}$	$[M+2H]^{+2}$	886.8940	886.8902	0.0038
13*	$C_{79}H_{130}N_{16}O_{42}$	$[M+2H]^{+2}$	988.4337	988.4299	0.0038
14	$C_{63}H_{104}N_{14}O_{32}$	$[M+2H]^{+2}$	785.3543	785.3512	0.0031
15*	$C_{79}H_{126}N_{16}O_{41}$	$[M+2H]^{+2}$	978.4206	978.4168	0.0038
16	$C_{100}H_{166}N_{22}O_{51}$	$[M+2H]^{+2}$	1246.5609	1246.5564	0.0045
17	$C_{71}H_{113}N_{15}O_{36}$	$[M+2H]^{+2}$	876.8809	876.8779	0.0030

* Muropeptide contains G-G-anhM.

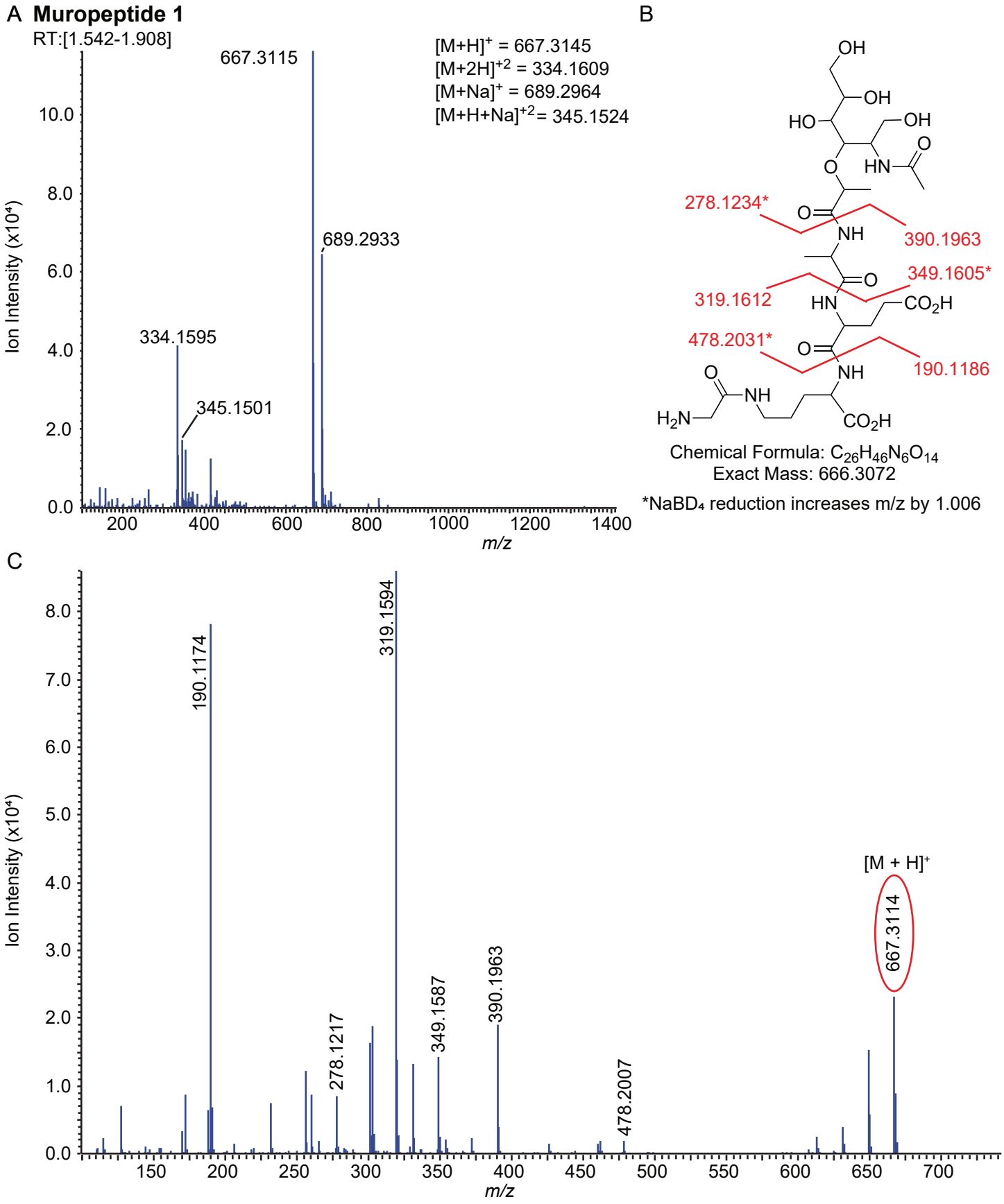

Supplemental Figure 3: (A) MS1 spectra generated from scanning retention times of 1.542-1.908 minutes. (B) The structure of muropeptide 1. Cleavages with resulting *m/z* fragments are shown in red. (C) MS2 obtained from targeting precursor ion 667.3145 $[M+H]^+$. Red fragments generated in B correspond to observed MS2 fragments in C.

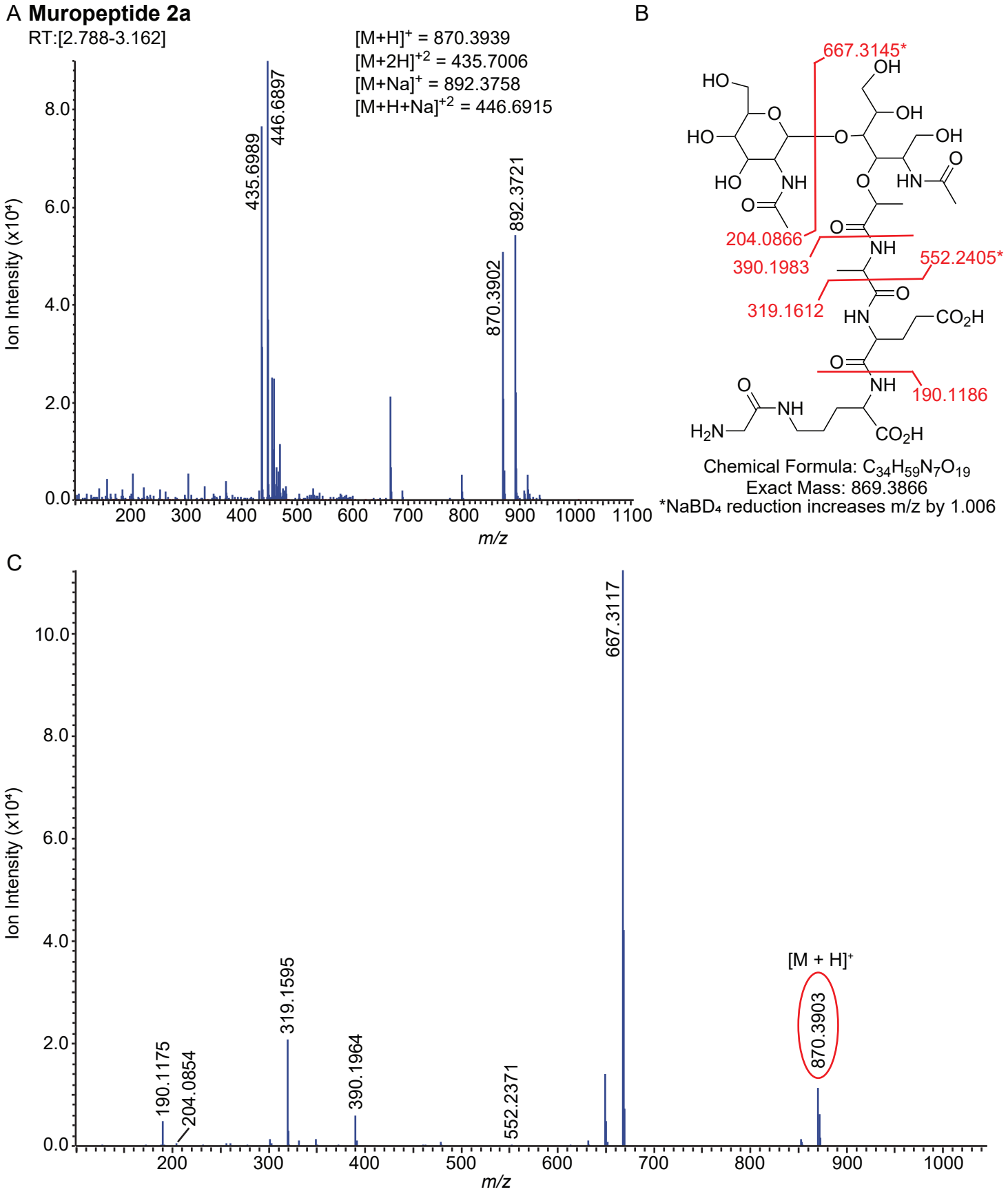

Supplemental Figure 4: (A) MS1 spectra generated from scanning retention times of 2.788-3.162 minutes. (B) The structure of muropeptide 2a. Cleavages with resulting *m/z* fragments are shown in red. (C) MS2 obtained from targeting precursor ion 870.3902 $[M+H]^+$. Red fragments generated in B correspond to observed MS2 fragments in C.

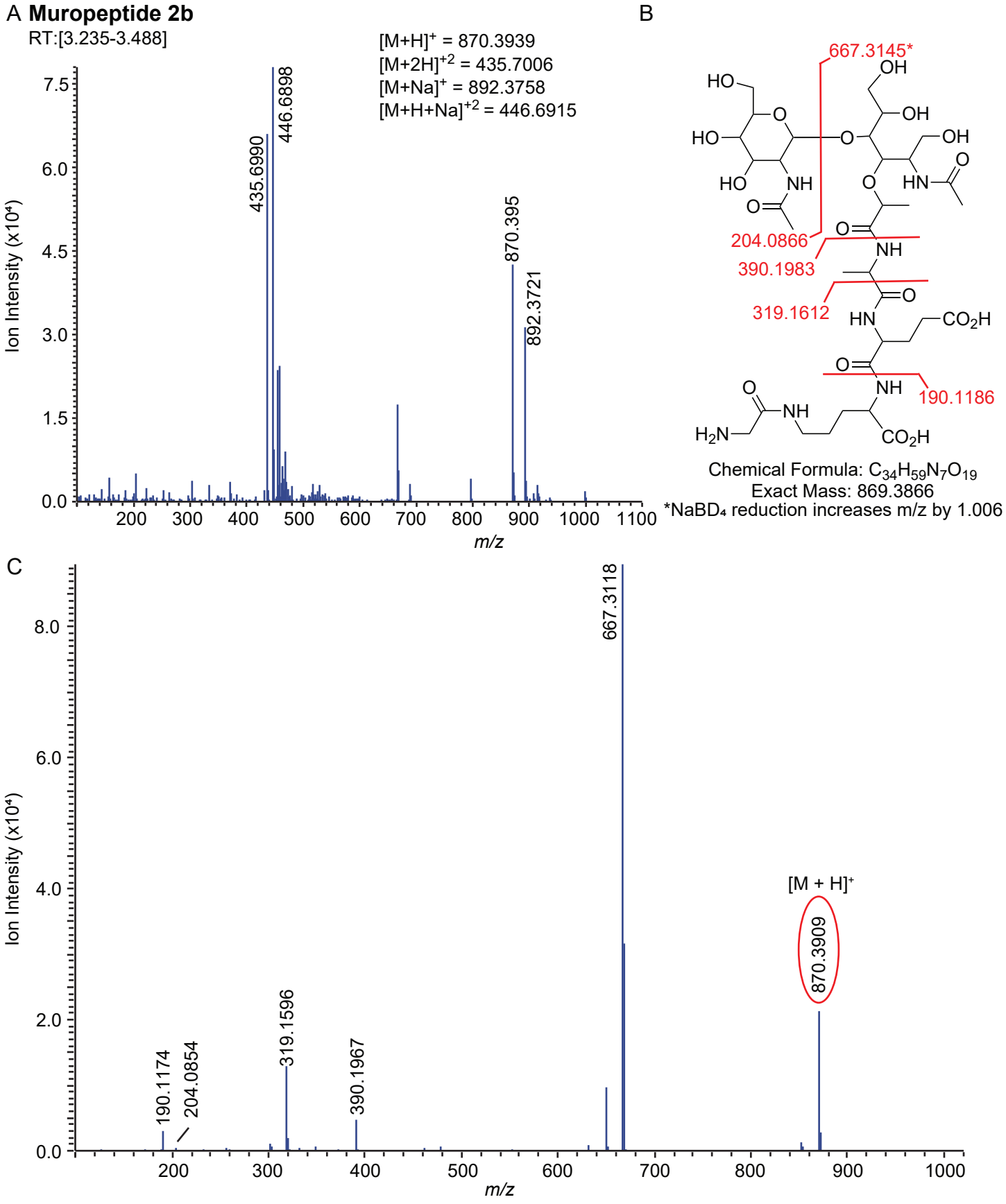

Supplemental Figure 5: (A) MS1 spectra generated from scanning retention times of 3.235-3.488 minutes. (B) The structure of muropeptide 2b. Cleavages with resulting *m/z* fragments are shown in red. (C) MS2 obtained from targeting precursor ion 870.3902 $[M+H]^+$. Red fragments generated in B correspond to observed MS2 fragments in C.

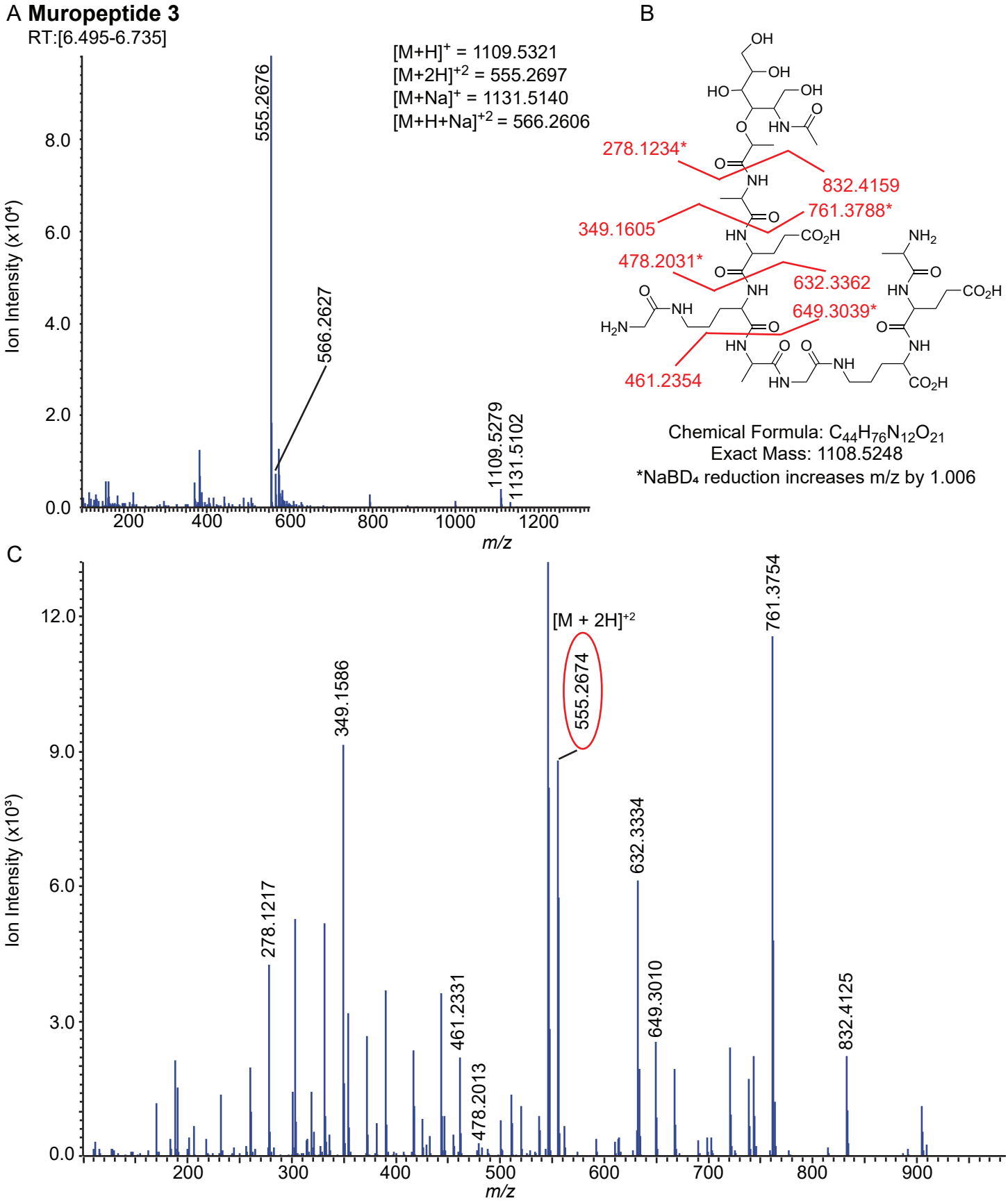

Supplemental Figure 6: (A) MS1 spectra generated from scanning retention times of 6.495-6.735 minutes. (B) The structure of muropeptide 3. Cleavages with resulting *m/z* fragments are shown in red. (C) MS2 obtained from targeting precursor ion 555.2676 $[M+2H]^{+2}$. Red fragments generated in B correspond to observed MS2 fragments in C.

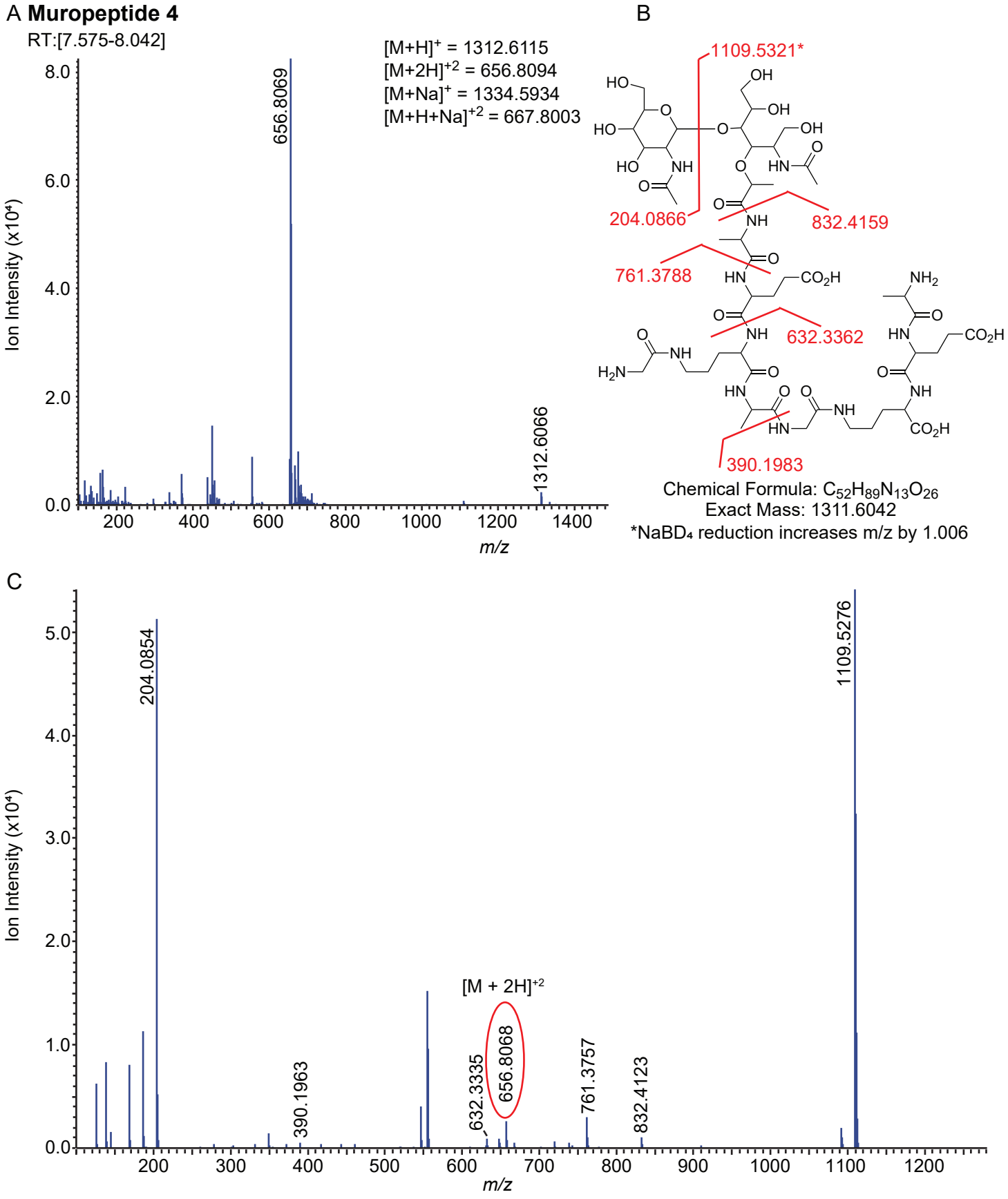

Supplemental Figure 7: (A) MS1 spectra generated from scanning retention times of 7.575-8.042 minutes. (B) The structure of muropeptide 4. Cleavages with resulting *m/z* fragments are shown in red. (C) MS2 obtained from targeting precursor ion 656.8094 $[M+2H]^{+2}$. Red fragments generated in B correspond to observed MS2 fragments in C.

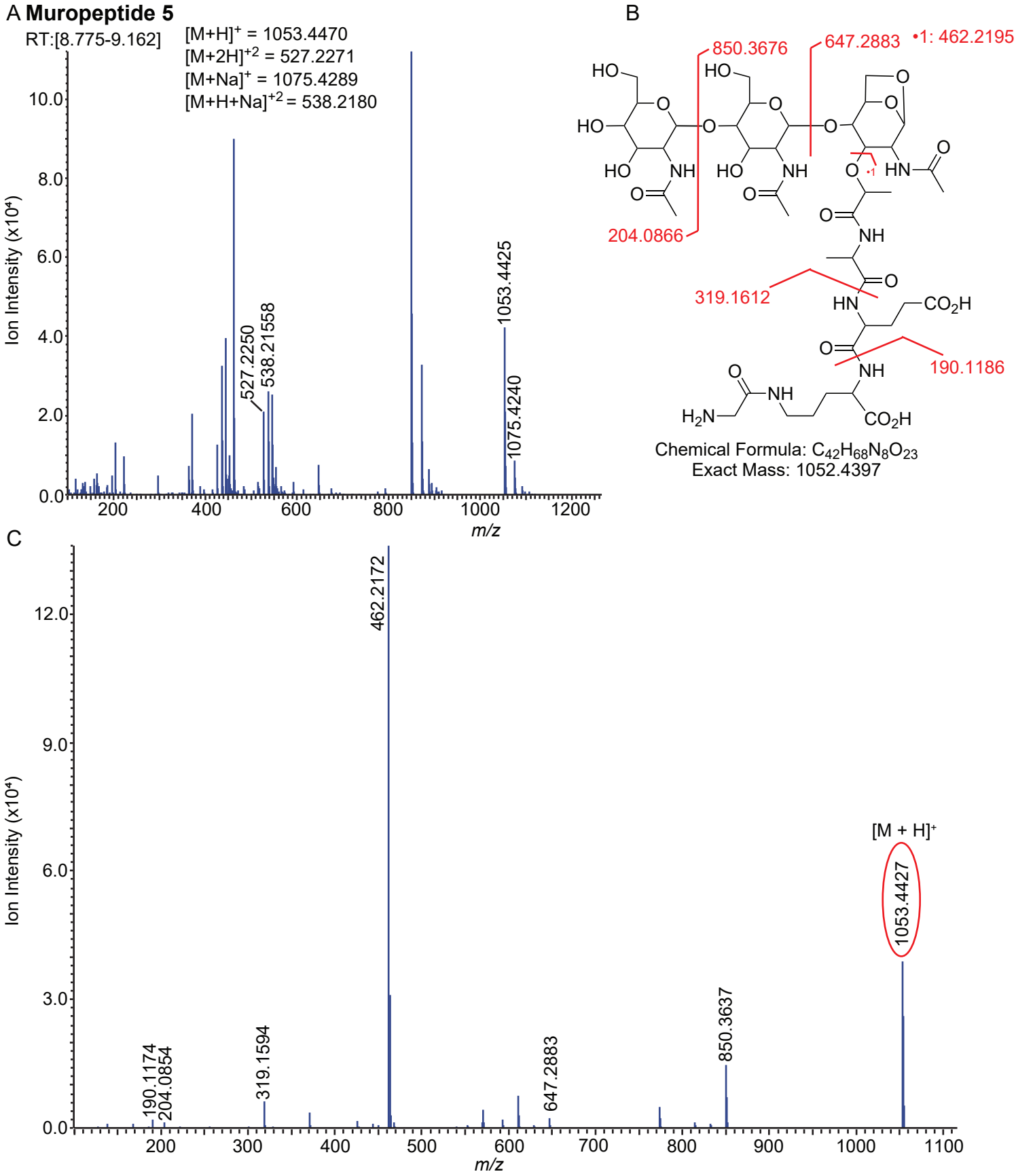

Supplemental Figure 8: (A) MS1 spectra generated from scanning retention times of 8.775-9.162 minutes. (B) The structure of muropeptide 5. Cleavages with resulting *m/z* fragments are shown in red. (C) MS2 obtained from targeting precursor ion 1053.4426 $[M+H]^+$. Red fragments generated in B correspond to observed MS2 fragments in C.

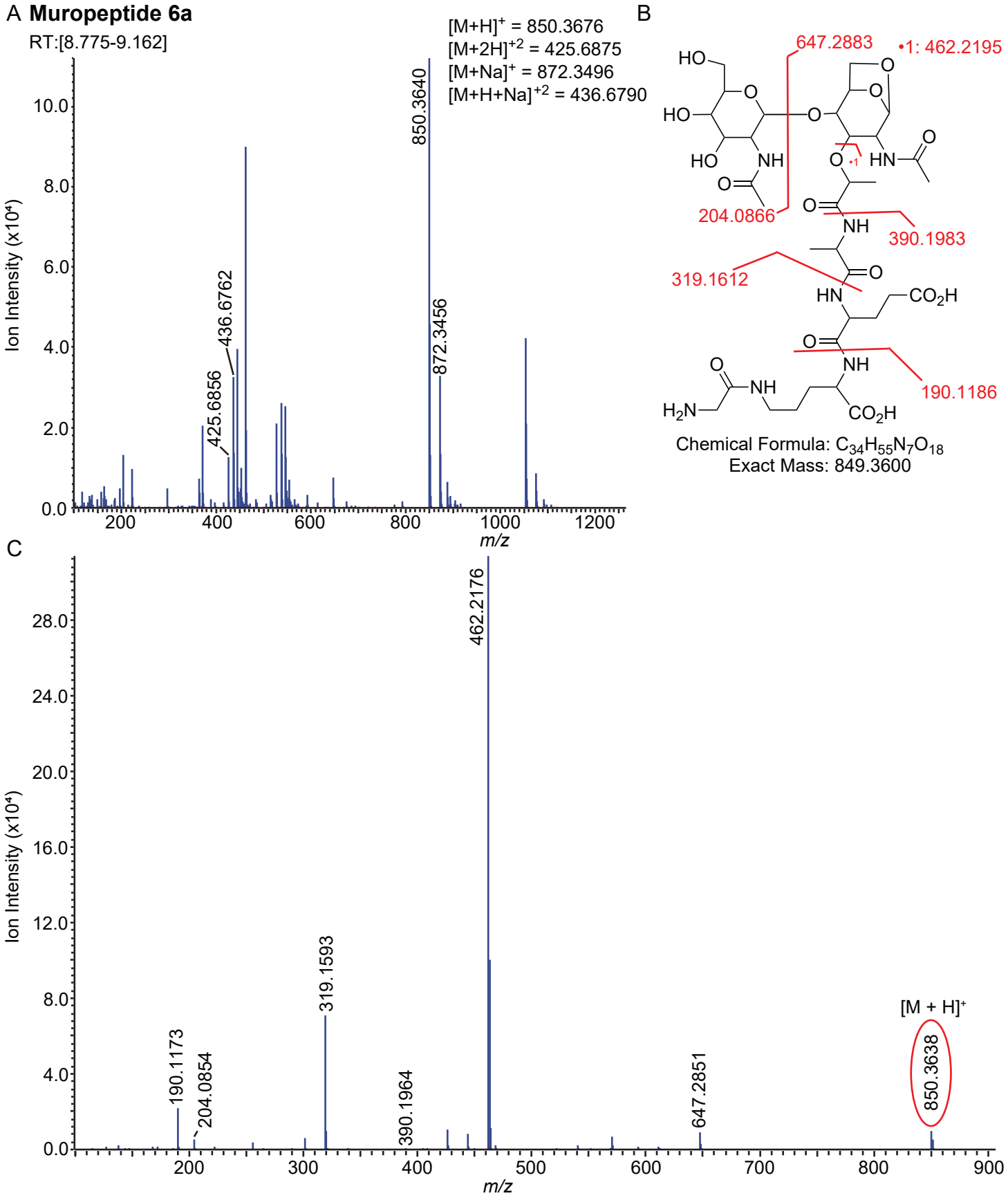

Supplemental Figure 9: (A) MS1 spectra generated from scanning retention times of 8.775-9.162 minutes. (B) The structure of muropeptide 6a. Cleavages with resulting *m/z* fragments are shown in red. (C) MS2 obtained from targeting precursor ion 850.3676 $[M+H]^+$. Red fragments generated in B correspond to observed MS2 fragments in C.

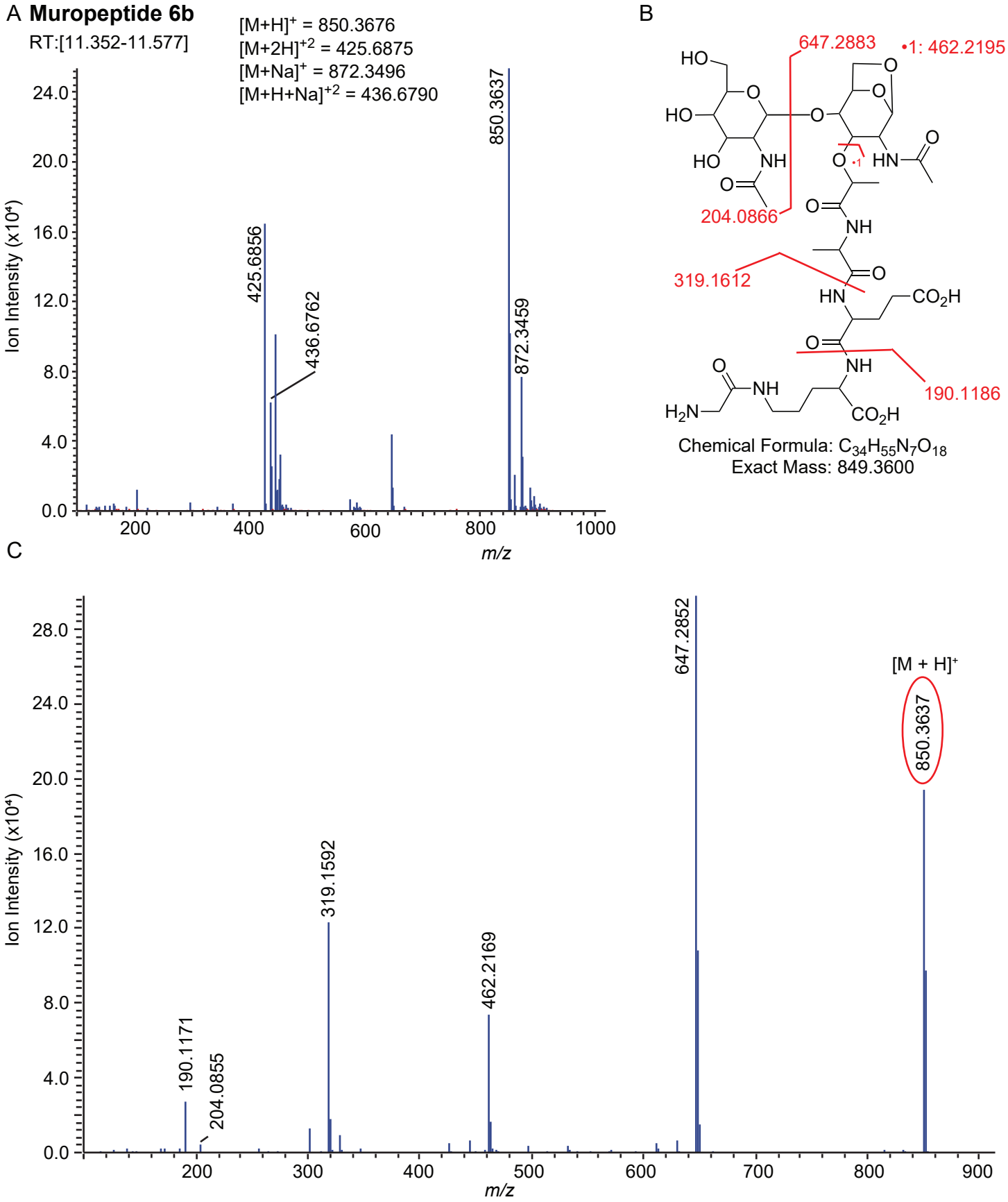

Supplemental Figure 10: (A) MS1 spectra generated from scanning retention times of 11.352-11.577 minutes. (B) The structure of muropeptide 6b. Cleavages with resulting *m/z* fragments are shown in red. (C) MS2 obtained from targeting precursor ion 850.3676 $[M+H]^+$. Red fragments generated in B correspond to observed MS2 fragments in C.

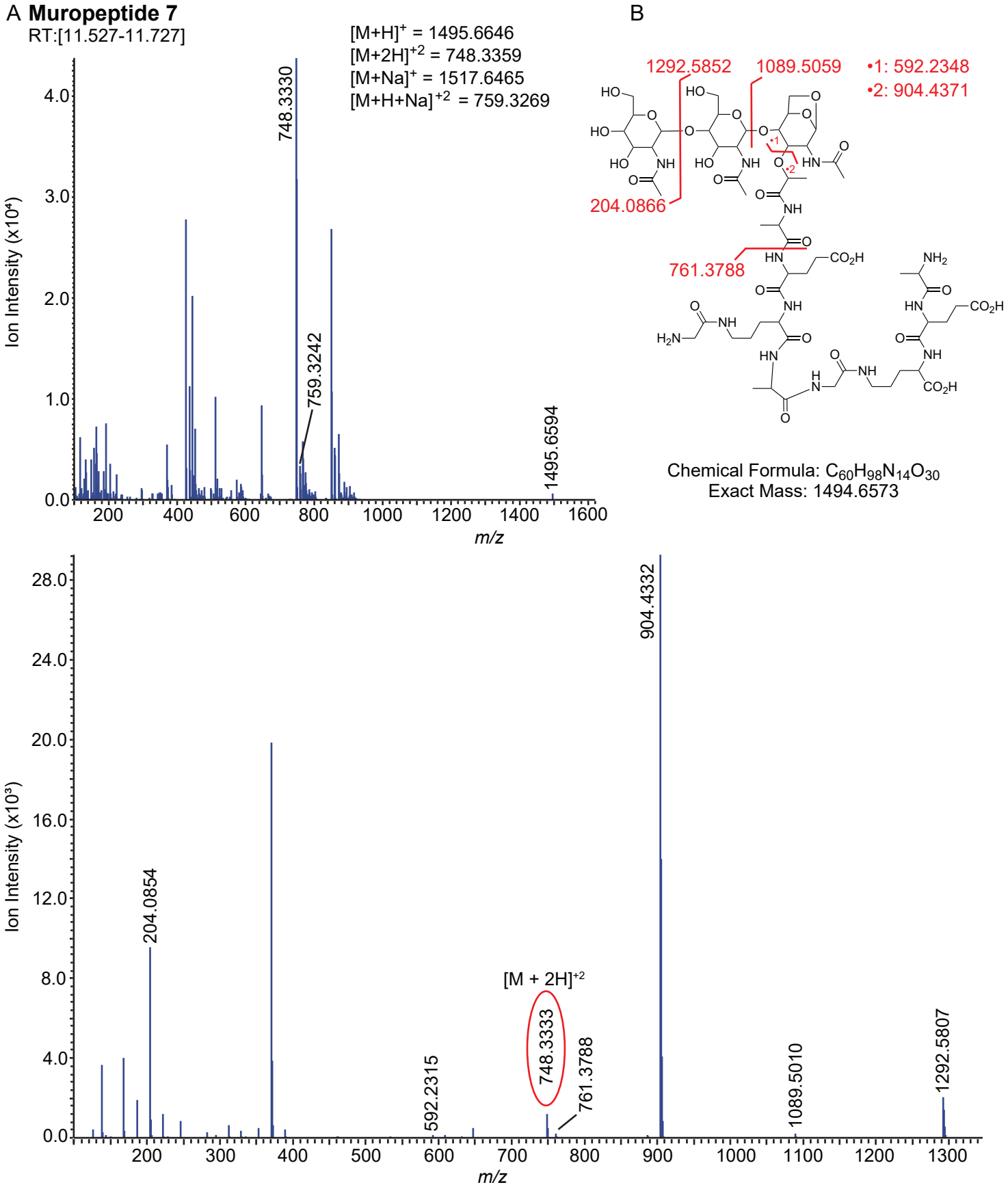

Supplemental Figure 11: (A) MS1 spectra generated from scanning retention times of 11.527-11.727 minutes. (B) The structure of muropeptide 7. Cleavages with resulting *m/z* fragments are shown in red. (C) MS2 obtained from targeting precursor ion 748.3359 $[M+2H]^{+2}$. Red fragments generated in B correspond to observed MS2 fragments in C.

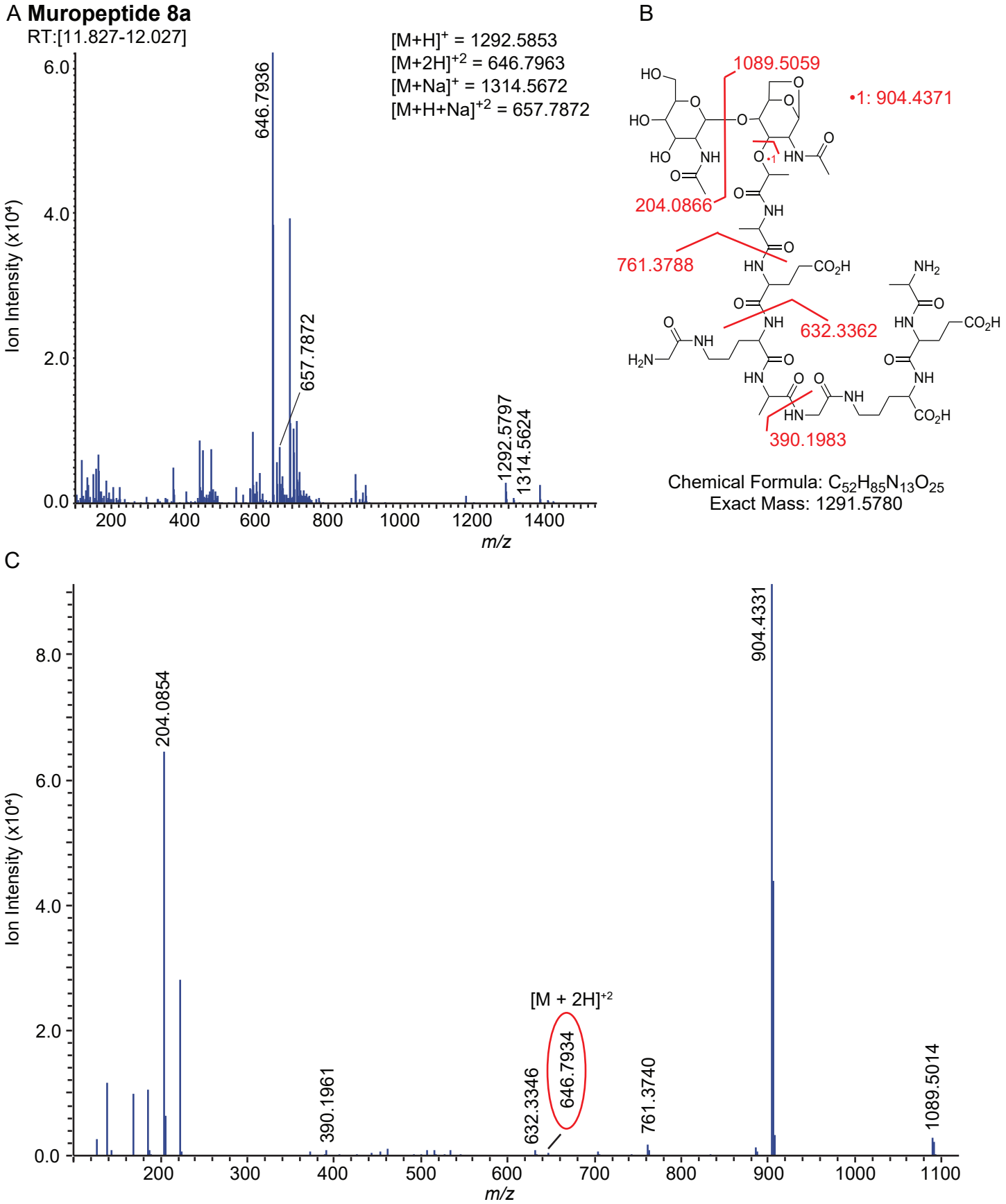

Supplemental Figure 12: (A) MS1 spectra generated from scanning retention times of 11.827-12.027 minutes. (B) The structure of muropeptide 8a. Cleavages with resulting *m/z* fragments are shown in red. (C) MS2 obtained from targeting precursor ion 646.7963 $[M+2H]^{+2}$. Red fragments generated in B correspond to observed MS2 fragments in C.

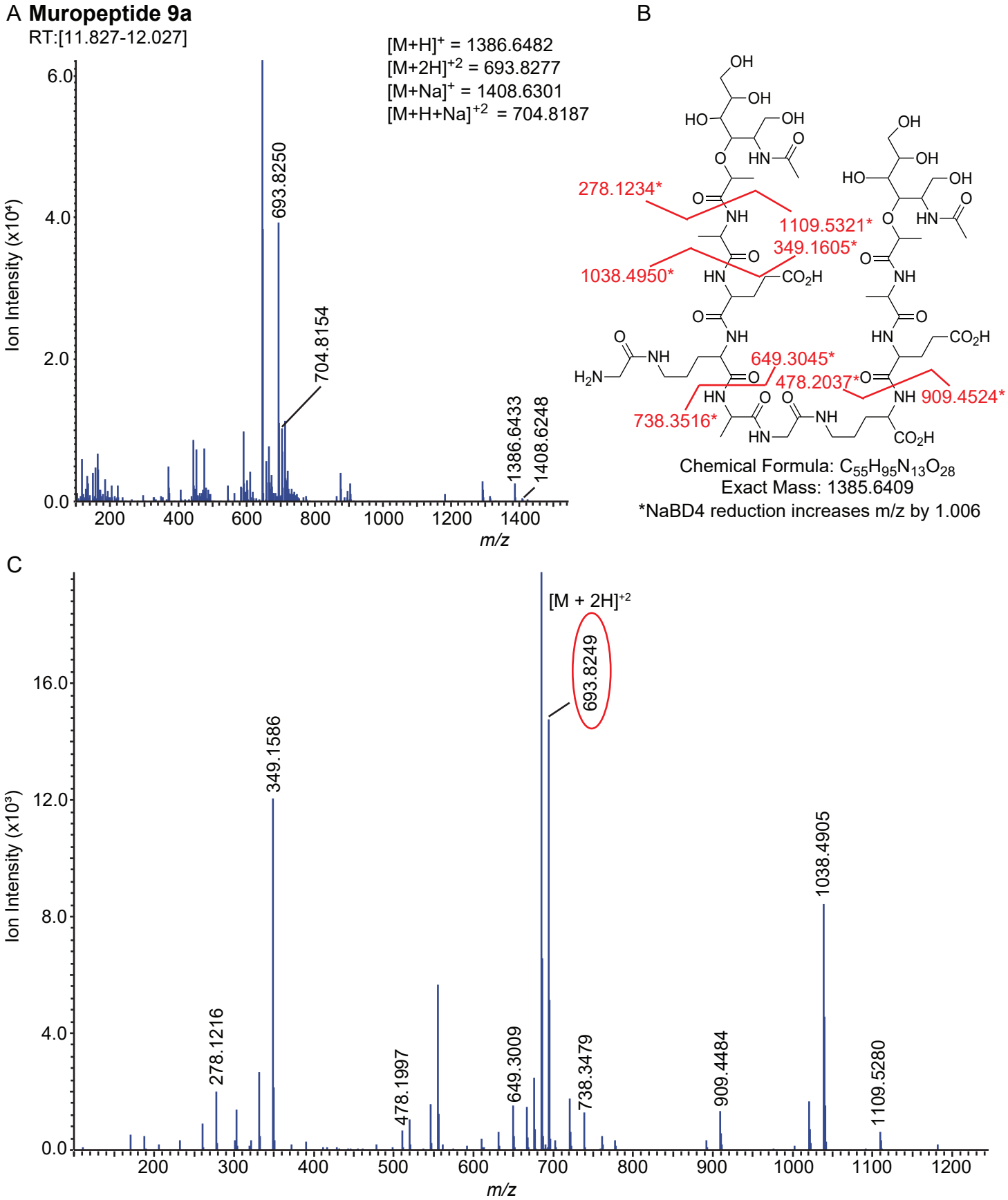

Supplemental Figure 13: (A) MS1 spectra generated from scanning retention times of 11.827-12.027 minutes. (B) The structure of muropeptide 9a. Cleavages with resulting *m/z* fragments are shown in red. (C) MS2 obtained from targeting precursor ion 693.8277 $[M+2H]^{+2}$. Red fragments generated in B correspond to observed MS2 fragments in C.

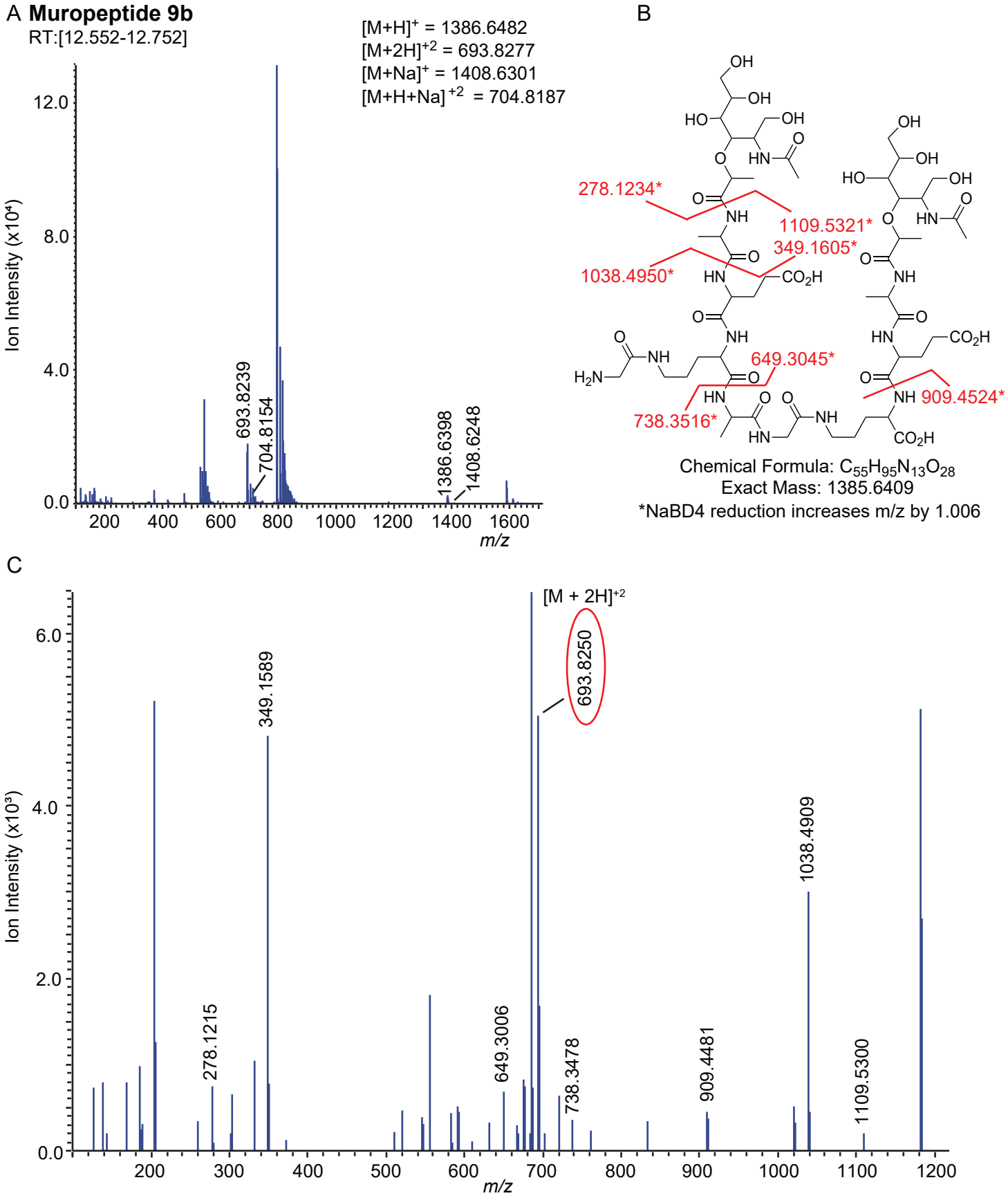

Supplemental Figure 14: (A) MS1 spectra generated from scanning retention times of 12.552-12.752 minutes. (B) The structure of muropeptide 9b. Cleavages with resulting *m/z* fragments are shown in red. (C) MS2 obtained from targeting precursor ion 693.8277 $[M+2H]^{+2}$. Red fragments generated in B correspond to observed MS2 fragments in C.

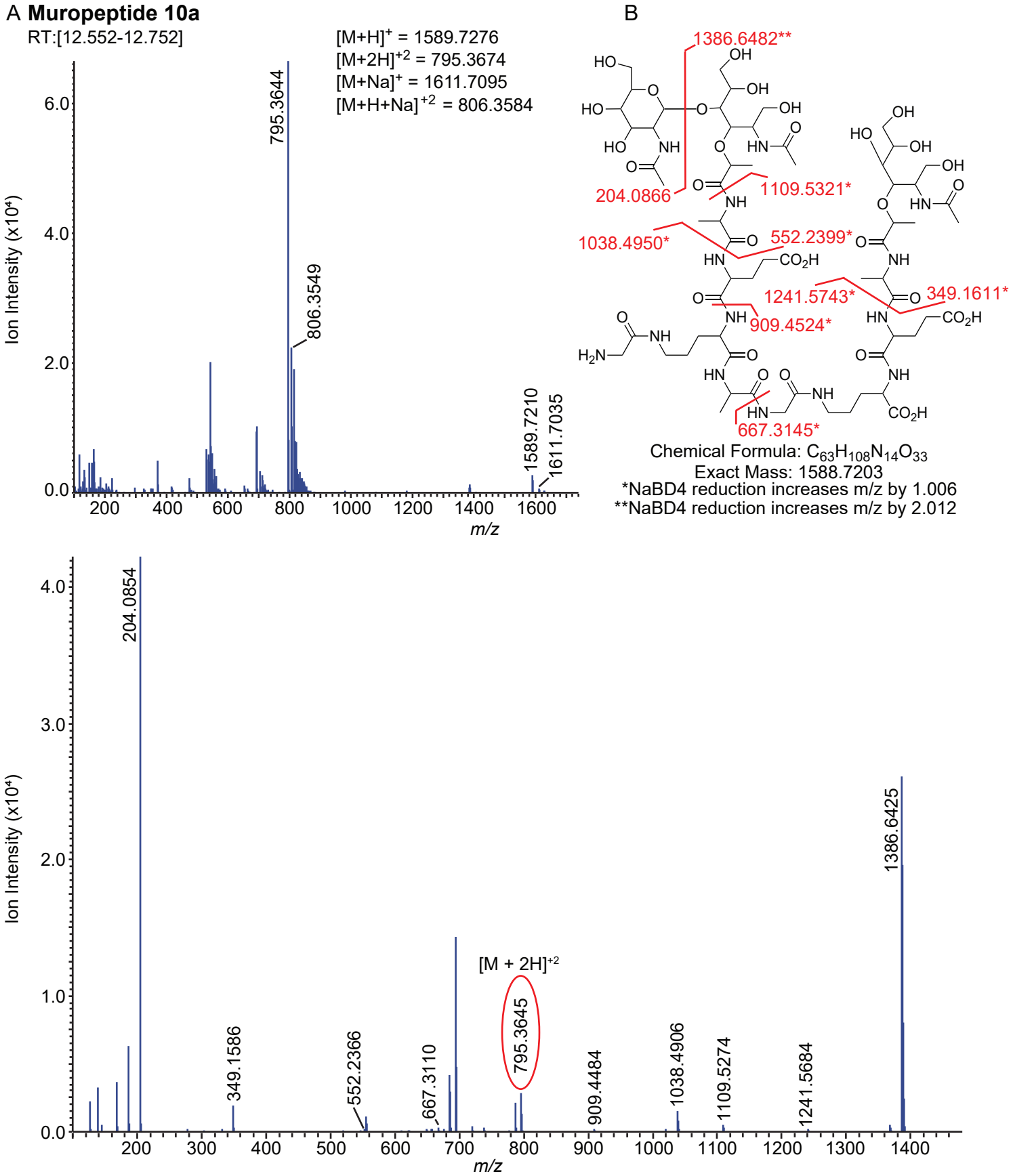

Supplemental Figure 15: (A) MS1 spectra generated from scanning retention times of 12.552-12.752 minutes. (B) The structure of muropeptide 10a. Cleavages with resulting *m/z* fragments are shown in red. (C) MS2 obtained from targeting precursor ion 795.3674 $[M+2H]^{+2}$. Red fragments generated in B correspond to observed MS2 fragments in C.

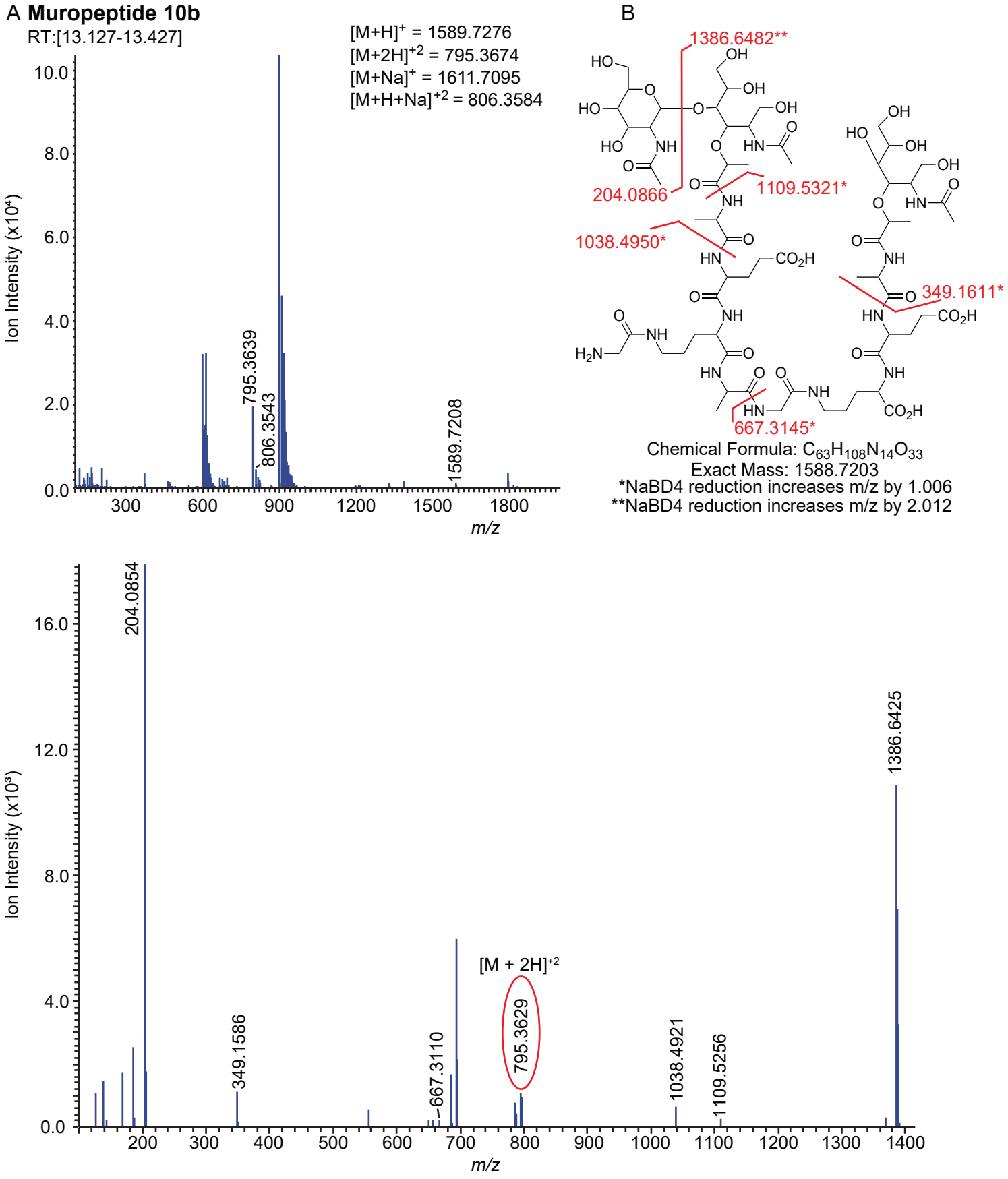

Supplemental Figure 16: (A) MS1 spectra generated from scanning retention times of 13.127-13.427 minutes. (B) The structure of muropeptide 10b. Cleavages with resulting *m/z* fragments are shown in red. (C) MS2 obtained from targeting precursor ion 795.3674 $[M+2H]^{+2}$. Red fragments generated in B correspond to observed MS2 fragments in C.

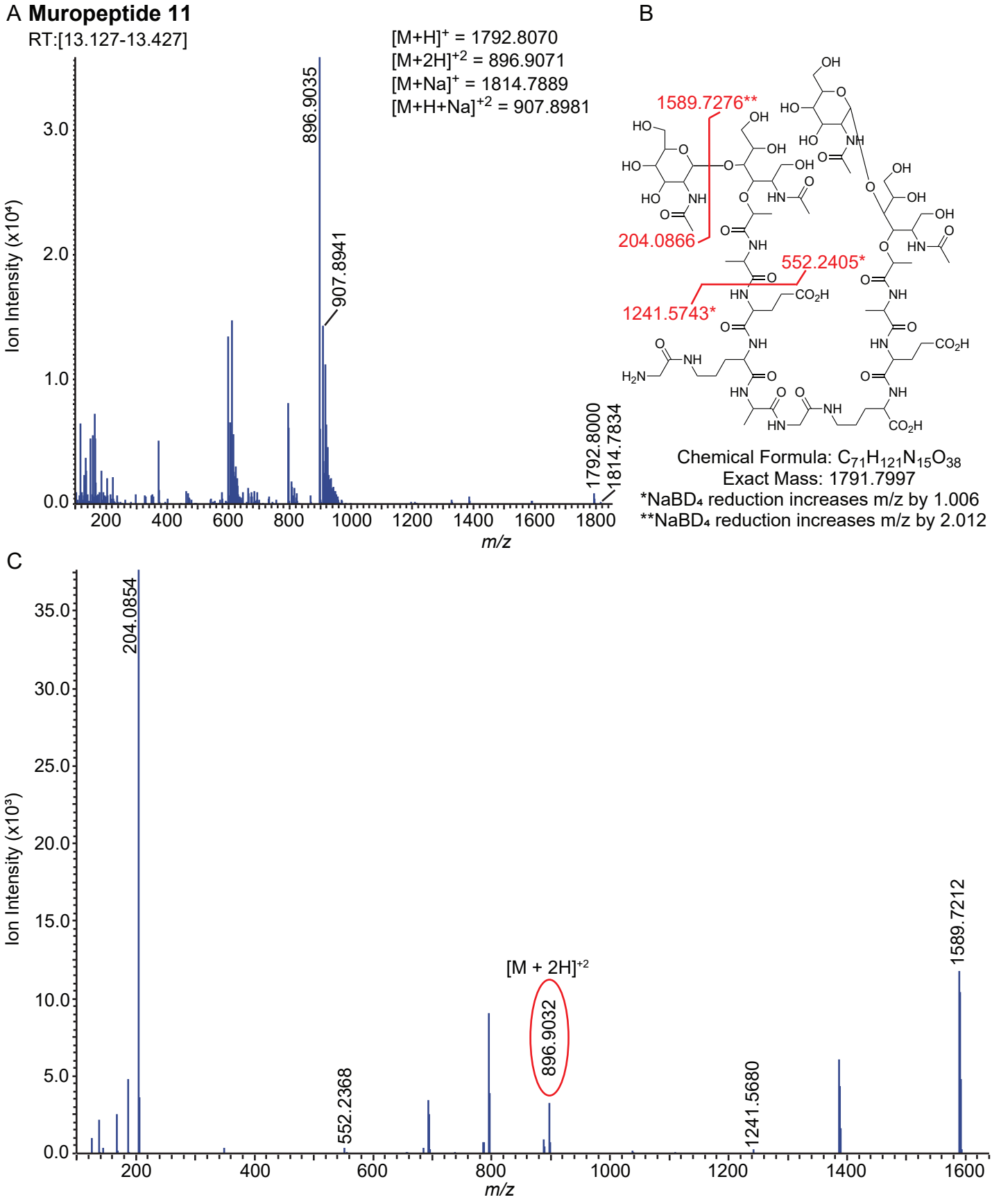

Supplemental Figure 17: (A) MS1 spectra generated from scanning retention times of 13.127-13.427 minutes. (B) The structure of muropeptide 11. Cleavages with resulting *m/z* fragments are shown in red. (C) MS2 obtained from targeting precursor ion 896.9035 $[M+H]^{+2}$. Red fragments generated in B correspond to observed MS2 fragments in C.

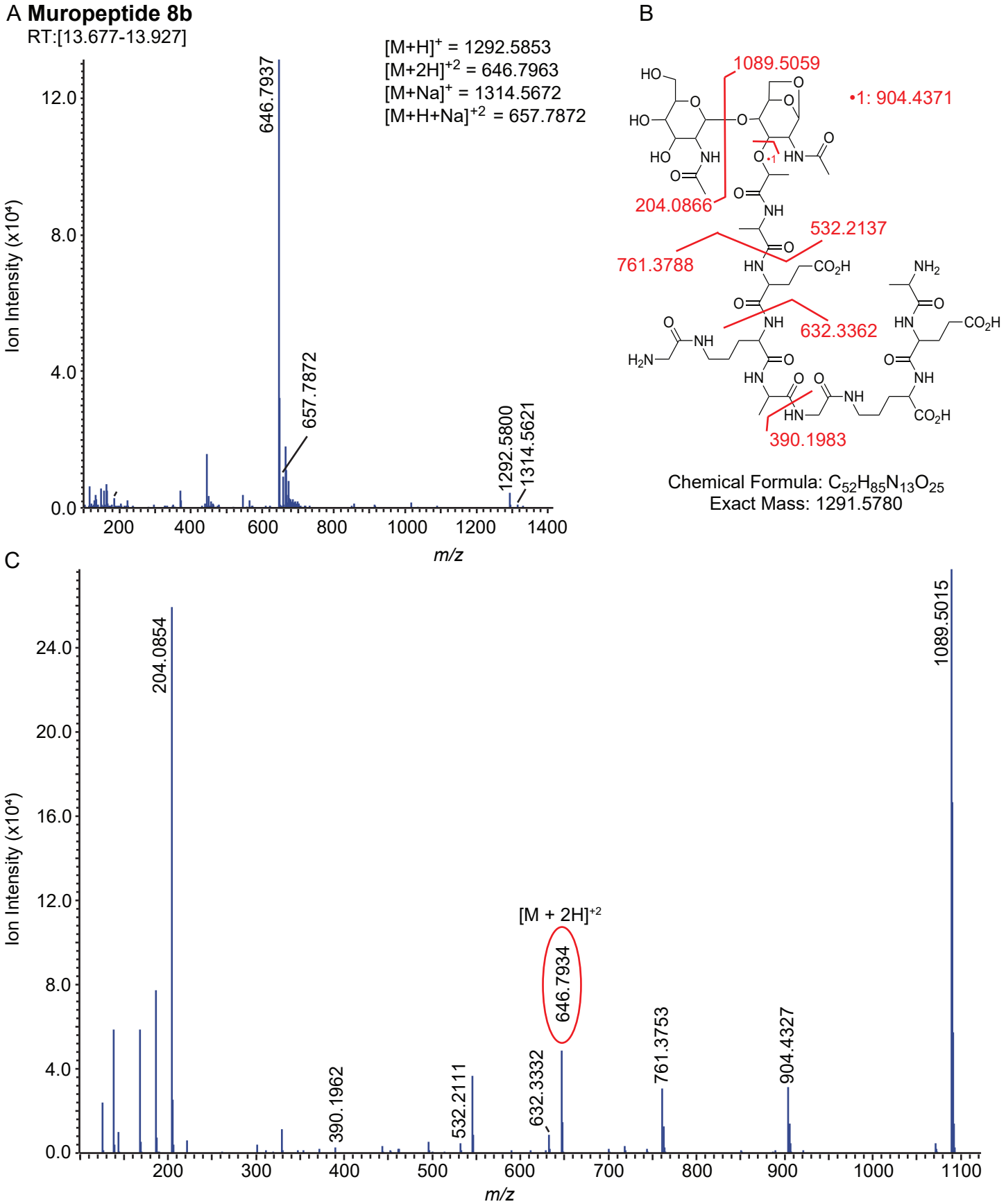

Supplemental Figure 18: (A) MS1 spectra generated from scanning retention times of 13.667-13.927 minutes. (B) The structure of muropeptide 8b. Cleavages with resulting *m/z* fragments are shown in red. (C) MS2 obtained from targeting precursor ion 646.7963 $[M+2H]^{+2}$. Red fragments generated in B correspond to observed MS2 fragments in C.

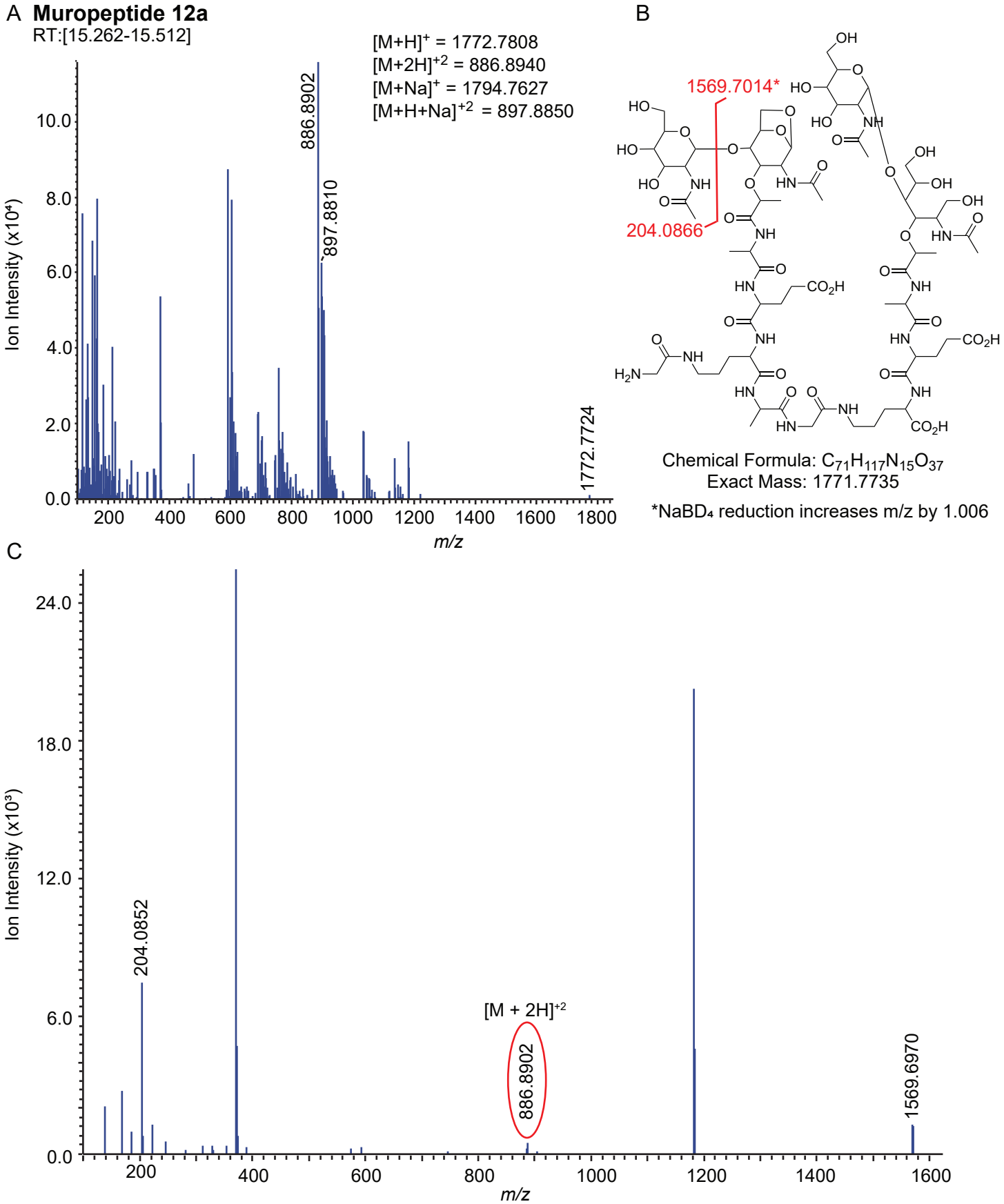

Supplemental Figure 19: (A) MS1 spectra generated from scanning retention times of 15.262-15.512 minutes. (B) The structure of muropeptide 12a. Cleavages with resulting *m/z* fragments are shown in red. (C) MS2 obtained from targeting precursor ion 886.8902 $[M+H]^{+2}$. Red fragments generated in B correspond to observed MS2 fragments in C.

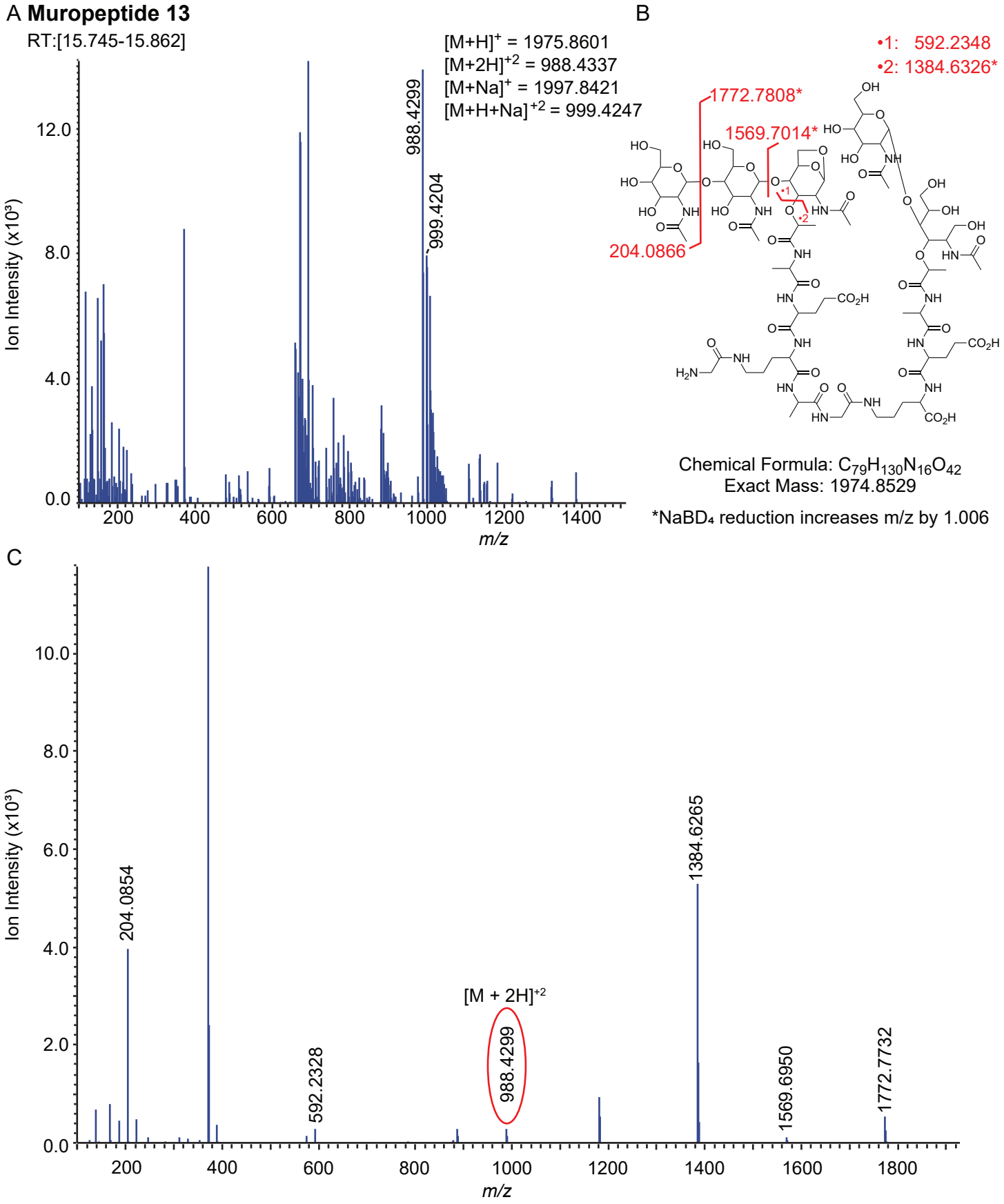

Supplemental Figure 20: (A) MS1 spectra generated from scanning retention times of 15.745-15.862 minutes. (B) The structure of muropeptide 13. Cleavages with resulting *m/z* fragments are shown in red. (C) MS2 obtained from targeting precursor ion 988.4299 $[M+H]^{+2}$. Red fragments generated in B correspond to observed MS2 fragments in C.

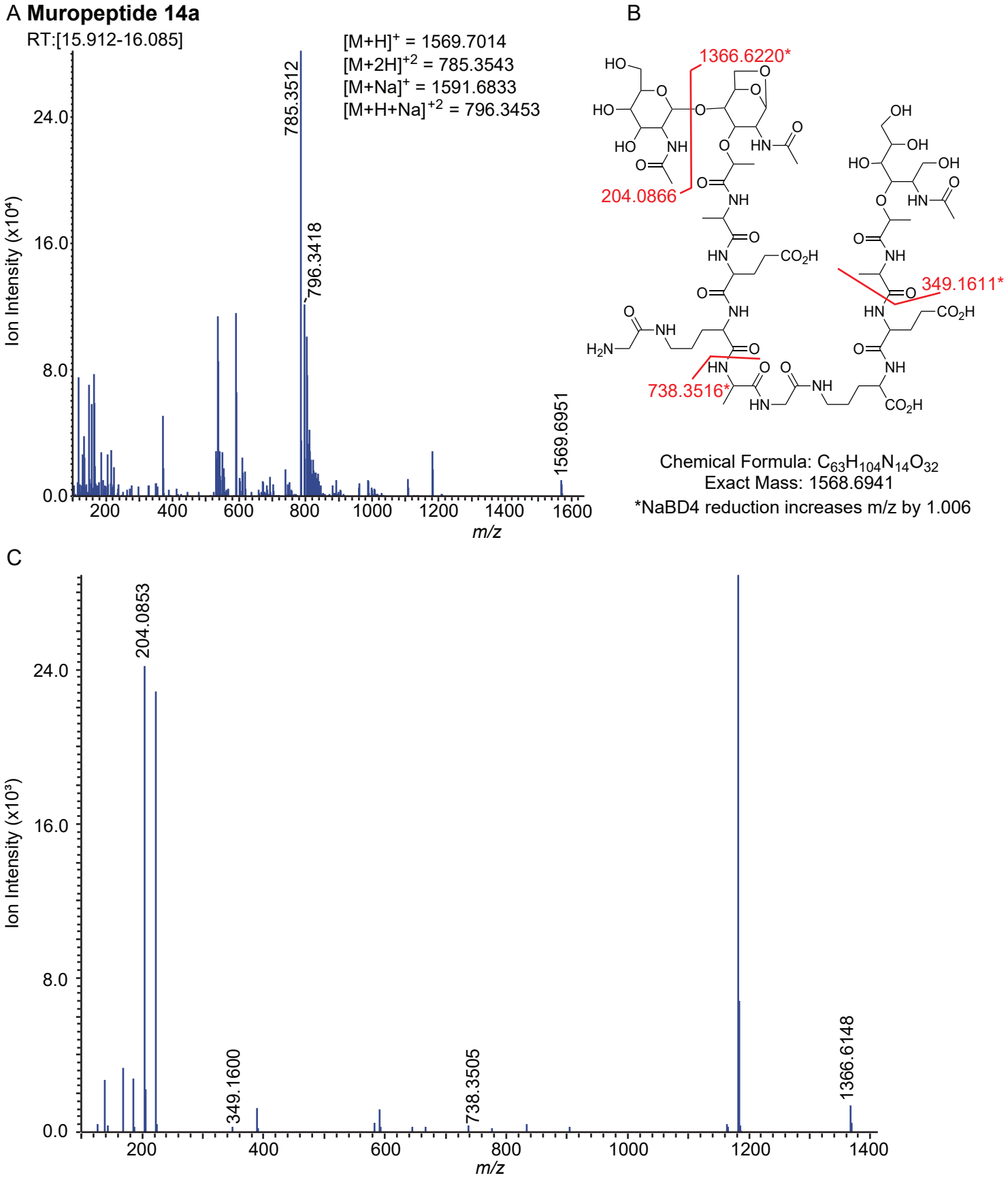

Supplemental Figure 21: (A) MS1 spectra generated from scanning retention times of 15.912-16.085 minutes. (B) The structure of muropeptide 14a. Cleavages with resulting *m/z* fragments are shown in red. (C) MS2 obtained from targeting precursor ion 785.3512 $[M+H]^{+2}$. Red fragments generated in B correspond to observed MS2 fragments in C.

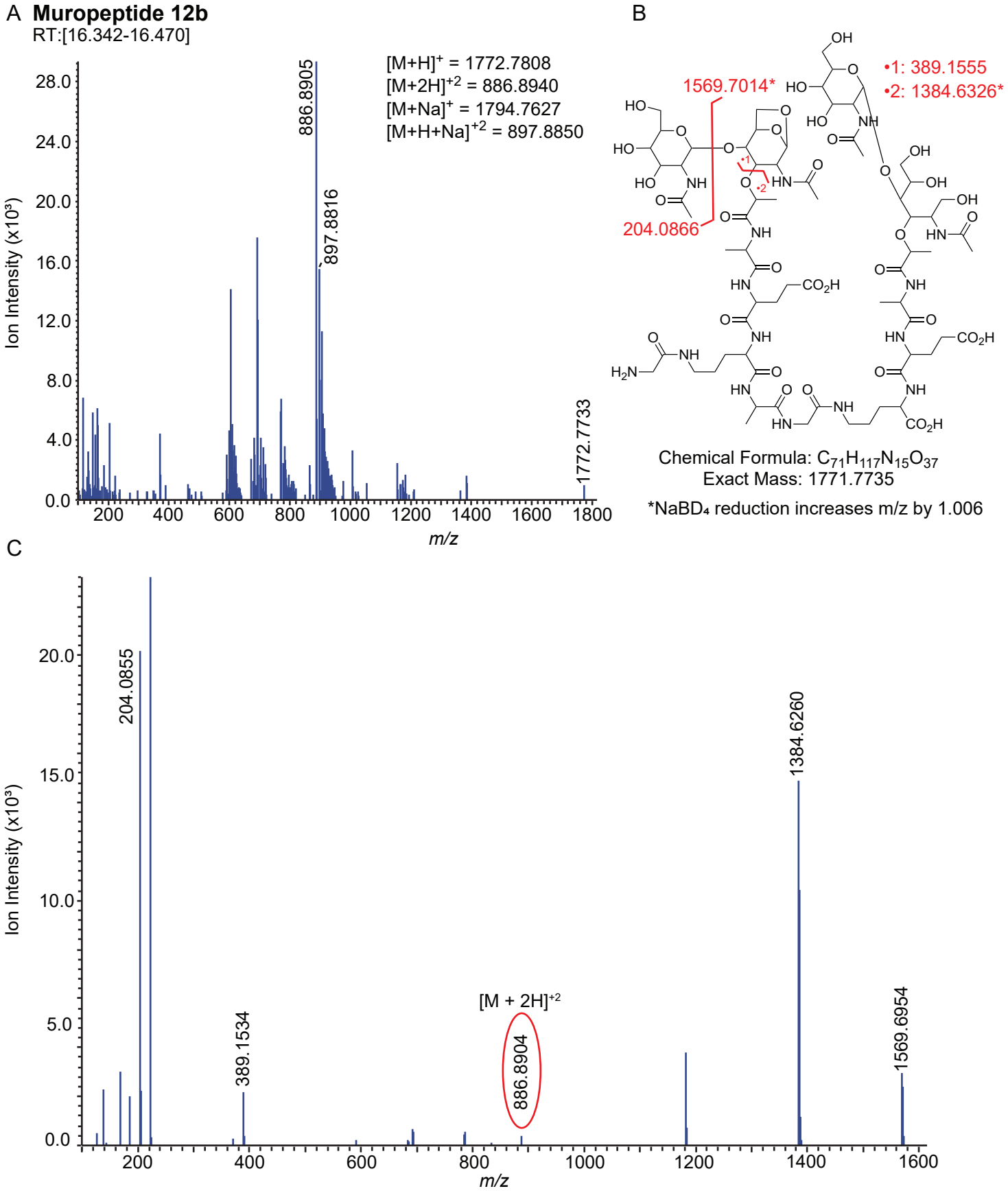

Supplemental Figure 22: (A) MS1 spectra generated from scanning retention times of 16.342-16.470 minutes. (B) The structure of muropeptide 12b. Cleavages with resulting *m/z* fragments are shown in red. (C) MS2 obtained from targeting precursor ion 886.8902 $[M+H]^{+2}$. Red fragments generated in B correspond to observed MS2 fragments in C.

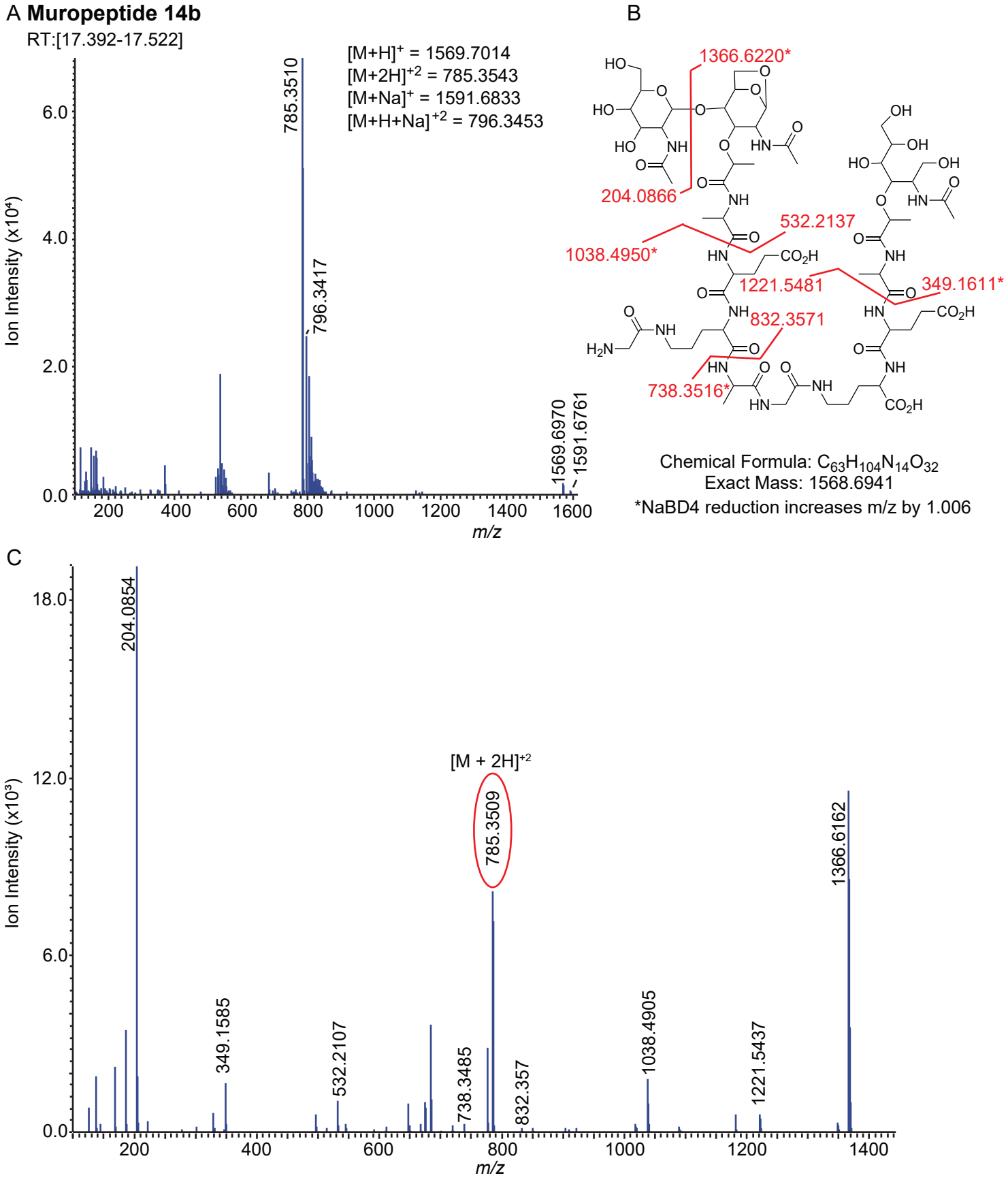

Supplemental Figure 23: (A) MS1 spectra generated from scanning retention times of 17.392-17.522 minutes. (B) The structure of muropeptide 14b. Cleavages with resulting *m/z* fragments are shown in red. (C) MS2 obtained from targeting precursor ion 785.3512 $[M+H]^{+2}$. Red fragments generated in B correspond to observed MS2 fragments in C.

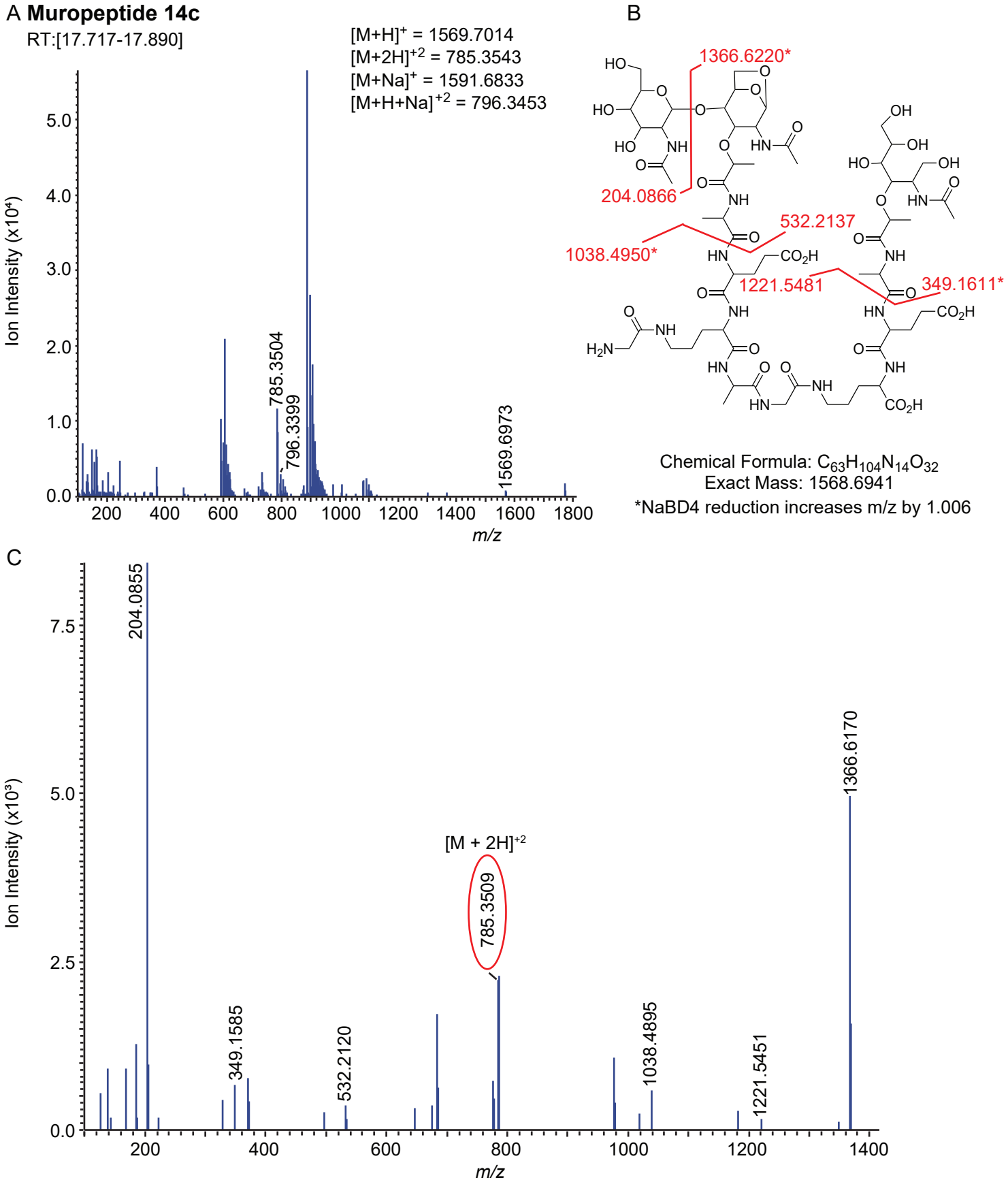

Supplemental Figure 24: (A) MS1 spectra generated from scanning retention times of 17.717-17.890 minutes. (B) The structure of muropeptide 14c. Cleavages with resulting *m/z* fragments are shown in red. (C) MS2 obtained from targeting precursor ion 785.3512 $[M+H]^{+2}$. Red fragments generated in B correspond to observed MS2 fragments in C.

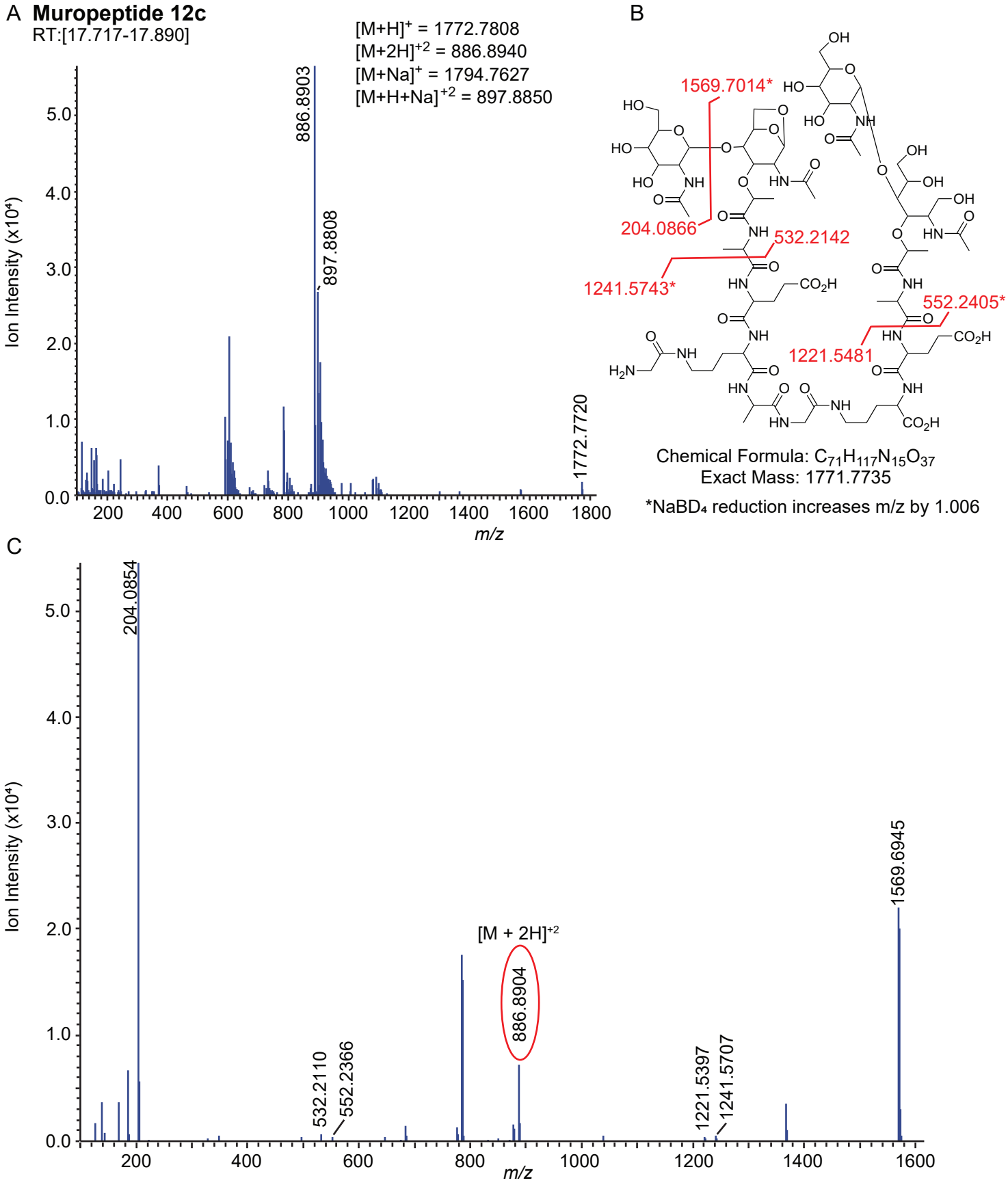

Supplemental Figure 25: (A) MS1 spectra generated from scanning retention times of 17.717-17.890 minutes. (B) The structure of muropeptide 12c. Cleavages with resulting *m/z* fragments are shown in red. (C) MS2 obtained from targeting precursor ion 886.8902 $[M+H]^{+2}$. Red fragments generated in B correspond to observed MS2 fragments in C.

A **Muropeptide 15a**

RT:[18.370-18.570]

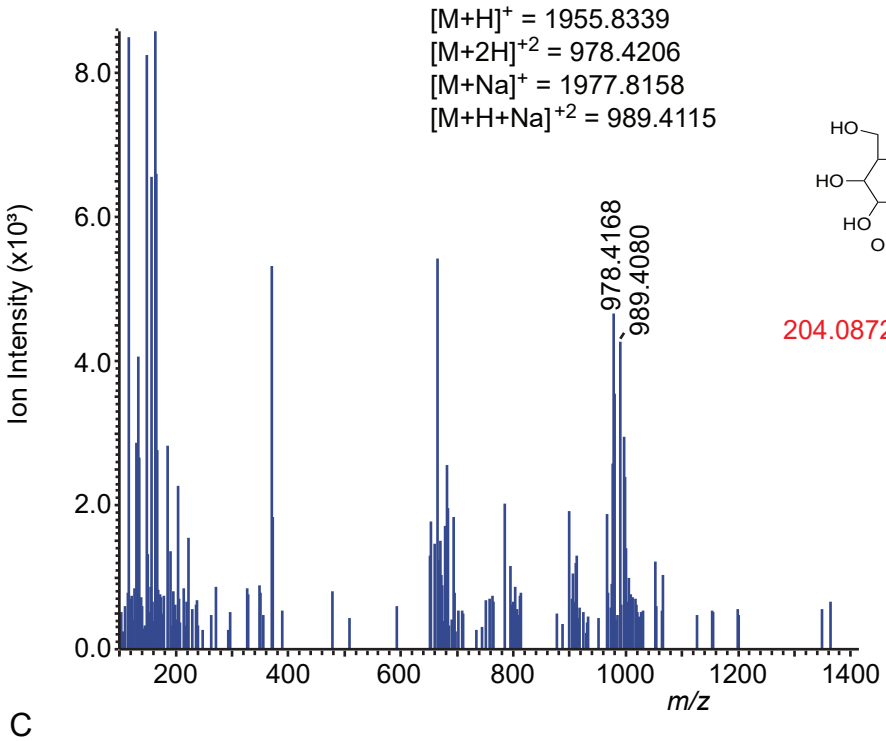

B

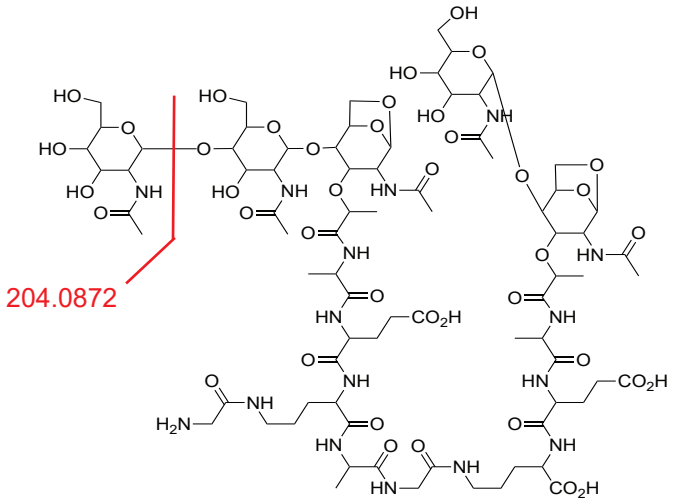

Chemical Formula: $C_{79}H_{126}N_{16}O_{41}$

Exact Mass: 1954.8266

*$NaBD_4$ reduction increases m/z by 1.006

C

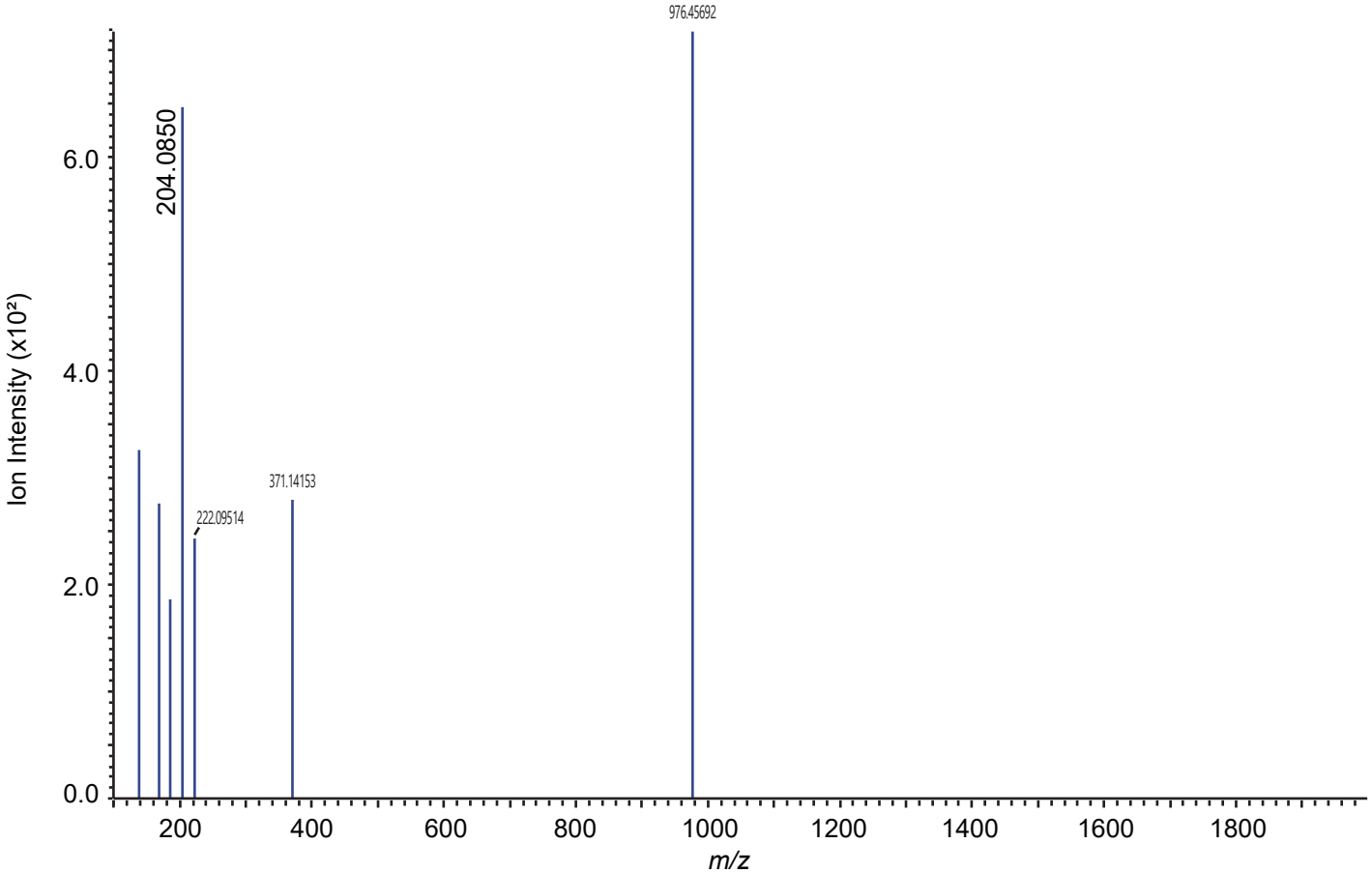

Supplemental Figure 26: (A) MS1 spectra generated from scanning retention times of 18.370-18.570 minutes. (B) The structure of muropeptide 15a. Cleavages with resulting *m/z* fragments are shown in red. (C) MS2 obtained from targeting precursor ion 978.417 $[M+H]^{+2}$. Red fragments generated in B correspond to observed MS2 fragments in C.

A **Muropeptide 16a**
RT:[18.917-19.130]

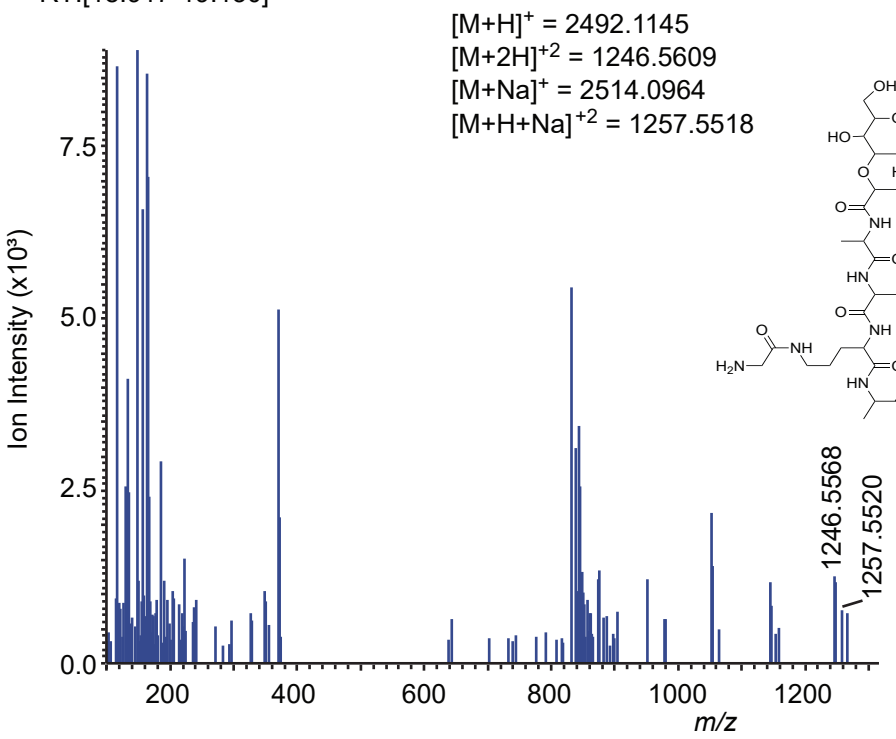

B

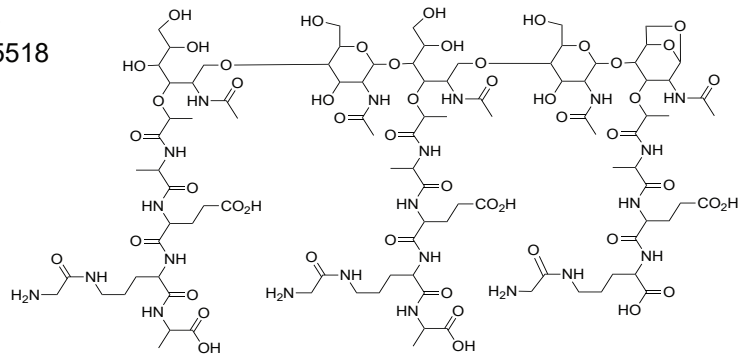

Chemical Formula: $C_{100}H_{166}N_{22}O_{51}$
Exact Mass: 2491.1072

*$NaBD_4$ reduction increases m/z by 1.006

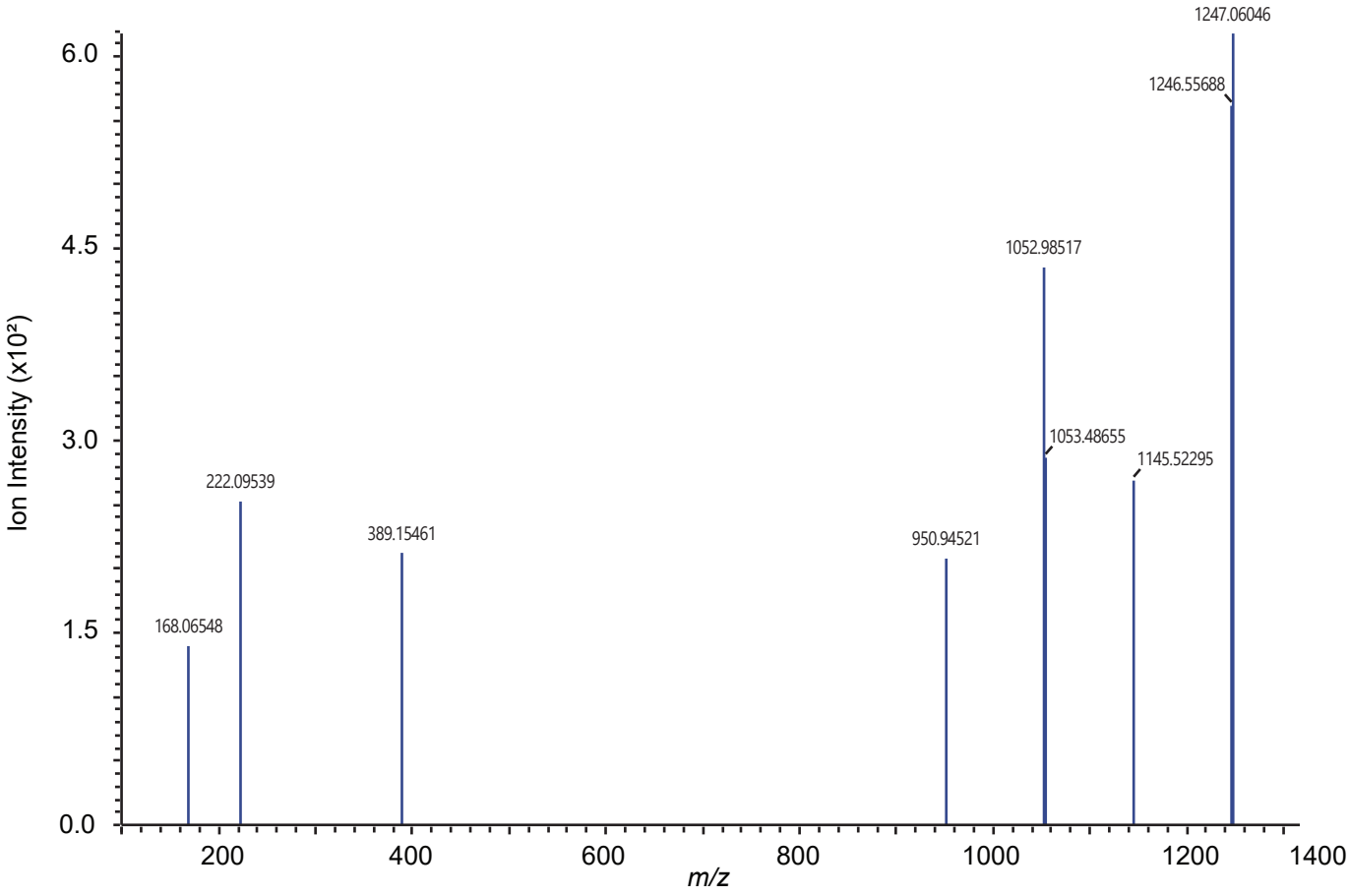

Supplemental Figure 27: (A) MS1 spectra generated from scanning retention times of 18.917-19.130 minutes. (B) The structure of muropeptide 16a. (C) MS2 obtained from targeting precursor ion 1246.5609 $[M+H]^{+2}$.

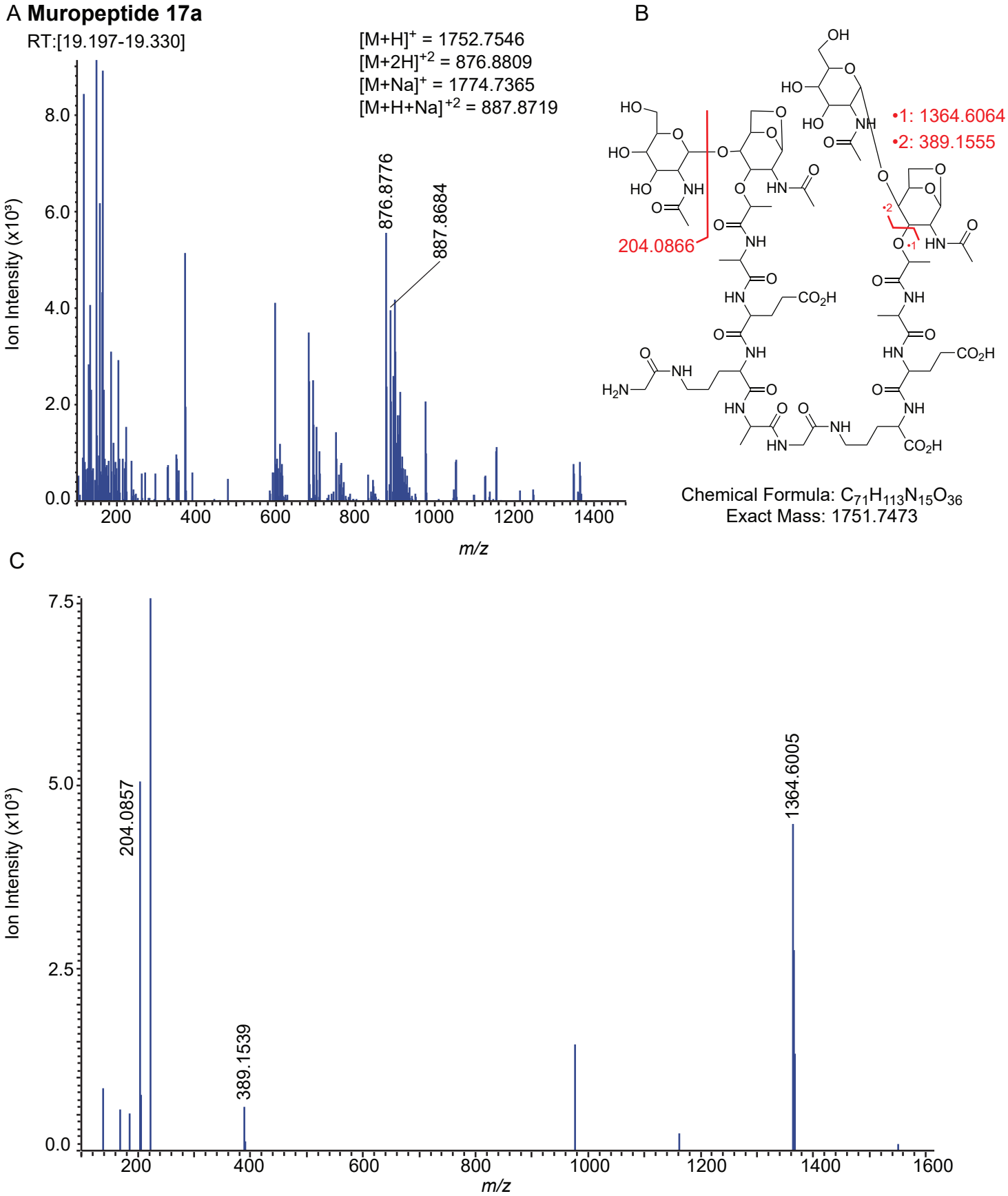

Supplemental Figure 28: (A) MS1 spectra generated from scanning retention times of 19.197-19.330 minutes. (B) The structure of muropeptide 17a. Cleavages with resulting *m/z* fragments are shown in red. (C) MS2 obtained from targeting precursor ion 876.87755 $[M+H]^{+2}$. Red fragments generated in B correspond to observed MS2 fragments in C.

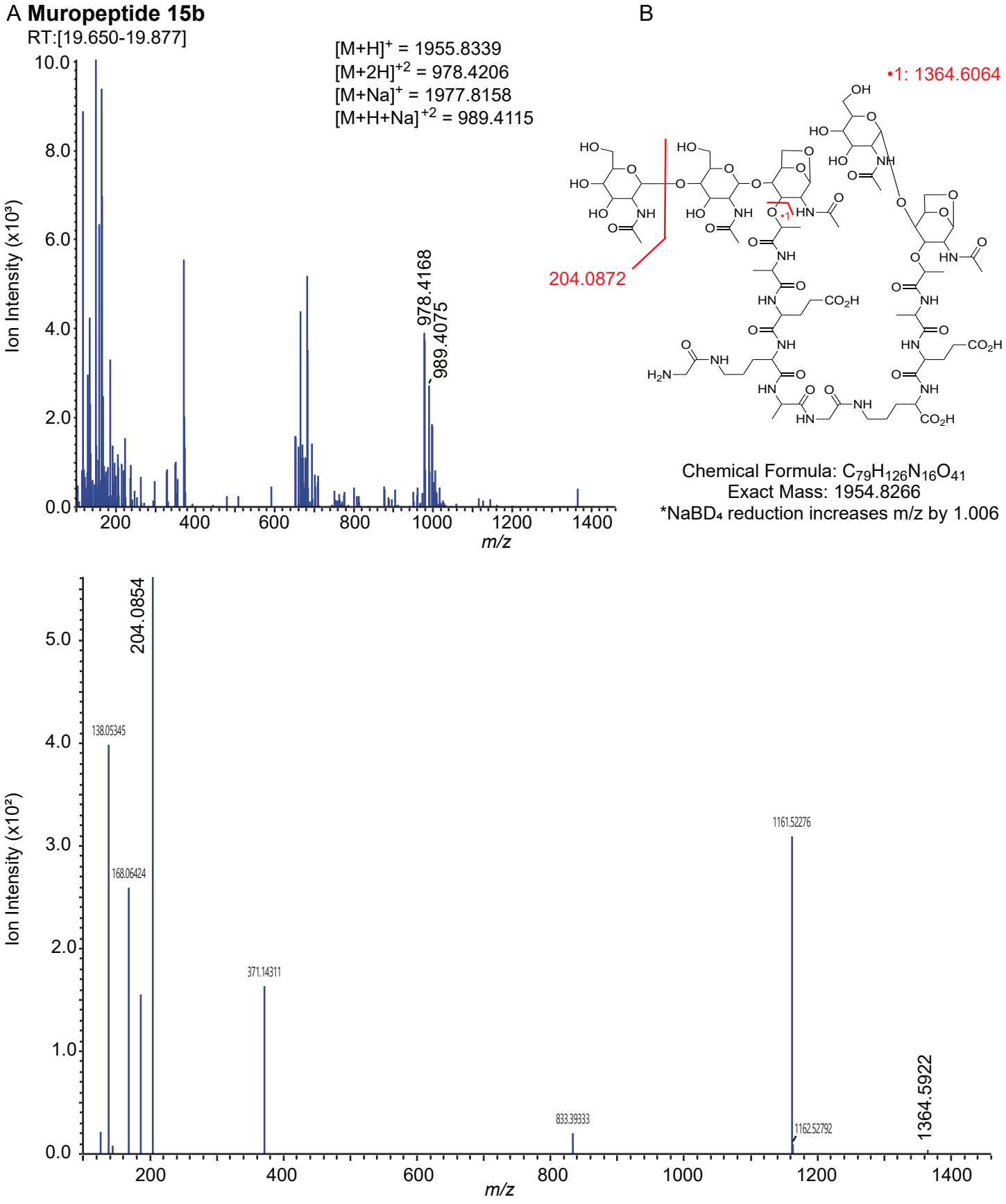

Supplemental Figure 29: (A) MS1 spectra generated from scanning retention times of 19.650-19.877 minutes. (B) The structure of muropeptide 15b. Cleavages with resulting *m/z* fragments are shown in red. (C) MS2 obtained from targeting precursor ion 978.4168 $[M+H]^{+2}$. Red fragments generated in B correspond to observed MS2 fragments in C.

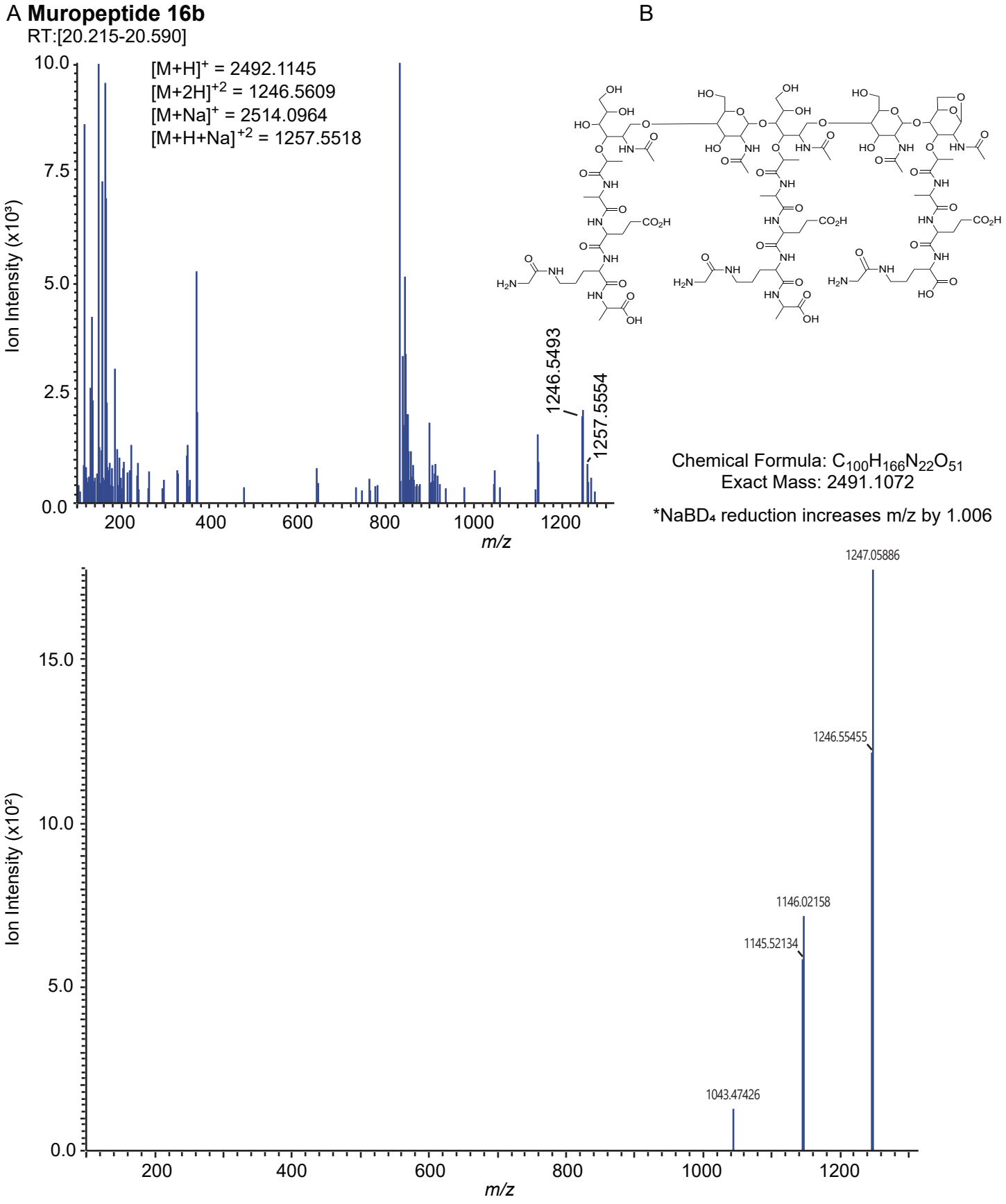

Supplemental Figure 30: (A) MS1 spectra generated from scanning retention times of 20.215-20.590 minutes. (B) The structure of muropeptide 16b. (C) MS2 obtained from targeting precursor ion 1246.5609 $[M+H]^{+2}$.

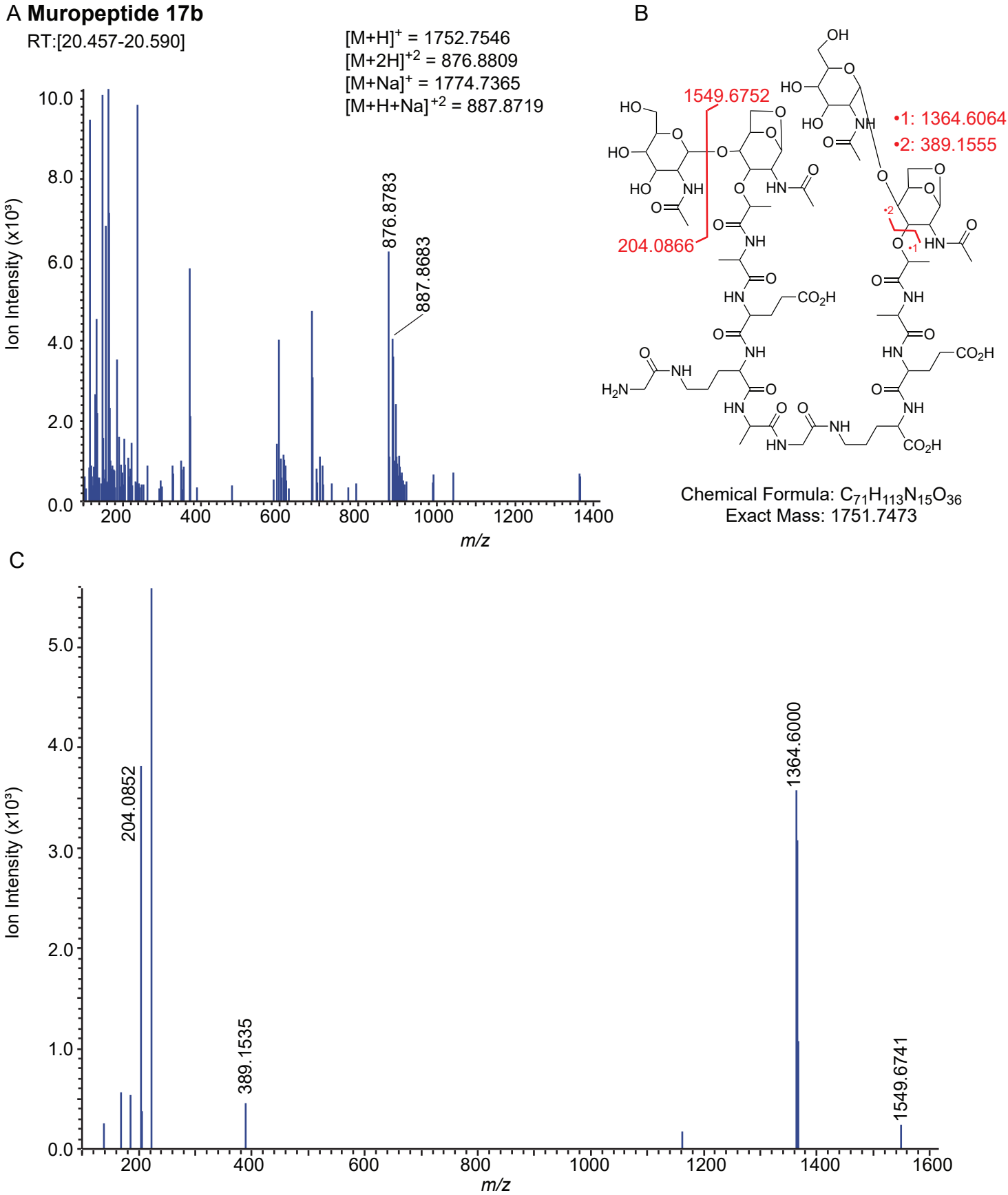

Supplemental Figure 31: (A) MS1 spectra generated from scanning retention times of 20.457-20.590 minutes. (B) The structure of muropeptide 17b. Cleavages with resulting *m/z* fragments are shown in red. (C) MS2 obtained from targeting precursor ion 876.87755 $[M+H]^{+2}$. Red fragments generated in B correspond to observed MS2 fragments in C.

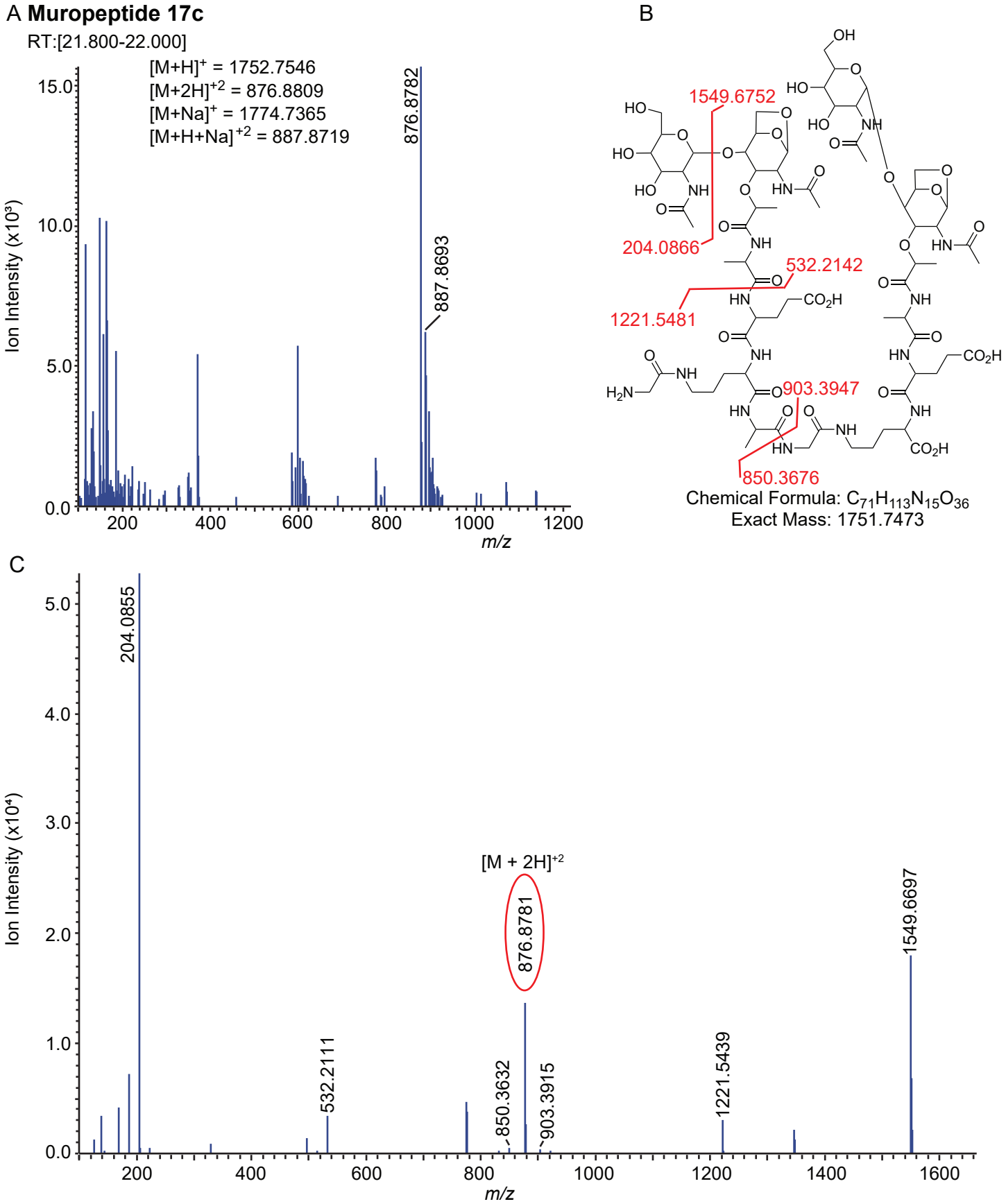

Supplemental Figure 32: (A) MS1 spectra generated from scanning retention times of 21.800-22.000 minutes. (B) The structure of muropeptide 17c. Cleavages with resulting *m/z* fragments are shown in red. (C) MS2 obtained from targeting precursor ion 876.87755 $[M+H]^{+2}$. Red fragments generated in B correspond to observed MS2 fragments in C.

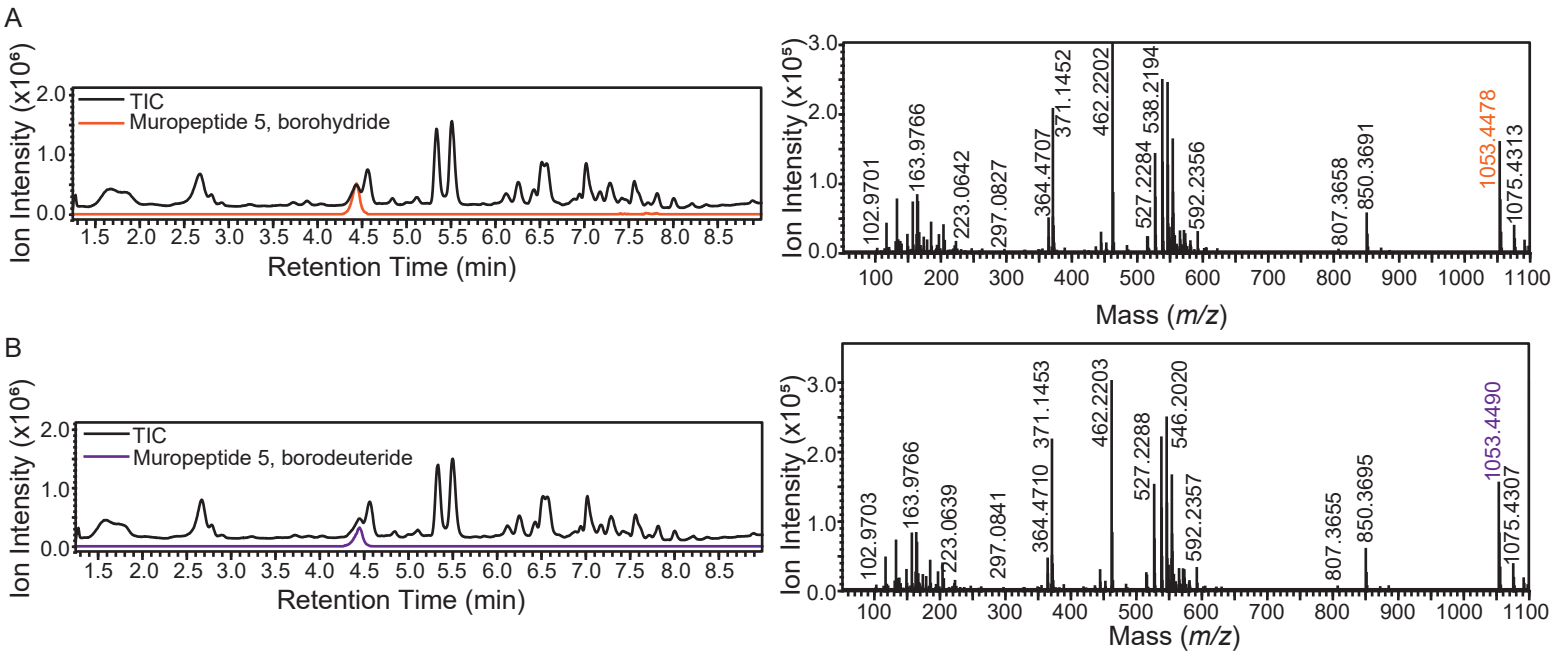

Supplemental Figure 33: A) LCMS chromatogram of borohydride reduced 5A11 *B. burgdorferi* peptidoglycan (left) and corresponding MS/MS spectra of borohydride reduced muropeptide 5 (right). The TIC is shown in black and the abundance of borohydride reduced muropeptide 5 is shown in orange (1053.4277-1053.4699 *m/z* scanned). The precursor ion selected for MS/MS is shown in orange. B) LCMS chromatogram of borodeuteride reduced 5A11 *B. burgdorferi* peptidoglycan (left) and corresponding MS/MS spectra of muropeptide 5 (right). The TIC is shown in black and the abundance of borodeuteride reduced muropeptide 5 is shown in purple (1053.4289-1053.4711 *m/z* scanned). The precursor ion selected for MS/MS is shown in purple.

Supplemental Table 4: A comparison of plasmid content in 5A11, 5A3, 5A3 N.I., and 5A3/*chbC B. burgdorferi* strains.

Plasmid	5A11	5A3	5A3 N. I.	5A3/*chbC*
cp9	+	-	-	-
cp26	+	+	+	+
cp32-1	+	+	+	+
cp32-3	+	+	+	+
cp32-4	+	+	+	+
cp32-6	+	+	+	+
cp32-7	+	+	+	+
cp32-8	+	+	+	+
cp32-9	+	+	+	+
lp5	+	-	-	-
lp17	+	+	+	+
lp21	+	+	-	+
lp25	+	+	-	+
lp28-1	+	+	-	+
lp28-2	+	+	+	+
lp28-3	+	+	+	+
lp28-4	+	+	+	+
lp36	+	+	-	+
lp38	+	+	+	+
lp54	+	+	+	+
lp56	+	+	+	+

Supplemental Table 5: In addition to the clean deletion of *chbC*, 5A3/*chbC* had the following single nucleotide polymorphisms, relative to 5A3.

Location	Position	Mutation	Annotation	Gene
lp28-1	27,425	S141S (AG<u>T</u>→AG<u>C</u>)	variable surface antigen VlsE	BB_RS05840 →
lp28-1	37,433	A144D (G<u>C</u>T→G<u>A</u>T)	variable surface antigen VlsE	BB_RS05840 →
lp28-1	27,897	D299N (<u>G</u>AT→<u>A</u>AT)	variable surface antigen VlsE	BB_RS05840 →
lp28-1	27,901	G300D (G<u>G</u>T→G<u>A</u>T)	variable surface antigen VlsE	BB_RS05840 →
lp28-1	27,910	E303G (G<u>A</u>G→G<u>G</u>G)	variable surface antigen VlsE	BB_RS05840 →

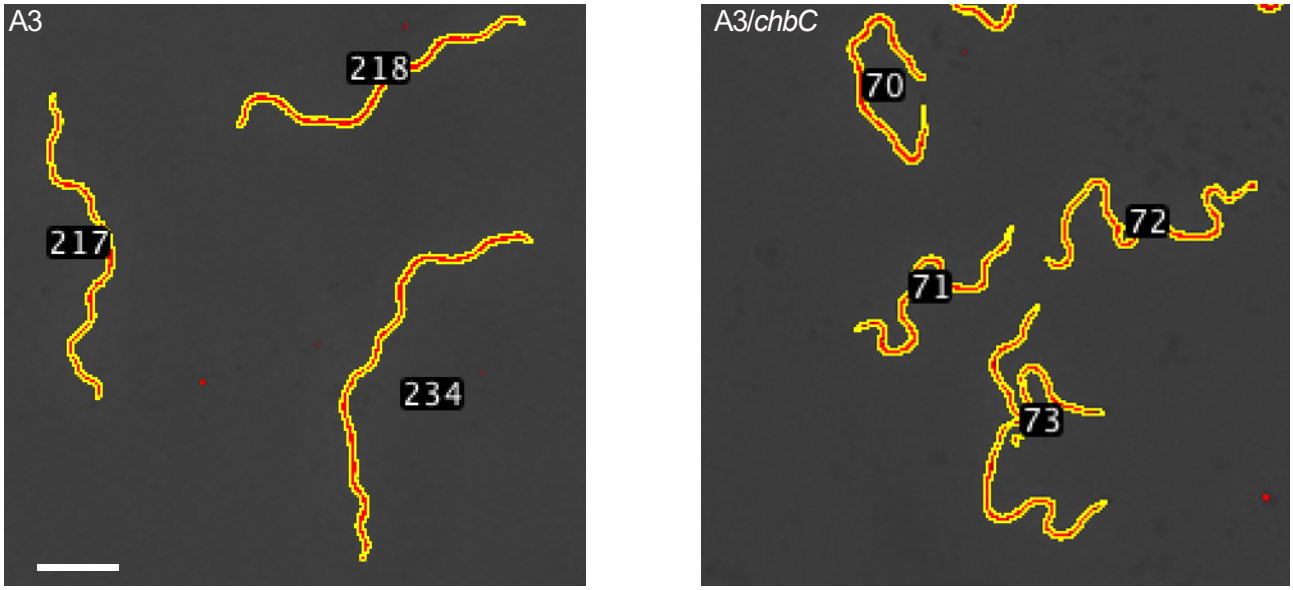

Supplemental Figure 34: Thresholds applied to phase-contrast micrographs containing *B. burgdorferi* A3 (left) and A3/*chbC* (right). Thresholds were generated using Fiji. Scale bars are 5 μm.

A

Feature Name	Retention Time (min)	# of Peaks
C01	13.34	31
C02	17.01	23
C03*°	9.08	17
C04	11.61	13
C05	17.83	12
C06	3.10	12
C09	3.10	9
C10	12.71	8
C11*	15.86	7
C12	16.45	7
C13	13.34	6
C14	13.35	6
C15	13.35	6
C16	3.10	6
C17	1.82	6
C18	16.45	5
C19	17.01	5
C20	17.82	3
C21	13.34	3
C22	13.34	3
C23	12.80	3
C24	5.74	3
C25	20.38	2
C26	19.15	2
C27	16.02	2
C28	13.34	2
C29	12.71	2
C30	13.03	2
C31	12.78	2
C36	3.09	2
C37	3.11	2

Supplemental Table 6: A) Features generated in RamCluster used for the comparison of G-G-anhM content in peptidoglycan from A3 and A3/*chbC B. burgdorferi*. Each feature is composed of a retention time and at least two peaks that correspond to an individual *m/z*. All features listed were used in the analysis. Features designated with an asterisk contain peaks corresponding to G-G-anhM. Features not listed (feature c07, c08, and c32-c35) were manually omitted — they represented adducts and redundancies that were not filtered out by RamClustR. A further breakdown of the peaks that compose each feature can be found in Supplemental Dataset 1. B) Relative comparison of G-G-anhM intensity in 5A3 and 5A3/*chbC B. burgdorferi*. All features were divided into two groups: G-G-anhM (features C03 & C11, designated by asterisk) or G-M (all other features).

°Feature C03 contained peaks corresponding to two separate muropeptides that had nearly identical retention times — one G-G-anhM and one G-M. Peaks within C03 were manually assigned as G-G-anhM or G-M depending on the muropeptide they correspond to. A further breakdown of which peaks in C03 correspond to G-G-anhM can be found in Supplemental Dataset 1.

B

Strain	Total G-G-anhM Intensity	Total G-M Intensity	% G-G-anhM in Total PG	% G-G-anhM Reduction Relative to 5A3
5A3	68977	4813717	1.43	–
5A3/*chbC*	47423	5249974	0.90	37.1

Supplemental Dataset 1: Features generated by RamClustR for *B. burgdorferi* PG analysis (Chapter III). Each feature is composed of a retention time and at least 2 peaks that correspond to an individual *m/z*. The relative intensity of each peak is shown beside its *m/z*. In feature C03, *m/z* designated by an asterisk correspond to G-G-anhM, while all others correspond to G-M.

Name: C01
Comment: Rt=800.55
Num Peaks: 31
896.913 721618
897.415 623498
907.904 331832
897.916 320251
915.887 292098
908.406 287435
916.388 252714
908.907 154017
916.89 131794
918.895 124985
898.417 122585
919.397 105900
927.379 61077
909.408 60791
919.897 59373
917.391 51031
929.886 47527
930.388 40276
937.868 40129
927.88 33916
938.37 33422
923.872 32777
923.372 28221
940.877 27575
920.398 25145
941.378 23185
930.888 22956
917.89 22264
620.26 22261
1792.817 20304
1793.82 16783

Name: C02
Comment: Rt=1020.78
Num Peaks: 23
906.086 165191
905.752 125644
906.376 122830
918.735 82505
913.413 75732
906.754 65595
918.401 61697
913.079 56840
913.747 56643
1358.624 52129
1358.122 39006
1359.125 38209
919.404 32508
920.74 31346
914.081 30680
926.062 30670
931.384 26923
907.088 26837
920.406 24926
921.074 24556
925.728 24114
926.396 23433
1359.627 18816

Name: C03
Comment: Rt=545.06
Num Peaks: 17
850.372 254630
445.165 183612
437.183 119308
463.225 118020
851.376 102541
872.354 75674
425.69 68308
888.32 62031
647.292 60601
445.666 54658
447.672* 45142
538.723* 43790
455.654* 34030
1053.453* 32320
873.357* 28676
852.378* 27910
916.319* 23052

Name: C04
Comment: Rt=696.82
Num Peaks: 13
425.69 294457
850.372 203790
436.681 159795
445.165 128731
426.192 120560
647.292 101151
851.376 82185
437.183 65192
888.32 38611
445.666 37452
463.638 33318
426.693 32866
648.295 28926

Name: C05
Comment: Rt=1069.6
Num Peaks: 12
886.9 220856
887.402 195969
897.891 106618
887.903 97409

898.393 91562
604.252 80291
905.874 77155
604.586 69600
888.404 39057
906.877 33371
908.882 25899
591.937 25448

Name: C06
Comment: Rt=185.83
Num Peaks: 12
436.205 996211
667.318 803614
447.196 564397
436.706 296506
668.321 251691
457.685 236923
447.696 195929
455.679 185438
462.159 122737
462.662 108018
437.207 69564
448.196 49767

Name: C07
Comment: Rt=1005.3
Num Peaks: 9
838.392 65295
838.058 49915
838.727 45179
851.042 34684
845.72 30518
850.707 30391
851.376 24122
845.385 24048
1257.084 22179

Name: C08
Comment: Rt=185.62
Num Peaks: 9
871.402 686800
892.38 567028
893.384 230989
872.404 204591
914.362 104979
894.386 66309
873.407 44926
915.366 39921
933.337 29330

Name: C09
Comment: Rt=186.06
Num Peaks: 9
908.346 257636
479.668 252629
936.345 183153
909.349 104485
480.169 103852
937.348 75429
476.659 69304
1004.333 68424
930.328 51711

Name: C10
Comment: Rt=762.43
Num Peaks: 8
814.346 109607
796.376 102296
543.234 91084
543.568 70584
543.902 31331
555.883 29405
817.355 27754
796.877 20922

Name: C11
Comment: Rt=951.84
Num Peaks: 7
988.44 41391
671.946 40357
988.942 40355
672.28 38547
1007.414 25625
999.431 23400
1007.916 22887

Name: C12
Comment: Rt=987.14
Num Peaks: 7
886.9 151025
887.402 141979
898.393 80836
887.903 73934
906.877 36028
908.882 28980
693.826 14236

Name: C13
Comment: Rt=800.54
Num Peaks: 6
926.878 74706
613.267 55840
948.86 36955
952.37 31976
949.361 31273
599.281 29314

Name: C14
Comment: Rt=800.85
Num Peaks: 6

610.927 257806
611.262 223988
611.596 117131
623.911 68942
934.861 63735
618.254 60310

Name: C15
Comment: Rt=800.76
Num Peaks: 6
598.278 179005
598.613 154701
605.605 112347
605.94 97334
935.362 52442
611.93 45821

Name: C16
Comment: Rt=186.07
Num Peaks: 6
435.704 2263598
446.694 1311971
454.677 1275106
455.178 578992
465.668 145484
458.187 88940

Name: C17
Comment: Rt=108.98
Num Peaks: 6
667.318 500441
414.698 170050
668.321 155679
689.3 92797
705.265 55891
690.303 27180

Name: C18
Comment: Rt=986.99
Num Peaks: 5
692.825 105357
604.252 86069
897.891 84430
905.874 80923
604.586 73921

Name: C19
Comment: Rt=1020.74
Num Peaks: 5
919.069 59918
1369.615 25449
1377.598 18976
1369.113 18002
1370.116 17996

Name: C20
Comment: Rt=1069.33
Num Peaks: 3
591.603 27935
598.93 23545
909.383 20963

Name: C21
Comment: Rt=800.67
Num Peaks: 3
598.947 76224
618.589 51410
898.919 37162

Name: C22
Comment: Rt=800.62
Num Peaks: 3
612.933 66058
606.273 54404
613.6 33679

Name: C23
Comment: Rt=768.18
Num Peaks: 3
692.825 236640
693.326 141352
711.798 75589

Name: C24
Comment: Rt=344.58
Num Peaks: 3
653.79 58139
499.733 36422
654.291 35129

Name: C25
Comment: Rt=1222.88
Num Peaks: 2
899.411 62492
912.06 9074

Name: C26
Comment: Rt=1148.9
Num Peaks: 2
1213.894 21028
1213.56 18463

Name: C27
Comment: Rt=961.45
Num Peaks: 2
785.36 54193
796.351 29807

Name: C28
Comment: Rt=800.6

Num Peaks: 2
623.577 86743
624.245 37370

473.651 112218
513.662 89262

Name: C29
Comment: Rt=762.48
Num Peaks: 2
814.848 68202
815.349 36260

Name: C30
Comment: Rt=781.53
Num Peaks: 2
795.373 205088
795.874 172298

Name: C31
Comment: Rt=766.65
Num Peaks: 2
704.317 69340
712.3 40104

Name: C32
Comment: Rt=762.38
Num Peaks: 2
806.364 100509
807.366 38764

Name: C33
Comment: Rt=545.18
Num Peaks: 2
538.222 91114
463.638 55793

Name: C34
Comment: Rt=545.12
Num Peaks: 2
444.664 403450
436.681 257394

Name: C35
Comment: Rt=545.08
Num Peaks: 2
546.204 114776
437.683 34113

Name: C36
Comment: Rt=185.45
Num Peaks: 2
468.676 108704
469.178 41933

Name: C37
Comment: Rt=186.7
Num Peaks: 2

Supplemental Dataset 2: Features generated by RamClustR for interspecies PG comparison (Chapter IV). Each feature is composed of a retention time and at least 2 peaks that correspond to an individual *m/z*. The relative intensity for each peak is shown beside its *m/z*.

Name: C01
Comment: Rt=13.27
Num Peaks: 91
896.91 267738
897.411 229924
915.883 205411
610.926 204293
916.385 177597
611.26 176096
897.912 119315
795.37 109814
598.277 95367
916.886 94314
611.594 93389
623.575 86429
598.611 83188
907.899 76015
623.909 75509
814.343 71756
908.401 67750
934.857 57956
908.897 57376
814.845 55357
935.358 51108
898.414 45873
606.266 43978
598.946 42808
624.243 42753
796.373 39585
605.602 39550
618.916 38175
926.873 38092
611.928 37493
618.252 37376
917.387 37328
605.937 36130
618.586 34050
927.374 33776
927.87 32320
909.396 32228
467.934 29405
935.859 28793
918.89 28187
606.6 28102
1386.648 27881
945.847 26677
468.185 25306
616.25 25170
806.359 24653
619.249 24267
628.898 24221
636.224 23511
919.392 23408
946.348 22826
694.331 21664
937.864 21467
807.354 21144
942.843 20144
928.369 19686
624.577 18578
616.584 18399
630.901 17896
938.365 17762
625.579 17741
919.888 17692
948.854 17423
917.886 17207
924.37 17096
599.28 16914
612.261 16888
612.93 16520
629.233 16413
946.847 16345
631.235 15489
631.566 15434
628.564 15402
923.367 14511
909.896 14268
796.874 14207
942.342 13930
938.862 13466
606.933 13221

936.36 13080
613.594 12913
619.583 12779
928.87 11413
626.245 11331
624.909 10905
924.871 10701
929.879 10299
949.855 10107
920.386 9577
957.34 8973
939.361 7773

Name: C02
Comment: Rt=16.68
Num Peaks: 82
604.251 106474
692.822 97109
604.585 91304
886.897 91088
887.398 78480
905.87 72312
906.084 71872
693.324 64931
906.372 60742
905.749 54837
918.733 53946
711.796 53783
906.418 53736
616.9 52124
604.919 48144
617.234 45066
918.398 41183
887.9 40299
919.067 40110
851.04 38226
838.39 37558
1181.554 36234
712.298 35774
906.873 32672
850.705 31750
838.056 30103
906.752 28836
693.824 28297
838.725 25814
617.568 25365
924.844 23961
703.812 22196
1053.497 22163
919.402 22073
875.058 20977
925.345 20624
931.382 20541
1182.557 20247
898.885 19135
605.253 18783
462.928 18193
913.742 18054
704.806 17342
913.41 17042
629.549 16724
874.723 15959
931.716 15852
599.591 15502
622.224 15070
888.401 14764
704.313 14610
875.392 14521
629.883 14432
914.075 13581
699.04 13158
698.539 13096
612.573 12788
907.087 12718
839.059 12584
913.076 12476
907.374 12360
926.391 11679
887.707 10891
925.846 10866
919.735 10525
1384.633 10489

617.902 10035
926.723 9114
770.025 9067
719.781 8796
932.05 8753
782.675 8555
630.216 8511
546.314 8215
769.691 7924
925.725 7643
463.429 7591
782.341 7440
699.291 7075
634.872 6981
456.282 4620
571.309 4131

Name: C03
Comment: Rt=12.81
Num Peaks: 64
795.37 161885
795.871 123810
543.232 114205
814.343 94709
543.566 88852
693.829 80068
814.844 72594
796.372 58473
693.83 48694
555.881 48671
694.331 48631
543.901 42275
556.215 38408
815.346 34522
694.331 32798
806.359 31207
833.317 27511
806.86 24825
807.355 23410
475.539 22286
833.818 21511
796.874 20179
712.803 19971
556.549 19230
694.832 19166
530.583 18752
551.221 17216
538.572 16669
537.908 16269
544.235 15521
713.305 15376
475.873 14855
417.163 13833
857.382 13530
538.242 13304
550.558 12998
713.305 12971
825.332 12892
807.854 12311
561.205 12099
815.847 11963
826.328 11566
822.328 11429
834.319 10659
825.834 10457
488.186 10347
417.414 10318
551.554 10289
857.047 10098
538.905 10091
548.556 9771
844.307 9144
857.716 8449
844.808 7217
826.827 6754
544.567 6723
653.613 6702
653.947 6503
821.826 6420
640.964 4243
652.776 4122
641.298 3834

858.05 3505
652.526 2938

Name: C04
Comment: Rt=2.99
Num Peaks: 53
870.394 1352541
454.676 1065595
435.702 1024953
871.397 553290
455.177 440236
436.203 424101
892.375 332695
908.341 213483
872.4 165082
893.378 140992
455.678 139610
436.705 127963
462.661 101428
909.344 89998
462.158 65950
448.185 64390
930.323 61528
894.373 61237
914.357 58937
463.163 40702
578.253 38286
873.402 37130
456.179 36403
456.674 31844
933.332 31101
437.206 30098
924.312 28546
426.165 28080
910.346 28039
931.325 27370
915.359 25629
933.834 23083
463.663 21481
923.309 21342
927.317 17145
934.333 16168
870.609 15509
895.372 15392
908.844 14589
916.337 14372
925.321 14339
454.834 13313
720.226 12801
435.856 12709
941.317 12316
927.818 11677
649.304 11252
932.324 10923
930.826 10148
928.317 9286
941.818 8824
912.339 8397
926.323 8224

Name: C05
Comment: Rt=6.31
Num Peaks: 41
499.731 117123
518.705 109682
506.739 81727
525.713 79152
795.373 64379
500.233 55823
519.206 51936
809.389 44167
507.241 39616
526.214 38535
510.721 33003
514.737 30301
533.71 26815
796.376 23956
537.678 23280
517.729 22390
511.713 19193
544.686 17835
416.151 17716

500.734 17401
519.708 17104
558.205 16770
998.453 16111
511.222 15962
500.233 14877
515.238 14231
526.698 13899
825.384 13781
519.206 13031
526.715 12811
534.212 12568
507.742 12542
518.23 11018
538.18 10928
529.694 8607
545.188 8457
512.214 7221
545.664 5900
410.17 5618
552.684 5387
521.712 5027

Name: C06
Comment: Rt=19.41
Num Peaks: 36
912.058 43010
899.409 41340
911.724 32547
912.392 32393
899.075 31063
899.743 30040
459.282 29369
1052.992 22278
950.95 21986
1052.491 21707
844.364 21503
951.452 19939
1154.532 18823
844.03 17470
912.726 16810
1154.031 16060
900.078 15904
924.707 15507
831.715 15157
844.699 14589
905.383 12645
831.381 12532
924.373 12519
906.735 11679
925.041 11556
832.05 9532
693.533 9240
694.034 9182
905.049 8509
1145.863 8392
892.734 7991
925.381 7748
460.285 6852
929.665 6609
900.411 5524
857.013 5349

Name: C07
Comment: Rt=2.75
Num Peaks: 36
457.683 93904
479.666 91822
936.339 88749
470.205 78396
468.674 44699
458.185 39834
480.167 38394
937.342 38124
510.651 26032
513.659 25808
689.296 25470
458.678 23600
487.65 22539
1004.326 18974
469.175 18530
471.208 16699

544.645 16368
967.326 15896
412.135 15857
418.88 15240
424.896 14099
480.667 13167
521.643 13142
507.642 12621
967.828 12451
998.31 12166
486.179 12047
518.634 11447
586.307 11184
608.289 10764
514.16 10058
486.867 9782
492.884 7970
552.628 7741
547.652 7229
1005.329 6536

Name: C08
Comment: Rt=17.87
Num Peaks: 35
886.897 101357
887.397 93274
604.251 81773
604.586 70187
905.871 55729
906.372 48454
887.904 46275
604.92 37031
616.9 34733
617.234 29961
421.209 25839
638.813 25673
906.874 25263
898.389 22182
591.602 21839
888.4 19829
591.936 18937
898.885 18303
924.844 17073
617.568 16979
639.314 15614
925.346 14870
605.254 14367
599.592 14179
967.102 11872
979.752 10540
907.375 10315
622.224 10081
592.271 10006
682.81 9542
609.575 9160
599.924 9032
979.419 8517
728.275 8008
683.312 6005

Name: C09
Comment: Rt=20.54
Num Peaks: 32
899.409 45350
515.214 37463
899.075 34223
912.058 33922
899.743 33598
912.392 25552
911.724 25500
844.365 20331
831.716 19113
900.078 17935
844.03 16613
577.372 16427
682.81 15451
1145.527 15450
831.381 15115
844.699 13973
597.576 13936
912.727 13292
1145.025 13149

832.05 12136
407.19 11441
1247.067 11436
924.707 11404
906.735 10947
876.885 10463
496.22 10376
516.218 10019
683.312 9480
877.386 9234
1246.565 8754
925.041 8452
900.412 7368

Name: C10
Comment: Rt=11.76
Num Peaks: 24
860.383 66884
586.574 65482
860.884 54689
586.909 53660
573.926 41506
574.26 35711
881.732 33196
587.243 28411
574.26 26756
881.398 25526
861.386 24467
882.067 23057
587.243 20958
515.7 19398
558.223 18053
440.183 13454
574.594 13245
857.381 11323
879.356 10488
581.915 9325
516.202 9163
857.047 8810
879.858 8117
581.251 7973

Name: C11
Comment: Rt=11.15
Num Peaks: 23
444.662 315887
425.689 159309
647.288 148969
445.164 130207
850.368 117302
426.19 65515
436.678 63833
851.371 47804
648.291 46893
425.689 44614
437.67 43846
463.636 43689
445.665 38609
437.179 29200
452.648 29123
452.145 19929
426.692 18906
426.19 18818
464.137 17943
438.17 15910
453.15 14969
453.149 11322
649.294 10346

Name: C12
Comment: Rt=10.03
Num Peaks: 21
758.843 55463
759.345 39751
518.881 38451
541.699 32041
522.726 31380
416.152 30162
758.843 28979
480.181 28067
519.216 24257
533.257 21484

759.345 20746
417.159 18832
841.361 15470
542.2 15318
523.227 14841
793.346 13867
440.183 13701
590.267 13233
480.683 12166
416.653 11267
440.434 10421

Name: C13
Comment: Rt=12.7
Num Peaks: 21
692.822 67165
693.323 45066
711.795 38693
474.867 38453
712.802 28979
475.201 25908
712.297 25352
591.282 23164
636.558 21734
487.516 18107
431.25 16265
468.435 14254
636.891 13592
475.536 13261
703.812 13155
610.255 12731
704.809 12520
487.85 12425
591.784 12234
631.899 10190
730.769 9405

Name: C14
Comment: Rt=9.18
Num Peaks: 19
546.202 138094
546.704 70292
1053.447 47617
538.218 34852
527.229 30942
565.176 28371
547.205 24872
464.225 24720
1054.45 23707
538.719 19355
539.212 18276
527.73 15305
565.677 14663
554.188 10141
435.224 9379
557.19 9173
430.23 8494
539.712 6860
592.235 6595

Name: C15
Comment: Rt=15.73
Num Peaks: 17
671.944 49574
672.278 48035
692.822 41472
693.324 27910
672.613 27271
684.593 21447
684.927 20404
988.437 20104
591.282 13960
672.947 11305
875.058 10629
989.439 10429
659.295 9761
513.697 9008
513.948 8057
679.269 7745
574.32 4627

Name: C16
Comment: Rt=3.17
Num Peaks: 16
667.315 918437
668.318 290398
447.685 189637
473.649 128548
669.32 72045
474.151 55563
466.659 42816
481.635 36660
481.132 23785
474.651 21069
448.686 18162
691.273 16029
482.136 14634
670.323 12144
464.231 10667
667.492 10621

Name: C17
Comment: Rt=8.96
Num Peaks: 15
444.662 525301
445.164 217001
436.678 117826
647.288 76515
445.665 66763
437.671 55940
437.179 53634
452.648 36258
648.292 24746
456.643 24565
471.621 21465
438.171 19521
466.644 18006
446.166 16758
467.145 7132

Name: C18
Comment: Rt=3.62
Num Peaks: 15
446.692 537690
447.193 232981
465.665 99044
414.696 91687
476.657 58705
466.166 46883
487.19 43648
415.198 35060
477.159 24440
461.683 20966
442.71 19899
681.33 15276
433.67 13128
484.642 10053
477.658 8946

Name: C19
Comment: Rt=15.65
Num Peaks: 13
591.282 38460
785.357 35971
536.557 32359
785.859 27404
536.892 24982
591.784 21803
549.206 17406
549.541 13370
786.36 12221
850.872 11381
537.226 11322
610.758 9934
580.234 8894

Name: C20
Comment: Rt=1.83
Num Peaks: 12
667.314 364372
668.317 114443
689.296 48069
705.261 43033

690.279 39095
669.319 27340
733.26 16472
706.264 12940
426.164 8853
418.181 8543
407.19 8191
417.165 5658

Name: C21
Comment: Rt=6.28
Num Peaks: 12
471.22 72073
490.194 71708
738.352 47443
471.722 33122
490.696 32344
482.21 21533
739.355 16573
491.197 10269
472.223 9877
482.712 9727
424.173 9572
941.431 8618

Name: C22
Comment: Rt=17.4
Num Peaks: 12
785.357 80834
785.859 61046
804.331 35950
804.832 26761
536.558 18065
536.892 13930
589.32 9397
549.207 8068
623.304 6983
738.294 6675
446.262 6162
508.241 5011

Name: C23
Comment: Rt=8.77
Num Peaks: 12
447.245 58486
656.811 37304
429.234 34907
504.266 24415
657.312 23603
433.229 22385
450.86 20977
555.271 14363
481.193 14351
448.248 13209
451.194 12769
430.237 7472

Name: C24
Comment: Rt=12.66
Num Peaks: 10
596.922 22158
602.278 19231
774.364 18578
597.256 18424
875.904 16214
876.406 14440
774.866 12980
584.608 11802
456.282 8060
500.272 7022

Name: C25
Comment: Rt=8.99
Num Peaks: 9
462.22 563781
463.223 123410
486.178 37052
515.131 22772
484.2 18977
516.137 15333
559.922 10288
560.256 8181

506.194 7446

Name: C26
Comment: Rt=22.79
Num Peaks: 7
764.431 52104
583.357 29350
765.434 21348
905.383 11984
504.283 10848
451.216 9723
584.36 8484

Name: C27
Comment: Rt=13.27
Num Peaks: 7
795.871 85858
693.83 31970
815.346 26628
806.86 18782
1387.651 18513
949.356 14432
615.915 13609

Name: C28
Comment: Rt=19.21
Num Peaks: 7
976.459 17148
597.576 15675
597.91 13409
701.783 12437
895.858 11329
896.36 10487
876.884 10148

Name: C29
Comment: Rt=8.96
Num Peaks: 7
463.636 77614
464.139 33740
471.118 18168
452.145 17227
464.636 13730
457.144 9332
472.123 8228

Name: C30
Comment: Rt=8.96
Num Peaks: 7
850.368 315326
851.371 129249
888.315 74763
872.348 38807
852.373 38084
889.318 30527
910.296 24983

Name: C31
Comment: Rt=2.38
Num Peaks: 6
487.19 107496
488.193 23417
503.164 8319
556.772 5809
445.129 5686
496.213 4249

Name: C32
Comment: Rt=18.04
Num Peaks: 5
807.03 22186
807.699 15837
705.466 9569
518.282 8167
440.568 5955

Name: C33
Comment: Rt=15.94
Num Peaks: 5
804.331 24801
610.256 18743
804.832 18406

805.334 8071
796.347 7781

Name: C34
Comment: Rt=19.43
Num Peaks: 5
407.229 13800
951.452 13665
565.299 11495
1182.532 10551
1367.58 5329

Name: C35
Comment: Rt=2.59
Num Peaks: 4
556.27 24748
952.308 19637
938.325 16212
953.31 8694

Name: C36
Comment: Rt=15.05
Num Peaks: 4
814.039 19758
813.705 16281
814.373 12790
634.94 6911

Name: C37
Comment: Rt=23.36
Num Peaks: 4
437.236 65841
493.303 18297
438.24 12438
892.734 7600

Name: C38
Comment: Rt=5.82
Num Peaks: 4
674.347 67311
675.35 21596
454.194 7268
434.225 6014

Name: C39
Comment: Rt=5.73
Num Peaks: 4
478.251 24834
653.787 21838
654.288 12958
448.843 12076

Name: C40
Comment: Rt=19.98
Num Peaks: 4
478.27 16503
409.18 13197
665.269 8025
665.269 8009

Name: C41
Comment: Rt=1.69
Num Peaks: 3
411.137 61410
429.148 19179
427.111 13105

Name: C42
Comment: Rt=1.4
Num Peaks: 2
531.22 27809
610.293 14906

Name: C43
Comment: Rt=15.88
Num Peaks: 2
1181.554 21747
592.275 8765

Name: C44
Comment: Rt=9.01
Num Peaks: 2

444.245 29273
562.272 17306

Name: C45
Comment: Rt=1.43
Num Peaks: 2
430.913 15993
554.854 7981

Name: C46
Comment: Rt=1.32
Num Peaks: 2
462.219 97503
463.222 21566

Name: C47
Comment: Rt=21.89
Num Peaks: 2
401.235 27339
467.762 9087